1-1-2015

Multiple Dalitz Plot Analysis At Cleo-C

Mackenzie Smith
Wayne State University,

MULTIPLE DALITZ PLOT ANALYSIS AT CLEO-c

by

MACKENZIE J. SMITH

DISSERTATION

Submitted to the Graduate School

of Wayne State University

in partial fulfillment of the requirements

for the degree of

DOCTOR OF PHILOSOPHY

2015

MAJOR: Physics

Approved By:

_____

Advisor

_____

_____

_____

ACKNOWLEDGEMENTS

This dissertation would not be possible without the assistance and support of many, both with the Department and beyond.

I would first thank my advisor, Professor David Cinabro. Without his guidance, patience, and extraordinary support, I could not have made it to end of this project.

I would also like to thank my thesis committee: Professor Giovanni Bonvicini, Professor Arthur Suits, and Professor Sean Gavin.

I would like to thank Professors Vaman and Ratna Naik, who gave me my first experience of Physics research, nurtured my excitement for physics, and provided the occasional swift kick that I dearly needed.

A very special thanks goes to Professor Aruna Nadasen, without whose faith and advocacy this would be impossible.

Whenever I encountered a seemingly intractable coding error, logic mistake, or miscellaneous processing mystery, I could always turn to Professor Claudr Pruneau, Dr. Mikhail Dubrovin, or Dr. Adam Lincoln. I thank you all for your invaluable help.

Last but certainly not least, I would like to thank my family and friends for their love and support throughout this journey, especially my mother, Belinda. You have been my champion, the person who instilled in me a sense of intellectual curiosity, and a constant reminder to have faith in one's self in spite of all else.

Thank you all.

TABLE OF CONTENTS

LIST OF FIGURES

LIST OF TABLES

CHAPTER 1: INTRODUCTION

1.1 The Standard Model

The Standard Model, the highly successful theory that describes fundamental interactions of forces and particles on subatomic scales, is the crowning achievement of 20th century physics. Its development, which we will cover briefly, mirror the development of perhaps the greatest theory of the 19th century: Atomic Theory. This will not be exhaustive; there are several texts that cover the topic [1] as well as Quantum Field Theory more generally [2] [3]. A more in depth coverage of the development of the Standard Model can be found elsewhere [4].

Humankind has concerned itself with the most basic makeup of the physical world since at least the Greek Hellenistic period. Adopting ideas from earlier writing, the famed philosopher Democritous proposed a universe consisting of the vacuum and small indivisible objects called atoms [5]. Though this proposal was complete speculation, without the specifics necessary to be useful, its broad outline is prescient of a theory that will appear around the turn of the 19th century.

By 1805, it was becoming clear some underlying material structure existed. Antoine Lavoisier had found no measurable change in mass between reactants and their products in a sealed container. Additionally, Joseph Louis Proust found that different samples of a material contained its constituent elements in constant proportion. It was in this climate that John Dalton proposed Atomic Theory. Elements consist of atoms, of which a given element are identical; compounds consist of atoms of two or more elements in integer numbers [5].

During the 1860s, Atomic Theory received a major boost due to efforts to relate elements based on similar characteristics. Though there were several chemists working on the problem including Julius Meyer, John Newlands, and Dmitri Mendeleev, it was Mendeleev's Periodic Table of the Elements that is most widely known. He noticed that elements can be arranged by atomic mass, and into groups. Elements of the same group exhibited similar chemical behavior, and periods could be arranged into orderly increases in mass. Much of the modern

periodic table was unknown in Mendeleev's time, but armed with high degree of order, his table was able to make several predictions about elements that should appear in empty places. Among his predictions, Mendeleev predicts the elements ekaaluminum and ekasilicon, which were later discovered and named gallium and germanium respectively. There is power in patterns; the ability to anticipate unobserved phenomena based on what's been seen before is both the goal and core feature of the scientific endeavor.

The number of particles discovered by the mid 1950s and 1960s requires a similar underlying theory. The discoveries of the electron, the proton, and the neutron set Atomic Theory on solid footing, as well as explain the presence of isotopes. The discovery of the muon together with Fermi's postulate of the near–massless neutrino, which was discovered much later, established the first two lepton generations. The pion and what we now call the kaon were the first of many mesons found. Prior to discovery of the Λ^0 and several other hyperons, the proton and neutron were the only known strongly interacting, high–mass particles. Due to their similar mass and similar strong interaction, the proton and neutron were considered two states of the same "nucleon". In order to account for the difference between the two nucleon states, the property of "isospin" was assigned. This is a close analogy to intrinsic spin.

The discovery of hyperons introduced problems with this interpretation. Λ^0, whose mass is comparable to the nucleons and is produced in strong interactions, has a lifetime that is much longer than expected. Strong interactions that produce this, the $\Sigma^{\pm}$, and $\Xi^{\pm}$ ("Cascade") hyperons also produce kaons; such particles have never been seen outside of this associated production. The solution to these and other problems was the introduction of the "strangeness" by Gell-Mann and independently by Nishijima. As an example, by arranging the mesons of spin-0 by I_3, the "3" projection of isospin similar to S_z, and strangeness one can create an octet as seen in Fig. 1.1, suggesting that there exists some underlying structure.

The quark model posits that quarks are the core constituents in protons, neutrons, and other strongly interacting particles. This theory successfully predicts the existence of a

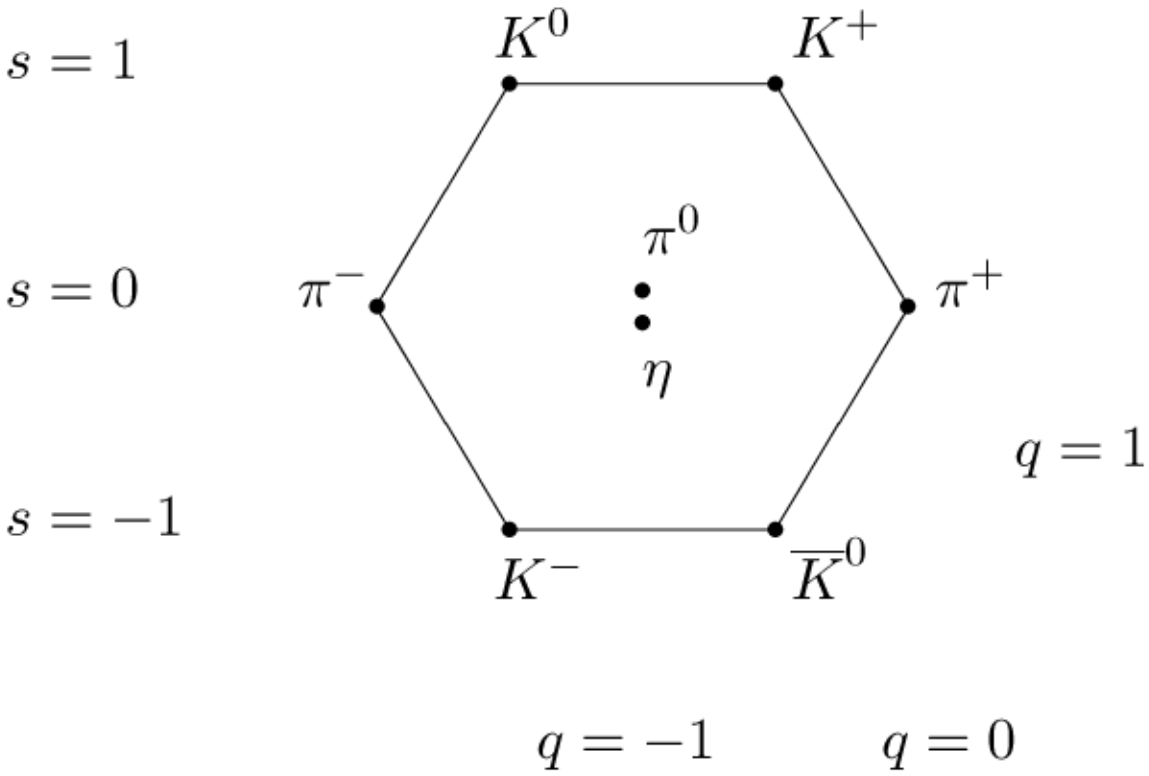

Figure 1.1: A grouping of spin 0 mesons, organized by I_3 (horizontal axis) and strangeness (vertical axis) [6]. Particles sharing a top-left to bottom-right diagonal have the same electric charge. M. Gell-Mann referred to this and other hadron octets by the phrase "Eightfold Way."

bound state containing three strange quarks; this particle, dubbed the Ω^-, was discovered in 1964. Quarks are now a major component of the Standard Model, which describes our best understanding of the fundamental particles and forces in nature. The Standard Model includes six quarks (Table 1.1) and six leptons (Table 1.2) in three generations, along with their respective antiparticles. It also describes the particles that mediates fundamental subatomic forces. These exchange particles, as seen in Table 1.3, are the photon, three Weak bosons, and gluons. The particle mediating the force of gravity is noticeably absent here. Gravity is hypothesized to be mediated by a massless spin-2 boson called the graviton. However, because it is orders of magnitude weaker than the other forces, not well accounted for in the Standard Model, and has yet to be directly observed, we can safely omit the graviton here.

Table 1.1: Standard Model quarks.

Symbol	Name	Electric Charge	Approximate Mass (MeV) [8]
u	Up	$+2/3$	4 (lattice simulation)
d	Down	$-1/3$	4 (lattice simulation)
c	Charm	$+2/3$	1240 (continuum extraction)
s	Strange	$-1/3$	95 (lattice simulation)
t	Top	$+2/3$	172600 (CDF/D0 [7])
b	Bottom	$-1/3$	4200 (continuum extraction)

Table 1.2: Standard Model leptons.

Symbol	Name	Electric Charge	Approximate Mass (MeV) [8]
ν_e	Electron Neutrino	0	< 0.003
e	Electron	-1	0.511
ν_μ	Muon Neutrino	0	< 0.19
μ	Muon	-1	107
ν_τ	Tau Neutrino	0	< 18.2
τ	Tau	-1	1777

Both quarks and leptons are spin-1/2 fermions and have the property of "flavor", which

Table 1.3: Standard Model gauge bosons.

Name	Force	Electric Charge	Approximate Mass (GeV) [8]
photon γ	Electromagnetic	0	0
gluon	Strong	0	0
$W^{\pm}$	Weak	± 1	80
Z^0	Weak	0	91

describes the difference in species for quarks and generation for leptons. Each flavor has its own quantum number; here isospin differentiates up and down quarks. Strange quarks have "strangeness", charm has "charmness", and so on. Similarly, electrons and electron neutrinos have electron lepton number, muons and muon neutrinos have muon lepton number, etc. Besides the obvious mass differences, quarks and leptons also differ by the absence of baryon number for leptons, as well as which forces they interact with. Quarks experience strong, weak, and electromagnetic forces; leptons do not interact strongly. Furthermore, neutrinos only interact weakly.

Table 1.4: Fundamental forces important in the Standard Model [1].

Force	Range (m)	Relative Strength	Interacts With
Strong	10^{-15}	1	Quarks, gluons
Electromagnetic	infinite	10^{-2}	Any electrically charged particle
Weak	10^{-18}	10^{-5}	Quarks, leptons

Of the three forces seen in Table 1.4, the Weak force is the appropriately named weakest. As opposed to the electromagnetic and strong forces, the Weak force is not involved in the formation of bound states. Aside from general momentum conservation requirements, it is also not the source of any push or pull. Instead it can best be understood as the force mediating flavor–changing and some leptonic interactions. A familiar example of a Weak process is the following neutron decay:

$$n \rightarrow p + e^- + \bar{\nu}_e \tag{1.1}$$

Known as β^- decay, the process evolves as seen in Figure 1.2. One of the down quarks within a neutron emits a W^- and becomes an up quark. The W^- then converts immediately into an electron and a neutrino. Electromagnetic and strong forces both conserve species, so the weak force is the only available decay channel. Eventually all higher generation particles decay into the first generation quarks and leptons via Weak decays. This explains why the visible universe is composed of the first generation particles and their constructs.

A different example of weak decay can be found in the comparison of the Δ^+ and Σ^+. Both are positively charged particles around 1.2GeV. Both also prominently decay to $n+\pi^+$. When we observe the lifetimes of these similar particles, we find a major difference. The $\Delta^+ \rightarrow n + \pi^+$ decay proceeds rapidly, on the order of 10^{-23}s, whereas $\Sigma^+ \rightarrow n + \pi^+$ takes $\sim 10^{-10}$s. Comparing the quark content before and after the decay, we can clearly discern what forces can allow the respective decays.

The $\Delta^+ \rightarrow n + \pi^+$ involves $uud \rightarrow udd + u\bar{d}$. This only requires the production of a down/antidown pair, which the strong force can provide. $\Sigma^+ \rightarrow n + \pi^+$ requires more. With $uus \rightarrow udd + u\bar{d}$, in addition to creating a down/antidown pair as in Δ^+, the decay must also replace a strange quark with another down. This flavor change is only possible within a Weak decay.

The electromagnetic force is well understood, being the force responsible for the electromagnetic spectrum, charged pith balls and other miscelaneous experiments common to introductory physics classes, and most chemical interactions including the formation of chemical bonds. Charged bodies interact with each other and extraneous electromagnetic fields via the exchange of photons. Quantum Electrodynamics (QED) is the theoretical framework for understanding such interactions at their most fundamental. QED is a perturbative field theory whose development foreshadowed Quantum Chromodynamics (QCD), the theory of strong interactions.

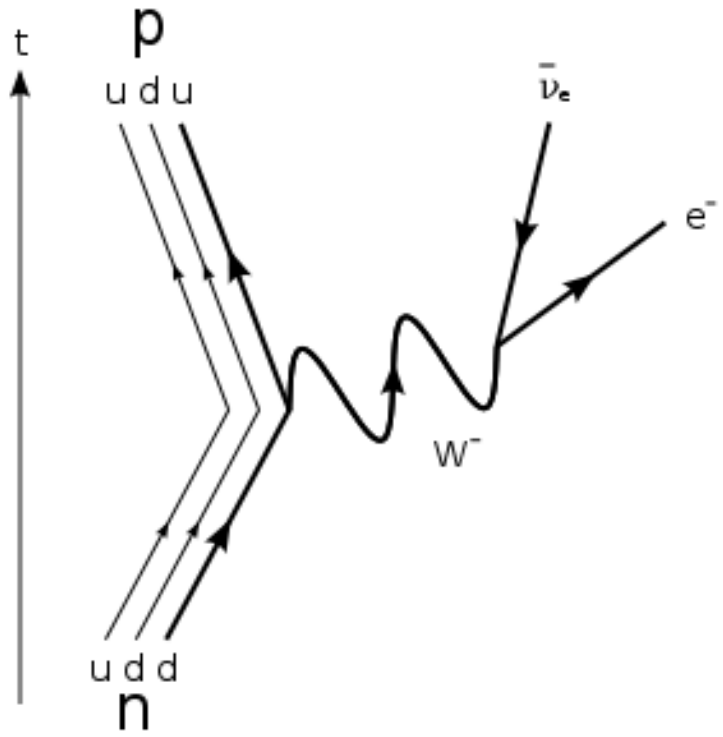

Figure 1.2: A diagram of beta decay (Eq. 1.1). A d quark decays via the weak force to result in a u quark still bound in the hadron, an electron, and an antielectron neutrino [9].

QCD describes the force responsible for the formation of protons and neutrons, their binding within nuclei, and the decay of very short–lived particles, such as the previously mentioned Δ^+. Similar to QED, the strong force acts on objects that carry a "color" charge. Each quark carries a "red", "green", or "blue" charge, and each anitquark an anticolor. It should be noted the colors associated with the strong force are only state labels — convenient analogies to the colors in the visual EM spectrum. A particle is said to be "white", or colorless, if the constituent quarks contain equal amounts of red, green, and blue or color and anticolor in equal measure. The strong force operates under color confinement, which forbids the observation of a net color charge; hadrons are observable colorless quark states. Hadrons containing three quarks equal amounts of the three color or anticolor charges are called baryons, which include the nucleons and the discussed hyperons. Mesons, e.g. pions, kaons, and η's, are hadrons composed of a quark with color and an antiquark with anticolor charge.

The requirement of colorless observable states is due to a key difference between the electromagnetic and strong forces: the gluon itself carries color charge. Though the photon carries the electromagnetic force between charged particles, it does not have its own charge. Thus the electric force between charged particles is nearly constant at large distances, but increases as the particles get closer. With strong interactions, however, as color charged particles get closer, such as quarks colliding in high energy interactions, the effective strong force decreases. The strong force increases as two quarks within a hadron are separated, making it more difficult to pull the two apart. If enough energy is put into dividing a pair quarks in a hadron another pair of quarks will appear from the strong field, creating two colorless hadrons that allow the original pair of quarks to separate.

1.2 An Introduction to Dalitz Plots

Describing hadron formation is generally intractable through analytic means. Outside the realm of peturbative QCD, the same features that produce hadronic observable states quickly overwhelm all but numerical approximations and high performance computing. These meth-

ods, including most prominently Lattice QCD, require more than the experimental verification necessary of all theoretical predictions. A review of Lattice QCD can be found in the PDG [8]. Properties such as exclusive charm branching fractions generally cannot be accurately predicted and must be found experimentally.

The D meson has proven to be an ideal system to study strong sector dynamics. Unlike the proton, D states are relatively free of the gluon "sea" that heavily populates protons. It also has advantages over its heavier analog, the B meson. Much of the strong dynamics vital to the understanding of B decays are larger in D. In addition to decay tagging being easier [10], certain analyses are impossible [11] in decays other than two D mesons decaying from a common parent.

Many of the decay channels available to the D meson consist of three or more body final states; these are predicted to primarily proceed through the production of a intermediate resonance [12]. For Weak nonleptonic three-body decays, the primary technique for analyzing this intermediate structure is the Dalitz Plot. This method was first used by its namesake R. H. Dalitz [13] to study the $\tau - \theta$ puzzle, the resolution of which found both were different parity decays of the same basic meson, what we now reference as the kaon. For a given resonance, there are three primary results derived from a Dalitz plot analysis: relative amplitudes, phases, and branching fractions.

The quantum description of the decay rate of a particle of mass M into n bodies is given by the formula

$$d\Gamma_n = \frac{(2\pi)^4}{2M}|\mathcal{M}|^2 d\Phi(M; p_i \dots p_n) \tag{1.2}$$

where

$$d\Phi(M; p_i \dots p_n) = \delta^4(M - \sum_{i=1}^{n} p_i) \prod_{i=1}^{n} \frac{d^3 p_i}{(2\pi)^3 2E_i}$$

is the general invariant phase space, and $|\mathcal{M}|^2$ is the Lorentz invariant amplitude. For a

psuedoscalar such as a D or B meson decaying into three psuedoscalars, the phase space is much more simple. The three final state particles each has a 4-momentum, representing twelve degrees of freedom. However not all of these degrees are independent. As summarized in Table 1.5, because our knowledge of the system, we can eliminate all but two degrees of freedom. If we combine masses $m_{12}^2 = (m_1+m_2)^2$ and m_{23}^2, then m_{13}^2 is completely determined and we have an ideal phase space to see resonances. Making the necessary integrations, we derive

$$d\Gamma_n = \frac{|\mathcal{M}|^2}{32(2\pi)^3 M^3} dm_{12}^2 dm_{23}^2 \tag{1.3}$$

which is the standard form of the decay rate on the Dalitz Plot. As seen in Figure 1.3, the limits of the Dalitz plot are kinematically determined. Additionally, the shape of the plot will also be different if there are identical particles in the final state, e.g. $D^{\pm} \to K_s^0 K_s^0 K^{\pm}$. If there are no resonances in the final state, events will populate the Dalitz plot evenly; any increased or decreased density of events on the plot are primarily due to the presence of resonances.

Table 1.5: Daltiz Plot Degrees of Freedom.

Constraint	DOF	Notes
3 Final State 4-Momenta	12	Each final particle has a 4-momentum
Euler Angles	- 3	Pseudoscalar Parent has no Preferred Angle
Conservation of Momentum	- 3	$\vec{p_3} = -(\vec{p_1} + \vec{p_2})$
Conservation of Energy	- 1	$E_3 = M_D - E_1 - E_2$ (In D Rest Frame)
Known Masses	- 3	$m_D = m_1 + m_2 + m_3$, $m_D = (M_D; \vec{0})$
Remaining D.O.F.	2	Can use $m_{12}^2 = (m_1 + m_2)^2$, m_{23}^2, etc.

The invariant amplitde $|\mathcal{M}|^2$ encapsulates all of the dynamics of the decay of M into a given set of final daughters. Each resonant decay channel has its own matrix element, an imaginary phase term, and an amplitude that is positve real by construction. Thus the total invariant amplitude takes the form

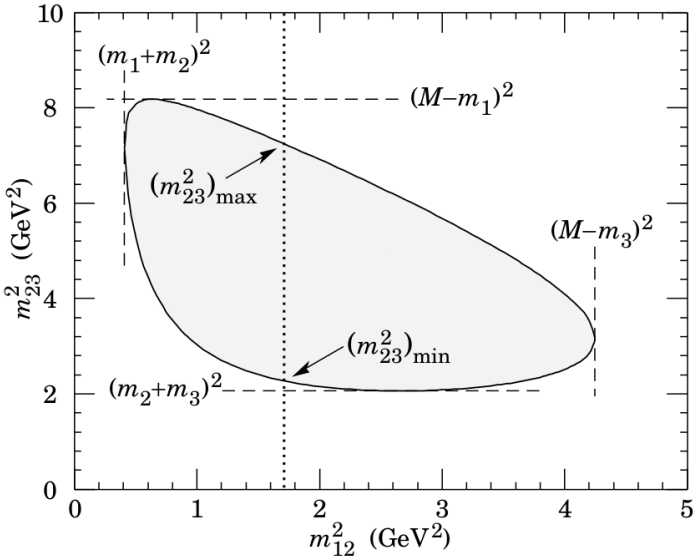

Figure 1.3: A diagram of a Dalitz plot. The shape of the plot is determined by the kinematics of the decay. A more complete discussion of particle kinematics can be found in the PDG [8].

$$\mathcal{M}(D \to abc) = \mathrm{a}_{nr} e^{i\varphi_{nr}} + \sum_n \mathrm{a}_n e^{i\varphi_n} \mathcal{A}_n \tag{1.4}$$

where a_n, φ_n, and $\mathcal{A}_n$ are the amplitude, relative phase, and dynamics matrix element of the nth resonance, respectively. The $\mathrm{a}_{nr} e^{i\varphi_{nr}}$ term is for a nonresonant D^0 decay. The normalization of $|\mathcal{M}|^2$ is arbitrary, so we set it to

$$\int |\mathcal{M}|^2 d\mathcal{DP} = 1 \tag{1.5}$$

whose integral is over the Dalitz plot. This means the analysis is only sensitive to relative phases and amplitudes. In practice, one resonance is set to $\mathrm{a} = 1$, $\phi = 0$, and the rest allowed to float against this fixed value. In the next section I will discuss previous attempts to deal with this normalization. Since different analyses are free to choose different resonance models and fixed resonances, we require a result that are independent of such details. Thus I also calculate the fit fraction [12] over the plot for each resonance,

$$\text{Fit Fraction}_r \equiv \frac{\int |\mathrm{a}_r e^{i\varphi_r} \mathcal{A}(abc|r)|^2 d\mathcal{D}\mathcal{P}}{\int |\Sigma_j \mathrm{a}_j e^{i\varphi_j} \mathcal{A}(abc|j)|^2 d\mathcal{D}\mathcal{P}} \tag{1.6}$$

In general the sum over the fit fractions is not equal to one due to interference between resonances.

The observation of resonance interference is another feature of Dalitz analysis, but it is not without complication. In decays involving a K^+K^- final state, such as $D^0 \to K^0_s K^+ K^-$, multiple resonances appear at the same place on the Dalitz Plot. $\phi(1020)$ is a well known "strangeonium" meson with $s\bar{s}$ composition and narrow width that appears near 1GeV^2. Two more, $a_0(980)$ and $f_0(980)$, are both wide resonances with largely unknown structure that should also contribute to this decay channel at the same mass; see the $f_0(500)$ Note in the PDG [8]. As seen in Table 1.6, while both have a secondary decay in K^+K^-, they have two different dominant decay channels. If we can utilize any of the information from the fit of a non-interfering channel on the $D^0 \to K^0_s K^+ K^-$ plot, we can attempt to accurately measure the contribution of these two resonances to the specific final state.

Table 1.6: Wide Scalar Mesons $a_0(980)$ and $f_0(980)$ Compared [8].

Property	$a_0(980)$	$f_0(980)$
Mass	$980 \pm 20\text{MeV}$	$990 \pm 20\text{MeV}$
Width	50–100MeV	40–100MeV
$I^G(J^{PC})$	$1^-(0^{++})$	$0^+(0^{++})$
Dominant Decay	$\eta\pi$	$\pi\bar{\pi}$
Next Largest Decay	$K\bar{K}$	$K\bar{K}$

So what properties are unchanged between the differing decay channels? There are two approaches that suggest themselves. Assuming a resonance with at least two channels "1" and "2" share a common amplitude, we can create a fitting "penalty term" that forces the amplitude in an interfering channel to the value found in the non-interfering channel. In the Dalitz method, amplitudes and phases are relative; we fix one resonance, often the largest, and fit the rest with respect to this. This in practice means the amplitudes, or more properly

the absoulte value of $|\mathrm{a}|^2$, must first be normalized to be compared. We must also note $|\mathrm{a}|^2$ represents

$$\mathcal{BF}_1 * \mathcal{BF}_{D^0 with mode1} = |\mathrm{a}_1|^2 \tag{1.7}$$

Thus the fit amplitude of a resonance into its "1" channel can be equated to its "2" channel amplitude by scaling each by the branching fraction of the resonance into that channel, and the fraction of the parent into a mode containing the channel. We can adjust for the relative fit by dividing by the sum of amplitudes in the channel as seen in Eq. 1.8. In equating amplitudes, we are oblivious to the interference on the plot.

$$\frac{c_1|\mathrm{a}_1|^2}{\mathcal{BF}_1\mathcal{BF}_{D^0 with mode1}} = \frac{c_2|\mathrm{a}_2|^2}{\mathcal{BF}_2\mathcal{BF}_{D^0 with mode2}} \tag{1.8}$$

where

$$c = \left(\sum_i \frac{|\mathrm{a}_i|^2}{\mathcal{BF}_i}\right)^{-1}$$

is the normailiztion factor.

If instead we equate the Fit fraction of the shared resonance, we explicitly deal with interference. Eq. 1.9 includes the scaling by branching fraction for the resonance mode and parent mode.

$$\frac{\mathcal{FF}_1}{\mathcal{BF}_1\mathcal{BF}_{D^0 with mode1}} = \frac{\mathcal{FF}_2}{\mathcal{BF}_2\mathcal{BF}_{D^0 with mode2}} \tag{1.9}$$

1.3 Current Experimental Status and Theoretical Predictions

The CLEO collaboration previously attempted to tackle the discrepancy between $f_0(980)$ as it appears in $D^0 \to K^0_s\pi^+\pi^+$ versus $D^0 \to K^0K^+K^-$ [14]. Since it was noted that $D^0 \to K^0K^+K^-$ should have an $a_0(980)K^0_s$ mode that is difficult to separate from the $f_0(980)$ contribution, CLEO set out to study $a_0(980)$ in a non–interferring mode. CLEO in

its II.V configuration, which will be discussed in the next chapter, was able to perform a Dalitz analysis on $D^0 \to K^0_s\pi^0\eta$, extract its branching fraction relative to $D^0 \to K^0_s\pi^0$, and find the two leading resonance candidates $a_0(980)K^0_s$ and $K^*(892)\eta$. Though this analysis adds to the knowledge of three body charm decays, question of how to separate $f_0(980)$ from $a_0(980)$ was left unresolved.

The BABAR collaboration later performed a Daltiz plot analysis on $D^0 \to \bar{K^0}K^+K^-$, also seeking information on charm three body decays as well as hoping to discover more information on $f_0(980)$ from $a_0(980)$, both of which are possible exotic strong states [15]. BABAR did not consider an $f_0(980)$ contribution, reasoning from a comparison between $K^0_sK^+$ and K^-K^+ that the lack of excess events in K^-K^+ made an $f_0(980)$ component unlikely. They calculate an upwards value for the contribution and omit amplitude and phase values. The possibility of interference between $a_0(980)$ and $f_0(980)$ is not considered.

In contrast to the BABAR study of $\bar{K^0}K^+K^-$, the FOCUS collaboration's "Study of the $D^0 \to K^+K^-\pi^+\pi^+$ decay" [16] includes the $f_0(980)\pi^+\pi^+$ channel in their overall fit, but explicitly exclude the corresponding $a_0(980)\pi^+\pi^+$ mode. FOCUS finds a relative lack of statistics and the fact $a_0(980)$ primarily decays into $\eta\pi$ are reasons for excluding $a_0(980)\pi^+\pi^+$.

CHAPTER 2: THE CLEO-C EXPERIMENT

Knowledge of an experimental apparatus is nearly as important as the data it produces. Here I will describe in brief the device used in this thesis. A more detailed description can be found elsewhere [17].

2.1 CESR

The Cornell Electron Storage Ring (CESR) is the source of colliding electrons and positrons at Cornell University. It has a circumference of 768 meters, extending from Wilson Laboratory through the tunnels underneath the adjacent athletic facilities and parking lots. CESR began operation in 1979.

Electrons begin the process. Emitted from a heated filament, these electrons are accelerated by special 30 meter long linear accelerator (LINAC). The LINAC uses microwave electric fields to bring the electrons up to 150 MeV at an intermediate point, at which time they strike a tungsten fixed target. More electrons, along with positrons and x-rays emerge from the interaction. The positrons are selected, and accelerated to energies between 150 and 300 MeV before being injected into the second acceleration stage: the synchrotron.

A synchrotron consists of cells to accelerate particles to the desired energies, and various magnets to selectively focus the particle beams. CESR's synchrotron has four 10-foot long radio frequency accelerating cells. The positrons make about 4000 clockwise orbits before being injected into CESR. This occurs at a rate of about 60 injections per second. Once CESR has the proper positron beam current, electrons take the analogous path in the system. Collected after the tungsten collision, electrons are accelerated through the system like the positrons before them, except in a counterclockwise direction. At current, CESR maintains both an electron and positron beam in the same tunnel, travelling in opposite directions. The beam is not a continuous object; a normal beam consists of up to nine "trains", each containing between three and five "bunches".

Each beam travels very close to the speed of light, with half of the total energy re-

quired for experimentation. CESR, like other storage rings, are specialized synchrotrons that maintain beams at experimental energy versus accelerating to energy. All charged particles, electrons/positrons in particular, lose energy as they circulate around the ring due to synchrotron radiation. CESR has superconducting RF cavities to replace energy lost to radiation, plus liquid cooling to remove heat deposited in the ring. In two stations, this synchrotron radiation is extracted, and used for various material science studies. These stations make up the Cornell High Energy Synchrotron Source (CHESS).

Since CESR stores beams for up to an hour, care must be taken to keep a well maintained vacuum and focusing to prevent collisions with the chamber walls. Beams consist of bunches of electrons and positrons, which introduces its own focus concerns. Like charged particles repel, spreading a given bunch. CESR counteracts this spread using quadrapole and sextapole focusing magnets.

2.2 Electron/Positron Collisions

When bunches of positrons and electrons coincide at the interaction point, there is a probability they will collide. When they collide they will annihilate, creating a virtual massive photon, $\gamma^\star$, which will immediately decay to a product that depends on the center of mass energy.

In the CLEO-c experiment, the beams are tuned to three primary energies: $\approx$ 3680MeV, $\approx$ 3770MeV, and $\approx$ 4770MeV. These correspond to ψ', ψ'', and $D_s^\star \bar{D}_s$, respectively. As an example, if the center of mass energy is 3774MeV, the reaction event is

$$e^- e^+ \rightarrow \gamma^\star \rightarrow \psi'' \tag{2.1}$$

The choice of energy depends on what the CLEO collaboration wishes to study. The ψ'' decays to $D^0\bar{D}^0$ and D^+D^- $(52 \pm 5)\%$ and $(41 \pm 4)\%$ of the time, respectively [8]. The D mesons are produced back to back nearly at rest.

CESR operation data is divided into "runs" and "datasets". A run consists of a single

e^+e^- fill, which can contain up to 10^4 events. A dataset contains a series of runs that are related by machine conditions, including the center of mass energy. This analysis is performed on datasets 31-33, 35-37, and 43-46. These data sets represent a total of 818 pb^{-1} of integrated luminosity taken at the ψ'' energy. When we multiply the luminosity by the cross section of $e^-e^+ \to D^0\bar{D}^0$ [18], we determine we have data on about three million $D^0\bar{D}^0$ pairs.

2.3 Previous Incarnations of CLEO

CLEO, so named to compliment CESR, was built along with CESR in the late 1970s [10]. It was constructed in the south hall of Wilson Laboratory, centered around one of two interaction points. A second experiment, the now defunct CUSB, was housed in the smaller north hall. Among CLEO's first tasks were to verify the then-recently discovered Υ states: $\Upsilon(1S)$, $\Upsilon(2S)$, and $\Upsilon(3S)$, as well as discover a fourth, $\Upsilon(4S)$, near the $B\bar{B}$ threshold. Various studies surrounding Υ and B mesons continued throughout the 1980s with a short shutdown in 1986 to improve resolution and particle identification. CLEO II came online in 1989 after a yearlong shutdown. Of the many upgrades, two of the most notable were the installation of the cesium iodide (CsI) calorimeter and the new muon chambers.

1995 saw the beginning of CLEO II.V operation. A new silicon detector near the interaction point allowed for better vertex resolution. A major focus in this era was measuring the bottom-related Cabibbo-Kobayashi-Maskawa matrix (CKM) matrix elements. Five years later, CLEO III came online, bringing with it an improved silicon detector, a new drift chamber, and a ring imaging Cherenkov (RICH) detector. It too was focused on B mesons, primarily from $\Upsilon(4S)$.

2.4 The CLEO-c Detector

Faced with the advent of high-luminosity B-Factories and the need for a better understanding of strong interaction effects, the CLEO collaboration decided to change focus to the lower energy charm sector. In order to better serve this new priority, the silicon vertex detector was replaced by an inner drift chamber and the magnetic field strength reduced

from 1.5T to 1.0T. This new detector was dubbed CLEO-c [17]. For a diagram, see Figure 2.1.

D mesons decay within the radius of the interaction region, producing a shower of particles that will survive to be detected in different layers. Electrons, positrons, and other charged particles will deposit energy in the drift chambers and either end their flight or decay by the time they are detected in the calorimeter. K-short (K_s^0) will most often decay to a $\pi^+\pi^-$ pair in the drift chambers. Photons will go largely unnoticed by the drift chambers and deposit energy in the calorimeter. Neutral pions (π^0) and etas (η) will similarly go undetected by the drift chambers, being detected by their decay into a photon pair. Muons will deposit energy in all layers of the detector including the appropriately named Barrel Muon Chambers. K-long (K_l^0) and neutrinos mostly escape detection, and must be reconstructed from missing energy and momentum.

Before we continue, we should make note of our coordinate convention. We use cylindrical coordinates, with our origin at the interaction point. The z axis coincides with the beam line in the direction of the positron beam, with r the distance from the beam line and ϕ the angle about the beam line. The Cartesian y axis is normal to the ground.

2.4.1 TRACKING

As charged particles emerge from the interaction region, their trajectories are curved by the magnetic field maintained within the detector. By measuring this track in a fixed field strength, we have a measure of the particle momentum.

The two innermost layers of CLEO-c, the inner and outer drift chambers, are designed to detect these tracks. An image of the inner drift chamber is shown in Fig. 2.2. A partial schematic of the outer drift chamber is shown in Fig. 2.3. Both chambers consist of cylindrical wires stretched between metal endcaps, contained in a helium-propane (60:40) gas mixture. There are two types of wire. Sense wires are gold-plated tungsten 20µm in diameter, maintained at a voltage difference of about 2000V relative to the second type. Field wires are gold-plated aluminum with a diameter of 110µm. These wires are used to

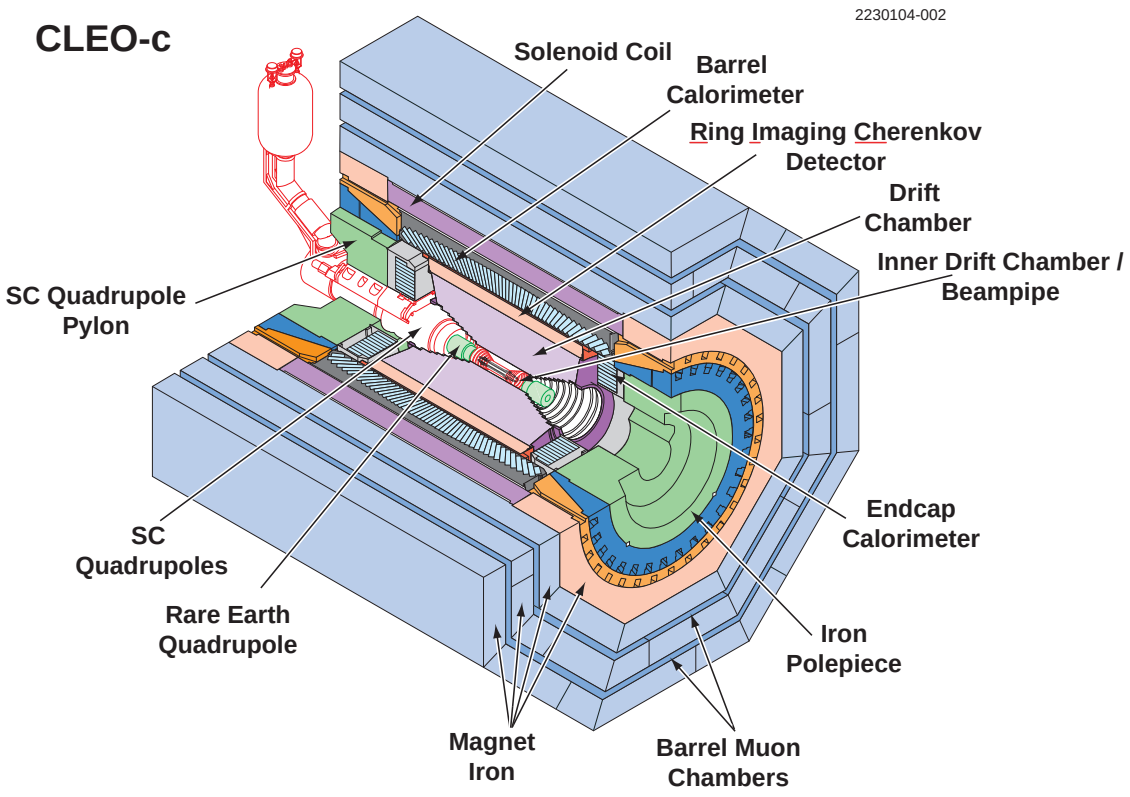

Figure 2.1: A diagram of the CLEO-c detector [19].

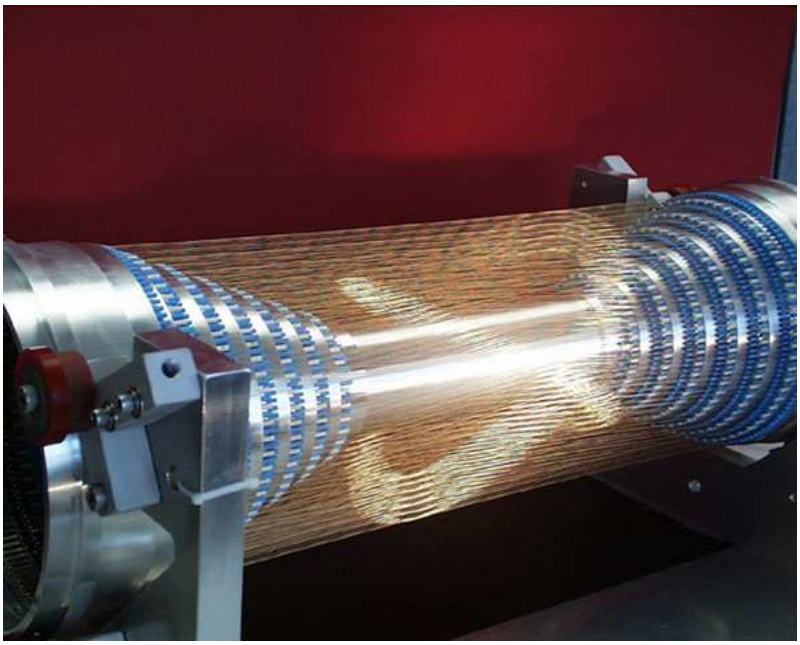

Figure 2.2: A picture of the inner drift chamber (ZD) at CLEO-c. The reflections show the stereo twist [20].

shape the electric field in the chamber in order to create cells, with a single sense wire to each cell. As seen in Fig. 2.3, each cell is roughly square.

As a charged particle passes through the drift chambers, it deposits energy in the gaseous medium, creating electron-ion pairs. As the electron is attracted to the sense wire it collides with more of the medium, creating more electrons. This cascade of electrons produce a current in the sense wire that is read out at the end of the chamber. The charged particle will continue this ionization process for the duration of its flight in the drift chambers. The current readouts, or hits, are turned into position measurements in the r–ϕ plane.

Most of the cells are axial; they are strung parallel to the beam line. However some are set at a stereo angle, which allows us to resolve position in the z axis as well. In software, we combine these hits to reconstruct the three dimensional path, or "track", the particle took through the detector. The direction of the curvature of the track tell us whether the charge was positive or negative. The magnitude of curvature tells us its momentum.

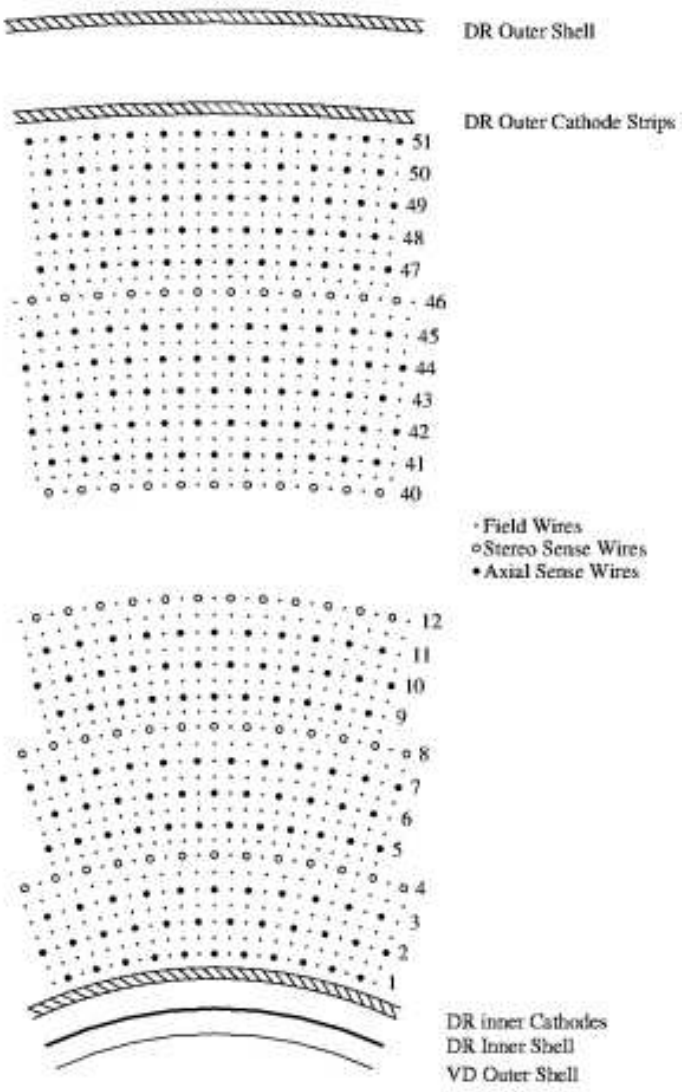

Figure 2.3: A schematic of the outer drift chamber (DR) at CLEO-c, showing the placement of field and sense wires [21].

2.4.2 PARTICLE IDENTIFICATION

The drift chambers' function in track reconstruction complement their other important function: particle identification. As a charged particle traverses the drift chamber, it loses energy as a function of velocity due to interaction with the chamber gas and wires. This specific energy loss, dE/dx, will change as a function of velocity. As we see in Fig. 2.4, beyond approx. 700MeV, dE/dx becomes less useful in differentiating $K^{\pm}$, $\pi^{\pm}$, and protons. At these energies we need the next outer layer of CLEO-c, the Ring Imaging CHerenkov (RICH) detector.

The RICH chamber (see Fig. 2.5) itself contains several layers. After leaving the outer drift chamber, the charged particle enters a layer of lithium fluoride (LiF) radiators, which have a high index of refraction. The particle is still traveling slower than the speed of light in vacuum (c), but faster than the speed of light in LiF. As it enters the radiators, the particle emits very ultraviolet photons in a cone similarly to a supersonic object creating a sonic boom in air. Since we need to detect the opening angle, which depends on the particle velocity, the cone is allowed to expand in a layer of pure nitrogen gas. Past this expansion gap, they are detected as a circle in the third layer, which consists of multiwire proportional chambers immersed in methane-triethylamine (TEA) gas mixture. The radius of this circle determines velocity. Combined with a momentum measurement from the tracking system, the particle is identified by calculating its mass.

2.4.3 CALORIMETRY AND MUON DETECTION

Beyond the RICH detector, the cesium iodide (CsI) electromagnetic calorimeter is tasked with determining the energy of EM showering particles and photons. The calorimeter consists of 7800 CsI crystals, each $5 \times 5 \times 30$cm, with silicon photodiodes for detection. The crystals are arranged such that a 5×5cm face is directed at the interaction region. As the target particle enters a crystal, it initiates a shower of photons that travel to the opposite end to be detected by the photodiodes. The light intensity is proportional to the energy of the incident particle.

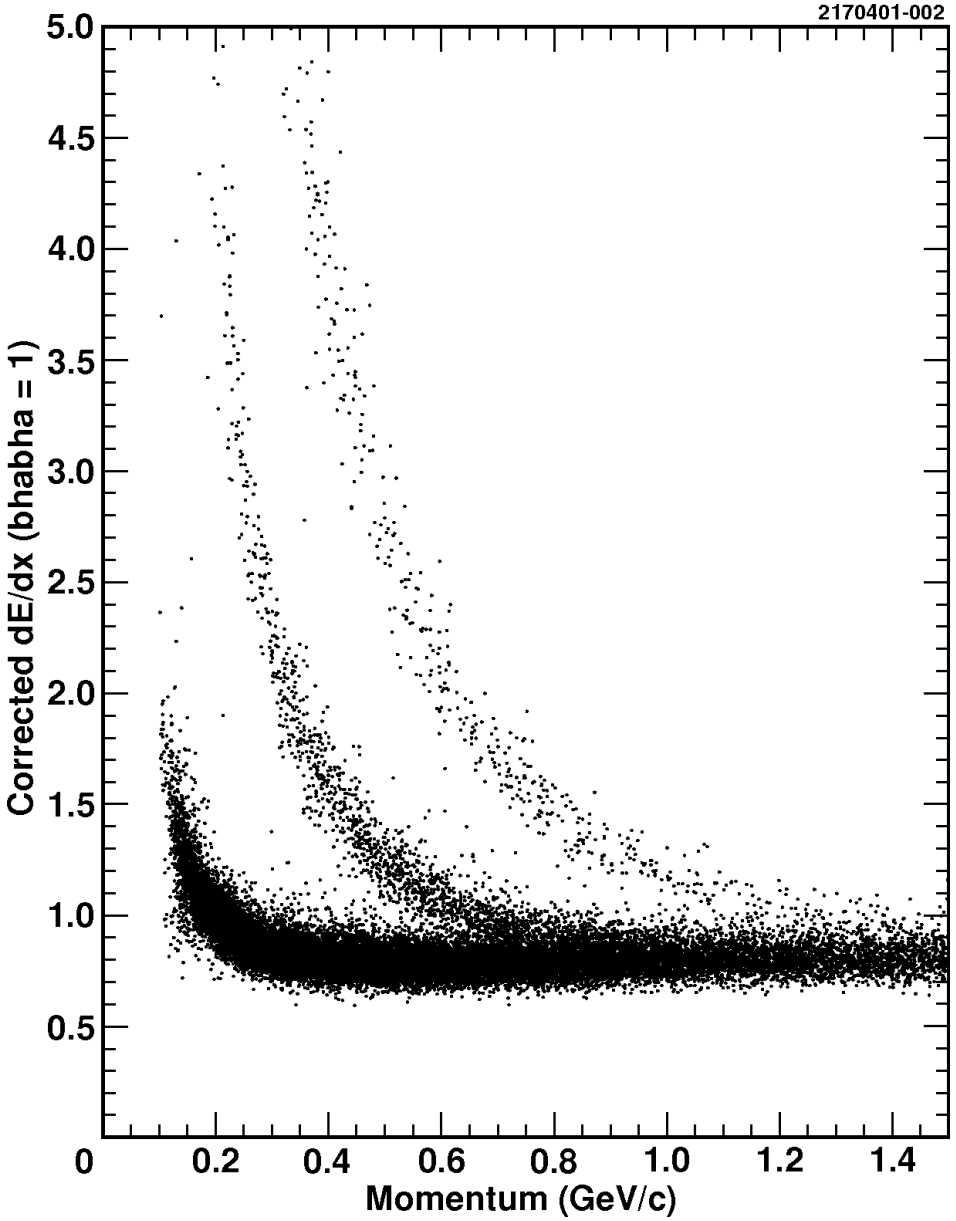

Figure 2.4: dE/dx plots from CLEO III. The bottom stripe of points consists of charged pions, the stripe in the middle consists of charged kaons, and the upper and faintest stripe consists of protons [17].

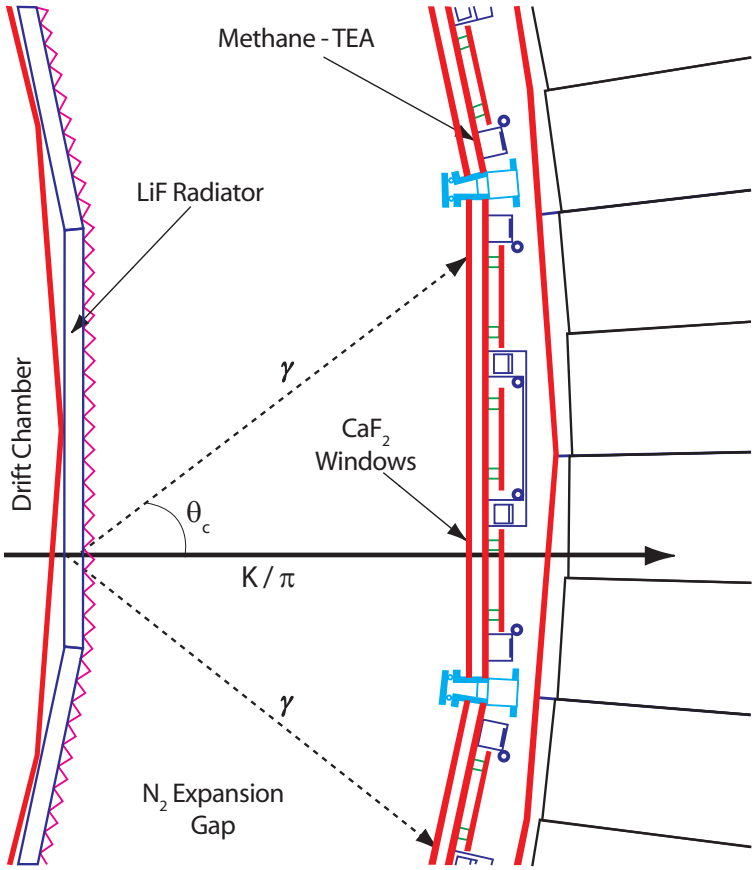

Figure 2.5: A cutaway diagram of the CLEO-c RICH detector, showing the LiF radiator (left), expansion gap, and detector apparatus (right) [24].

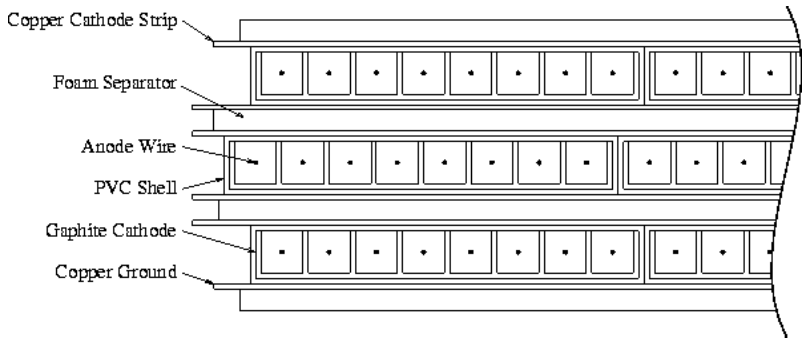

Figure 2.6: A cross section diagram of the CLEO-c Barrel Muon Chambers [23].

The final layer of CLEO-c consist of several layers of iron that serve as flux return for the superconducting magnet. Interspersed between magnet iron are the Barrel Muon Chambers. Like the drift chambers, the Barrel Muon Chambers consist of wires immersed in gas mixture that detect the trajectory of passing charged particles. As seen in Figure 2.6, instead of multiple field and sense wires occupying a common chamber, each anode wire is contained in graphite–coated extruded PVC tubes in a 50% argon and 50% ethane gas mixture [22]. The graphite of the plastic tubes acts in a similar fashion to the field wires of the drift chambers. 8cm copper cathode strips run perpendicular to the tubes to properly determine position.

2.4.4 TRIGGERING, DATA ACQUISITION, AND EVENT RECONSTRUCTION

A given e^+e^- collision run contains far more results than can be saved to storage for study. Coupled with our inability to analyze decays in real time, we require a means to quick assess how interesting the given event is. This evaluation is called triggering, and it has several components.

Beginning with the drift chambers, the readouts are checked against signatures of events with objects that travel far enough in the detector to be useful. Triggering also requires that three of the four stereo layers in the outer drift chamber receive hits. The tracking trigger rejects interesting events fewer than 1% of the time. The calorimeter data is gathered next,

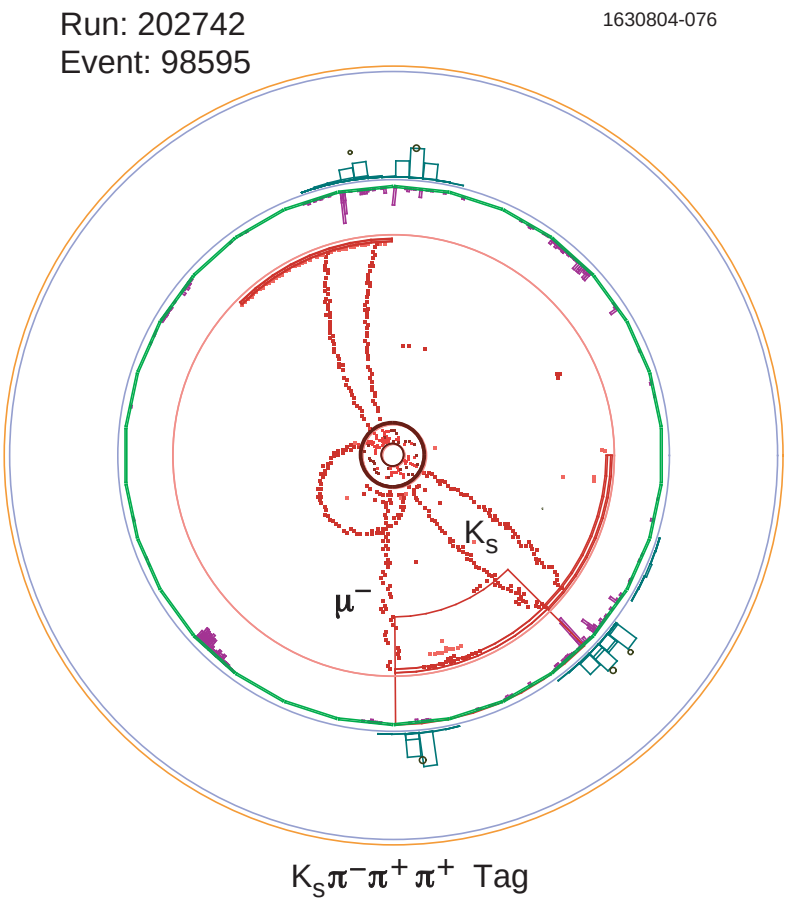

Figure 2.7: The event display for a CLEO-c event. Tracks, RICH response, and showers are shown.

locating showers by grouping adjacent crystals into overlapping tiles.

Tracking and calorimeter data are fed into the global trigger which decides if the event fits into one of eight categories of interesting events. If it matches one, the rest of detector information is gathered. This coincides with a period of about 20μs during which the detector is blind to additional events. Event displays generate for interesting events, which show the transverse plane in the detector. Figure 2.7 shows an example display, with responses from all affected layers.

The data acquisition system (DAQ) digitizes about 400,000 readouts from all of CLEO-c. Depending on the event, this can represent more than 5MBps. As the DAQ operates, CLEO-c resumes data taking. If another interesting event passes triggering, the readouts for

this new event is placed in buffer for later processing by the DAQ. More software triggers downstream are used to do additional background minimization before data is stored to disk or tape.

The collaboration has a mature and robust set of software libraries written in C++ that allow us to turn hits and showers into physics "objects" that can be analyzed. This is done after triggering and DAQ, and is not casually related to data taking. From there, collaboration members write code in various compiled and scripting languages, commonly C++ along with shell scripts, to build our analyses. If the raw readout information is required, this too is available.

Most of the work of event reconstruction is performed by "pass2", which builds tracks, showers, and does loose particle identification. D meson analysis is of such importance to the collaboration that many studies, including our own, use data that has been pre-searched for D candidates. This "D Skim" [25, 26] takes pass2 objects to make combinations, looking for potential D "tags". If one combination passes the skim's cuts, the whole event is included in the skim for that dataset. Pass2 reconstructs anything it can, including any secondary decays, so the skimmer cannot determine what might be important without further analysis. A researcher can look for a specific decay(s) by invoking one of over 70 tagged $D\bar{D}$ or $D_s\bar{D}_s$ modes.

Since pass2 only performs basic selections, D Skim makes additional requirements. Tracks must be well reconstructed, originating close to the interaction point. The track's momentum must also be within bounds. Table 2.1 lists all of the track requirements. In order to differentiate between pions and kaons, we can utilize information from both dE/dx and RICH. Given the dE/dx information is availible, we calculate a χ^2 for the particle hypothesis

$$\sigma_h^2 = \left(\frac{dE/dx_{measured} - dE/dx_{predicted}}{\sigma} \right) \tag{2.2}$$

where h is either a pion or kaon. In the case of valid RICH information, the liklihoods L_K and

L_π are calculated based on the locations of the Cherenkov photons and track information [36]. We combine theses particle hypothesis tests in a log-likelihood calculation, whose value for a pion test is

$$\mathcal{L} = \sigma_K^2 - \sigma_\pi^2 + L_K - L_\pi \tag{2.3}$$

where $\mathcal{L} \geq 0$. For a kaon, Eq. 2.3 is used with the K and π subscripts switched. If the RICH gives an obviously wrong output, L_K and L_π will be omitted. The RICH outputs will also be omitted if the track momentum is below 700MeV or $|\cos\theta| > 0.8$. These rejections are due to the optimum momentum resolution and physical coverage of the RICH detector.

Table 2.1: Track quality cuts used by D Skim.

Cut	Description
$0.050 \leq p \leq 2.0$ GeV	p: track momentum
$\lvert db\rvert \leq 0.005$ m	db: closest dist. from track to interaction point
$\lvert z0\rvert \leq 0.050$ m	$z0$: same as db, except along beam axis (z-axis)
$\chi^2 \leq 100000$	χ^2: measure of how well raw output fits to shape of a track
hitfrac ≥ 0.5	(Actual # of tracking hits)/(expected # of tracking hits)
$\lvert\cos\theta\rvert \leq 0.930$	θ: angle track makes with the beam axis

Neutral particles, in particular K_S^0, π^0, and η, also receive extra selections. K_s^0 candidates are reconstructed using pairs of tracks that make a "vee", where both come from approximately the same vertex in the drift chambers. These tracks, which are not subjected to particle identification, must also have a total energy that is within 30MeV of the K_s^0 mass, 0.4976GeV. π^0 and η candidates are built from photon showers in the calorimeter. Among the cuts, as seen in Table 2.2, is photon minimum energy, which must be at least 30MeV and 50MeV for the π^0 and η respectively. η' are also built, but are not used in this analysis.

In order to build a D tag, the D Skim takes a list of these lighter reconstructed particles and tries to make D candidates from a list of known decay modes. Candidates that survive the D selections in Table 2.3 are included in the skim. Incuded D skim tracks, showers, and

Table 2.2: π^0 and η quality cuts used by D Skim.

Cut	Description
$E > 30(50)$ MeV	Shower energy: minimum for $\pi^0(\eta)$
$\frac{m_{measured}-m_{expected}}{\sigma} < 3$	Pull Mass, where σ is the resolution
$0 \leq m \leq 1000$ GeV	Unconstrained Mass: to remove pathological shower combinations
$\chi^2 \leq 100000$	χ^2: how well raw output fits to $\pi^0(\eta)$ originating from the interaction point
$\sigma_{max} \leq 1000\sigma$	Maximum deviation from $\pi^0(\eta)$ hypothesis

overall D candidates are also kinematically fit using the `FitEvt` [29] package; the fit results are stored along with the candidate.

Table 2.3: D candidate cuts used by D Skim. E_{beam} is one half the total energy of the e^+e^- collision.

Cut	Description
$M_{bc} > 1.83$ GeV	Beam constrained mass; $M_{bc} \equiv \sqrt{E_{beam}^2 - p_D^2}$
$\lvert\Delta E\rvert < 0.1$ GeV	$\Delta E \equiv E_D - E_{beam}$

2.5 Monte Carlo Simulations

Monte Carlo (MC) simulation [30] is an important application in the physics analysis tool set. This toolkit allows us to generate simulated events to test analysis techniques as well as determine efficiencies. Unlike actual data, simulated MC decays can be determined from the initial e^+e^- collision through to the final detected daughters.

MC simulation begins with the EvtGen program. Beginning with $e^+e^- \rightarrow \gamma^*$, EvtGen uses either the master file, called `DECAY.DEC`, or a user created file to simulate a random decay to the final daughters. `DECAY.DEC` contains the branching fractions and masses of every decay at CLEO energies known to the collaboration. These decay chains are processed through

cleog, a Geant4–based[1] software package that simulates how the detector behaves including random detector noise. What emerges from cleog are showers and other detector hits that can be run through the same pass2, etc. that are used for actual data. We emphasize MC must be treated carefully; EvtGen does not accurately represent every fine nuance of the Standard Model, let alone nature. Additionally, cleog is not a perfect model of the detector. Taken together they are, however, good tools that are often used to determine how often fake data seeps into signal.

There are two types of pre-generated MC. "generic MC" is simulated to only include $D\bar{D}$ events. This is also D skimmed, so users can readily use D tags from MC and data. The other variety is "continuum MC", which models the non-$D\bar{D}$ decays that are present in data, but not in generic. Each dataset has set of $D\bar{D}$, continuum, and the other varieties, each with several luminosities. The MC is generated with the specific detector conditions recorded the given dataset. For analyses that require a subset of decay channels, a user can create his or her own decay.dec, and specify what decays are modeled. This type is "signal MC".

2.6 Software

The CLEO collaboration has developed mature software tools that allow members to bootstrap an analysis quickly. In particuler, the `mkproc` tool in conjuntion with 14 optional modifiers builds a fully functional C++ analysis package, a "processor", capable of tasks from modified particle reconstrution to D Skim with full $D\bar{D}$ pair identification (so-called "double tags").

Processors are run in the `suez` framework, so named to complement the Caesar/Cleopatra naming scheme. Using scripts written in the TCL scripting language, `suez` handles any shared libraries, data/MC, and preprocessing tasks required for a given analysis. Small analysis tasks can be run on CLEO workstations. Large tasks, including large MC generation, can be handed off to the server farm using the Grid Engine queuing system.

[1] `http://http://geant4.cern.ch/`

2.7 Notable Results

As of 2014, the CLEO collaboration has published over 500 articles, many of great importance in high energy physics. Besides its inaugural bottom quarkonia studies [31] [32], CLEO has greatly contributed to the understanding of other quark/anitquark bound states[33] [34]. Measurements of charmless B meson decays are sensitive to the Cabibbo-Kobayashi-Maskawa (CKM) matrix element $|V_{ub}|$, and CLEO has discovered many forms of these decays [35]. CLEO has also produced one of the most comprehensive studies of the hadronic branching fractions of D mesons [36] [37].

CHAPTER 3: EXPERIMENTAL TECHNIQUE

3.1 Formalism

The matrix element $|\mathcal{M}|^2$ contains all of the resonance dynamics; with no resonances the events would uniformly populate the Dalitz plot subject to kinematic limits. In general the matrix element $\mathcal{M}_r$ for $D^0 \to rc$, $r \to ab$, as seen in Fig. 3.1, takes the form

$$\mathcal{M}_r = \sum_{\lambda} < ab|r_\lambda > T_r(m_{ab}) < cr_\lambda|D^0 > \tag{3.1}$$

where the sum is taken over the λ helicity states of r and $T_r(m_{ab})$ is the dynamical function describing the decay of r. Generally the matrix element depends on the total angular momentum of parent, the orbital angular momentum between r and c, the orbital momentum between a and b, and the momenta of c and either a or b in the r rest frame. A more complete overview of the formalism can be found in the Dalitz Formalism note in the PDG [8].

The dynamics function $T_r(m_{ab})$ derives from the S-Matrix formalism. An initial state i couples to a final state f by $S_{fi} =< f|S|i >$, where S is the unitary scattering operator that satisfies $S^\dagger S = SS^\dagger = I$. The Lorentz invariant transition $\hat{\mathrm{T}}$ is derived by separating the probability that the final state f is not equal to the intial state i

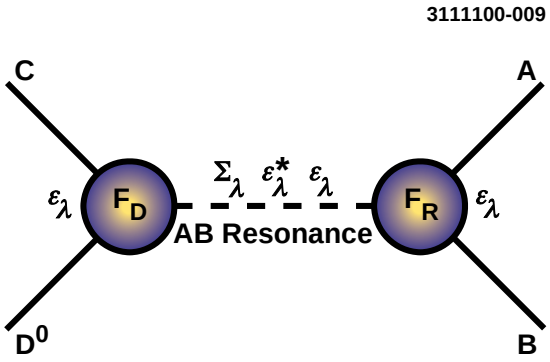

Figure 3.1: A diagram depicting a D^0 resonantly decaying to the ABC final state.

$$S = I + 2iT = I + 2i\rho^{1/2}\hat{T}\rho^{1/2} \tag{3.2}$$

where ρ is the diagonal phase space matrix, $\rho_{ii} = 2q_i/m$, and q_i is the momentum of a in the r rest frame for the decay channel i. For the single channel S-wave, $S = e^{2i\delta}$ satisfies unitarity and $\hat{\mathrm{T}}$ is

$$\hat{T} = \frac{1}{\rho} e^{i\delta} \sin\delta \tag{3.3}$$

We can use this single channel as a model of non-resonant decays.

There are three common formulations of the dynamical function: the Breit-Wigner, the Flatté and the K-Matrix formulations. In practice we utilize the first two; the K-matrix formulation is described elsewhere [38]. For a resonance r decaying into two spin-0 daughters a and b, the Breit-Wigner is

$$T_r(m_{ab}) = \frac{1}{m_r^2 - m_{ab}^2 - im_r\Gamma_{ab}} \tag{3.4}$$

The "mass-dependent width" Γ_{ab} depends on the invariant mass of ab (m_{ab}), the momentum p_{ab} of either daughter in the ab rest frame, the momentum p_r of either daughter in the r rest frame, the spin J of the resonance, and the width Γ_r. This is expressed as

$$\Gamma_{ab} = \Gamma_r \left(\frac{p_{ab}}{p_r}\right)^{2J+1} \left(\frac{m_r}{m_{ab}}\right) F_r^2 \tag{3.5}$$

F_r is a Blatt-Weisskopf penetration factor, also described in the Dalitz formalism note [8], which attempts to model the underlying quark structure. The factors as seen in Table 3.1, which separately model both the resonance and D^0, are normalized to 1 when $m_{ab} = m_r$. To be consistent with other experiments [39], we have chosen the radius, R, to be $5\mathrm{GeV}^{-1}$ and $1.5\mathrm{GeV}^{-1}$ for the D^0 and resonances, respectively.

The Flatté formulation is useful when two resonance channels open close to one another.

Table 3.1: Blatt-Weisskopf Penetration Factors

Spin	Form Factor F
0	1
1	$\frac{\sqrt{1+R^2p_r^2}}{\sqrt{1+R^2p_{ab}^2}}$
2	$\frac{\sqrt{(R^2p_r^2-3)^2+9R^2p_r^2}}{\sqrt{(R^2p_{ab}^2-3)^2+9R^2p_{ab}^2}}$

It takes the form

$$\hat{T}(m_{ab}) = \frac{1}{m_r^2 - m_{ab}^2 - i(\rho_1 g_1^2 + \rho_2 g_2^2)} \tag{3.6}$$

where $g_1^2 + g_2^2 = m_r\Gamma_r$. The coupling constants g_1 and g_2 couple a resonance to the two channels. For $a_0(980)$, $g_1 = g_{\pi\eta}$ and $g_2 = g_{K\bar{K}}$. The phase space terms are $\rho_1 = \rho_{\pi\eta}$ and $\rho_2 = \rho_{K\bar{K}}$ where

$$\rho_{ab} = \sqrt{\left[1 - \left(\frac{m_a - m_b}{m_{ab}}\right)^2\right]\left[1 + \left(\frac{m_a - m_b}{m_{ab}}\right)^2\right]} \tag{3.7}$$

For $f_0(980)$, the coupling constants are $g_1 = g_{\pi\pi}$, and $g_2 = g_{K\bar{K}}$; the phase space terms are $\rho_1 = \rho_{\pi\pi}$ and $\rho_2 = \rho_{K\bar{K}}$. Since the $m_{K^\pm} \neq m_{K^0}$, the charged and neutral kaon channels are taken to have the same coupling constant but different phase space factors. Therefore

$$\rho_{K\bar{K}} = \frac{1}{2}\left(\sqrt{1 - \left(\frac{2m_{K^\pm}}{m_{K\bar{K}}}\right)^2} + \sqrt{1 - \left(\frac{2m_{K^0}}{m_{K\bar{K}}}\right)^2}\right) \tag{3.8}$$

The simplest matrix element is a scalar resonance; it has the form

$$\mathcal{A}_0(abc|r) = F_D T_r(m_{ab}) F_r \tag{3.9}$$

where F_D and F_r are the same barrier penetration factors for the production of rc and ab

found in Table 3.1. The matrix element for a vector resonance is

$$\mathcal{A}_1(abc|r) = F_D(p_{D^0} + p_c)_\mu T_r(m_{ab}) \sum_\lambda \varepsilon_\lambda^{\mu*} \varepsilon_\lambda^\nu (p_a - p_b)_\nu F_r \tag{3.10}$$

where p is momentum and the sum is over the spin states of r. This sum evaluates to

$$\sum_\lambda \varepsilon_\lambda^{\mu*} \varepsilon_\lambda^\nu = -g^{\mu\nu} + \frac{p_{ab}^\mu p_{ab}^\nu}{m_{ab}^2} \tag{3.11}$$

We relax the transversality requirement on the vector resonance in Eq. 3.11 and divide by m_r^2 instead of m_{ab}^2. This substitution will result in a small spin zero component when the resonance is off mass-shell. This behavior occurs with the W boson; it is also expected in the resonance behavior herein.

With this substitution, we insert the spin sum into Equation 3.10 and sum over repeated indices. The result gives the Lorentz invariant matrix element for a vector particle as a function of position on the Dalitz plot:

$$\mathcal{A}_1(abc|r) = F_D F_r T_r(m_{ab}) \left(m_{ac}^2 - m_{bc}^2 + \frac{(m_D^2 - m_c^2)(m_b^2 - m_a^2)}{m_r^2} \right) \tag{3.12}$$

As a matter of completeness, we will also look at the case of a tensor (spin 2) particle. We begin with

$$\mathcal{A}_2(abc|r) = F_D(p_{D^0} + p_c)_\mu (p_{D^0} + p_c)_\nu T_r(m_{ab}) \sum_\lambda \varepsilon_\lambda^{\mu\nu*} \varepsilon_\lambda^{\alpha\beta} (p_a - p_b)_\alpha (p_a - p_b)_\beta F_r \tag{3.13}$$

The spin sum has been calculated [8] to be

$$\sum_\lambda \varepsilon_\lambda^{\mu\nu*} \varepsilon_\lambda^{\alpha\beta} = \frac{1}{2}(T^{\mu\alpha} T^{\nu\beta} + T^{\mu\beta} T^{\nu\alpha}) - \frac{1}{3} T^{\mu\nu} T^{\alpha\beta} \tag{3.14}$$

where

$$T^{\mu\nu} = -g^{\mu\nu} + \frac{p^\mu p^\nu}{m^2} \tag{3.15}$$

Inserting this expression into Eq. 3.13 and performing the sum, the final element is

$$\mathcal{A}_2(abc|r) = F_D T_r(m_{ab}) F_r \left[\left(m_{bc}^2 - m_{ac}^2 + \frac{(m_D^2 - m_c^2)(m_a^2 - m_b^2)}{m_r^2} \right)^2 \right.$$
$$\left. -\frac{1}{3}\left(m_{ab}^2 - 2m_b^2 - 2m_c^2 + \frac{(m_D^2 - m_c^2)^2}{m_r^2} \right)\left(m_{ab}^2 - 2m_a^2 - 2m_b^2 + \frac{(m_a^2 - m_b^2)^2}{m_r^2} \right) \right] \tag{3.16}$$

At this point we must state our phase conventions. Examining Eq. 3.12 we see that if we switch the labels a and b, we will generate an overall minus sign, changing the phase by 180°. To be consistent with previous results, we choose the phase convention the E687 Collaboration [39] uses.

We are now in a position to discuss the total dynamics matrix. For a D^0 Dalitz decay with a nonresonant (nr) component and n resonances, we express the total dynamics matrix as

$$\mathcal{M}(D^0 \to abc) = \mathrm{a}_{nr} e^{i\phi_{nr}} + \sum_n \mathrm{a}_n e^{i\phi_n} \mathcal{A}_{s_n} \tag{3.17}$$

where a_n and ϕ_n are the amplitude and relative phase of the n'th component respectively. The normalization is arbitrary, so is generally chosen to be

$$\int |\mathcal{M}|^2 d\mathcal{DP} = 1 \tag{3.18}$$

where $d\mathcal{DP}$ denotes an integral over the Dalitz Plot. In practice this means we are only sensitive to relative phases and amplitudes, therefore we are free to fix one phase and amplitude in Eq. 3.17. The standard prescription is to fix the amplitude and phase of the largest mode to one and zero respectively.

The choice of normalization, amplitude formulation, and phase convention are often

inconsistent between experimental results. It is therefore more common for fit fractions to be reported as well, since this allows a more meaningful comparison. The fit fraction is defined as the integral over the Dalitz plot of one resonance, divided by the integral of the coherent sum of all of the components:

$$\text{Fit Fraction}_r \equiv \frac{\int |\mathrm{a}_r e^{i\phi_r} \mathcal{A}(abc|r)|^2 d\mathcal{DP}}{\int |\Sigma_j \mathrm{a}_j e^{i\phi_j} \mathcal{A}(abc|j)|^2 d\mathcal{DP}} \tag{3.19}$$

The sum of fit fractions for all components will generally not equal one due to interference.

3.2 The Dalitz Fitter

I use a maximum likelihood Dalitz plot fitter developed by Mikhail Dubrovin [40]. Written in C++, the fitter uses both standard libraries as well as Root[1] libraries. Graphical output is also handled in Root. This software is robust; among its features, it can fit multiple simultaneous Dalitz plots, choose from several minimization methods including unbinned LogL, binned LogL and χ^2, as well as calculate fit fractions with statistical errors. It can also perform separate Efficiency and Background fitting using samples of my choosing. It uses `MINUIT`[2] to perform the multi-parameter minimization.

For a single event i, the probability distribution function at the (m^2_{ab}, m^2_{bc}) position on a Dalitz Plot can be described by

$$L_i = f_i(m^2_{ab}, m^2_{bc}; \alpha_1, \alpha_2, \ldots, \alpha_k)$$

where α_k represent the k parameters that are to be determined. For N events on the plot, the total likelihood is given by the product of L_i,

$$\mathcal{L} = \prod_{i=1}^{N} L_i = \prod_{i=1}^{N} f_i(m^2_{ab}, m^2_{bc}; \alpha_1, \alpha_2, \ldots, \alpha_k) \tag{3.20}$$

The maximum lilkelihood is the set of parameters $\alpha_1, \ldots, \alpha_k$ that maximize $\mathcal{L}$ over the Dalitz

[1] `http://root.cern.ch`

[2] `http://seal.web.cern.ch/seal/snapshot/work-packages/mathlibs/minuit/`

plot. In practice, we can maximize $\mathcal{L}$ by minimizing the negative log of the function

$$\mathcal{F} = -2\log\mathcal{L} = -2\sum_{i=1}^{N}\log L_i \tag{3.21}$$

For N events on the Dalitz plot described by $|\mathcal{M}|^2$, with efficiency $\varepsilon(m_{ab}^2, m_{bc}^2)$ and background $\mathcal{B}(m_{ab}^2, m_{bc}^2)$, the minimized fuction is [12]

$$\mathcal{F} = -2\sum_{i=1}^{N}\log\left(\frac{f\varepsilon(m_{ab}^2, m_{bc}^2)|\mathcal{M}|^2}{\mathcal{N}_{signal}} + \frac{(1-f)\mathcal{B}(m_{ab}^2, m_{bc}^2)}{\mathcal{N}_{background}}\right)_i + \chi^2_{penalty} \tag{3.22}$$

where f is the signal fraction, and $\mathcal{N}_{signal}$, $\mathcal{N}_{background}$ are

$$\mathcal{N}_{signal} = \int \varepsilon(m_{ab}^2, m_{bc}^2)|\mathcal{M}|^2 d\mathcal{D}\mathcal{P} \tag{3.23}$$

and

$$\mathcal{N}_{background} = \int \mathcal{B}(m_{ab}^2, m_{bc}^2) d\mathcal{D}\mathcal{P} \tag{3.24}$$

respectively. I will discuss the details of the two separate penalty terms in the next chapter.

The fit parameters α_k correspond to phases and amplitudes for the matrix components, signal fraction, efficiency and background coefficients, as well as coefficients of any background resonances. The coupling terms, decay radii, and particle masses are all fixed, but can be floated as needed.

3.3 Event Selection

Event selection is mostly common to both decay channels. I process over the D Skim of each relevant dataset, choosing the decay channel in question. Since I am not performing a double tag reconstruction, charge conjugation should be assumed throughout. In events with fewer than ten candidates, I count the number of candidates and select for the smallest ΔE to reduce combinatoric background. Events with ten or more candidates are rejected. As seen in Figure 3.2, roughly 75% of $K_s^0 K^+ K^-$ events contain only one candidate. In the

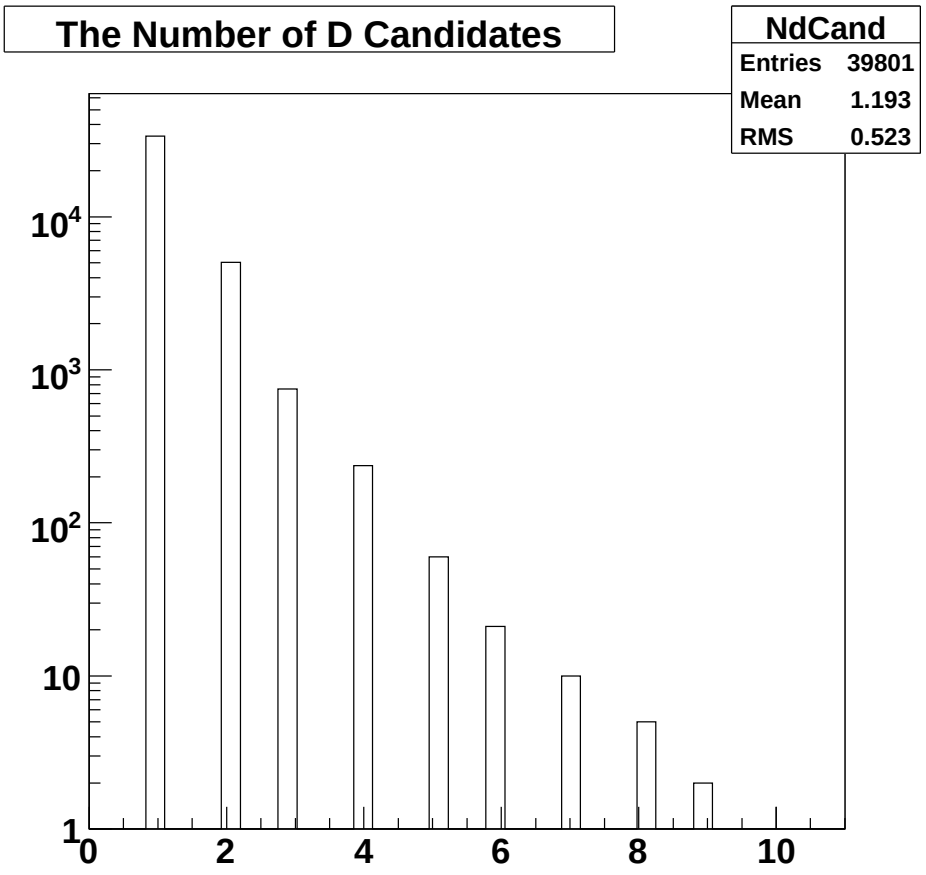

Figure 3.2: A plot of the number of $D^0 \to K^0_s K^+ K^-$ candidates per event, counted during best candidate selection.

$K^0_s \pi^0 \eta$ channel, Figure 3.3 roughly 75% of events contain either one or two candidates, most of which are one candidate events. In order to better select events on $K^0_s \pi^0 \eta$, I also cut on the probability of a good D^0 fit (Figure 3.4), where $1 - P(\chi^2, 4)$ is defined as the probability that χ^2, calculated for the overall D^0 hypothesis by the D skim, exceedes the value χ^2 by chance, and 4 is the number of degrees of freedom.

I use beam-constrained mass (m_{bc}) and ΔE as my primary selection variables, since the beam energy is accurately known and the $D\bar{D}$ pair produced from $\psi(3770)$ are created nearly at rest. Therefore m_{bc} and ΔE serve as convenient proxies for invariant mass and momentum respectively. I create a 2D histogram of these variables (Figures 3.5 and 3.6) to discern any

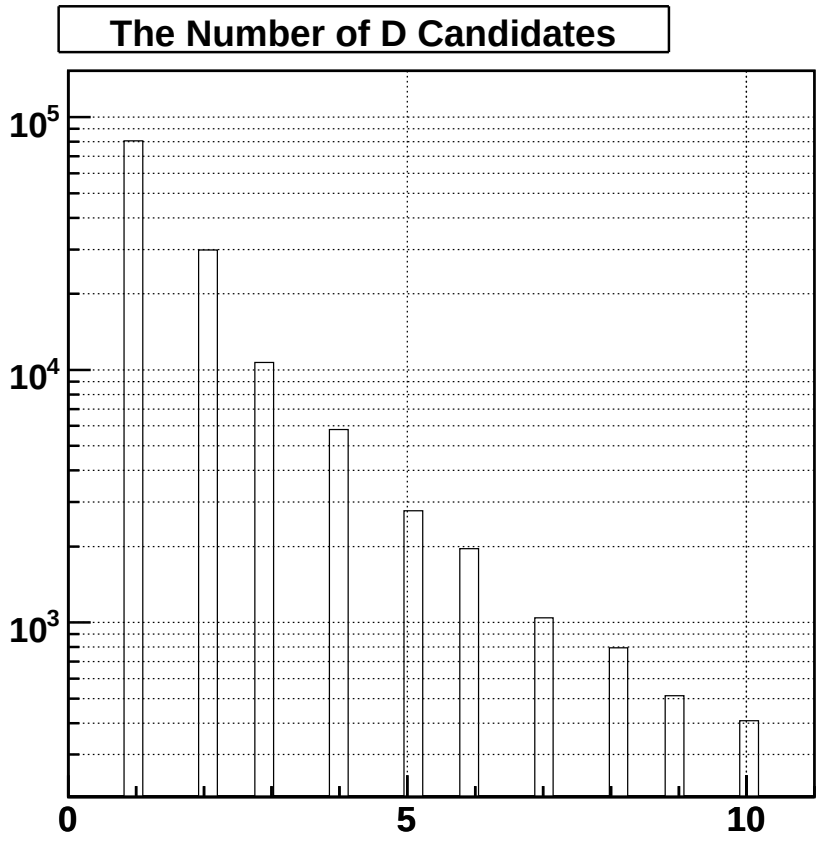

Figure 3.3: A plot of the number of $D^0 \to K^0_s \pi^0 \eta$ candidates per event, counted during best candidate selection.

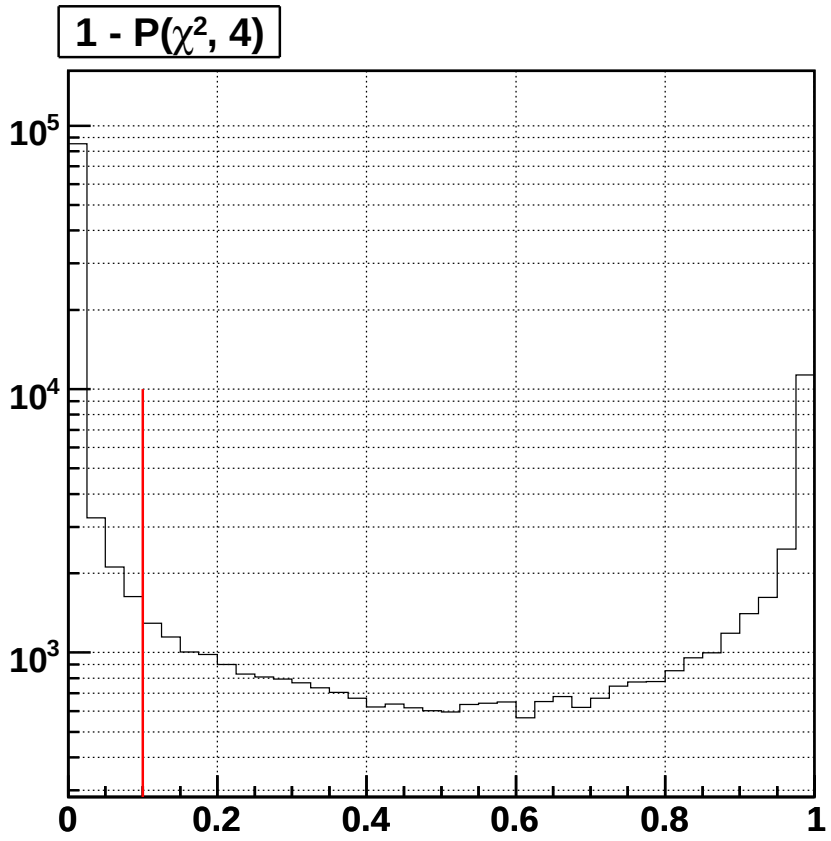

Figure 3.4: A plot of $D^0 \to K^0_s \pi^0 \eta$ Fit Probability. The red line shows the cut Fit Probability > 0.1.

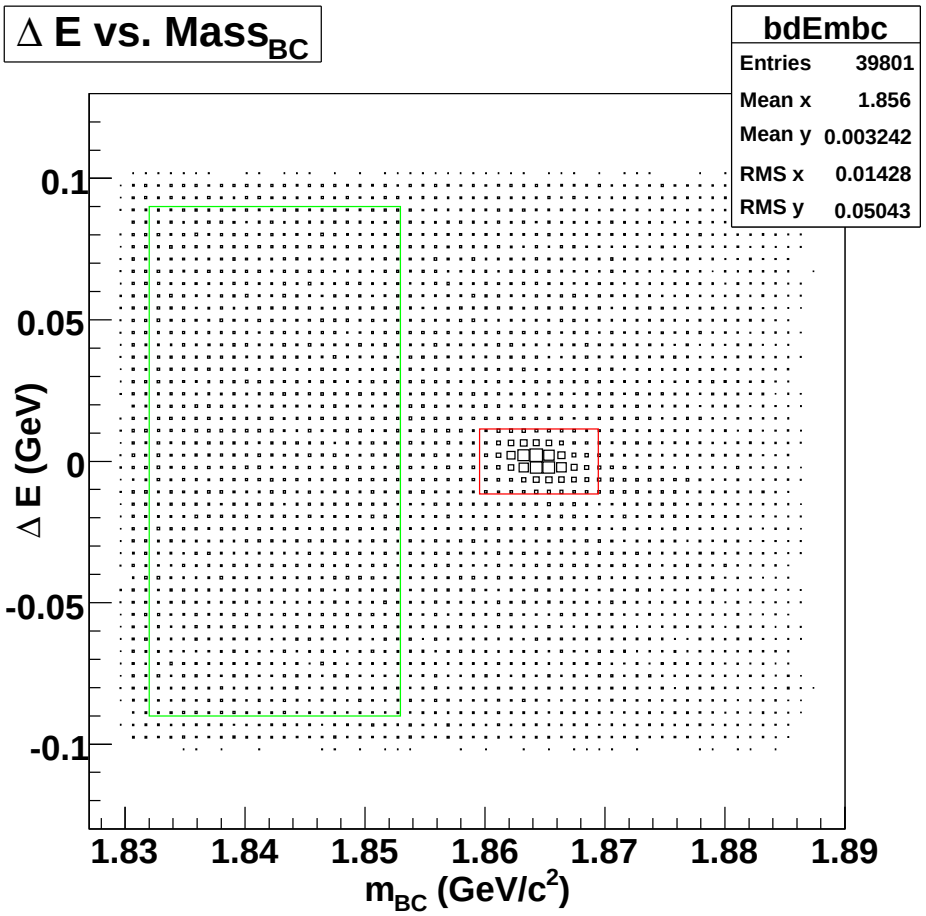

Figure 3.5: $D^0 \to K^0_s K^+ K^-$: ΔE Versus M_{bc}. Red indicates the Signal selection; Green, Background

clear signal regions. When found, I fit each variable using the root package roofit[3], which has several physics-inspired fit functions. The region containing a peak is fit to either a single or double Gaussian signal function convolved with a background function that will best describe the non-signal portion of the histogram. I choose candidates that lie within $\pm 3\sigma$ of the $K^0_s K^+ K^-$ signal mean of both m_{bc} (Figure 3.7) and ΔE (Figure 3.8) fits. For $K^0_s \pi^0 \eta$ candidates, I select within $\pm 2\sigma$ of m_{bc} (Figure 3.9) and ΔE (Figure 3.10) fits. The background samples chosen are different and will be covered in their respective sections.

[3] `http://roofit.sourceforge.net/`

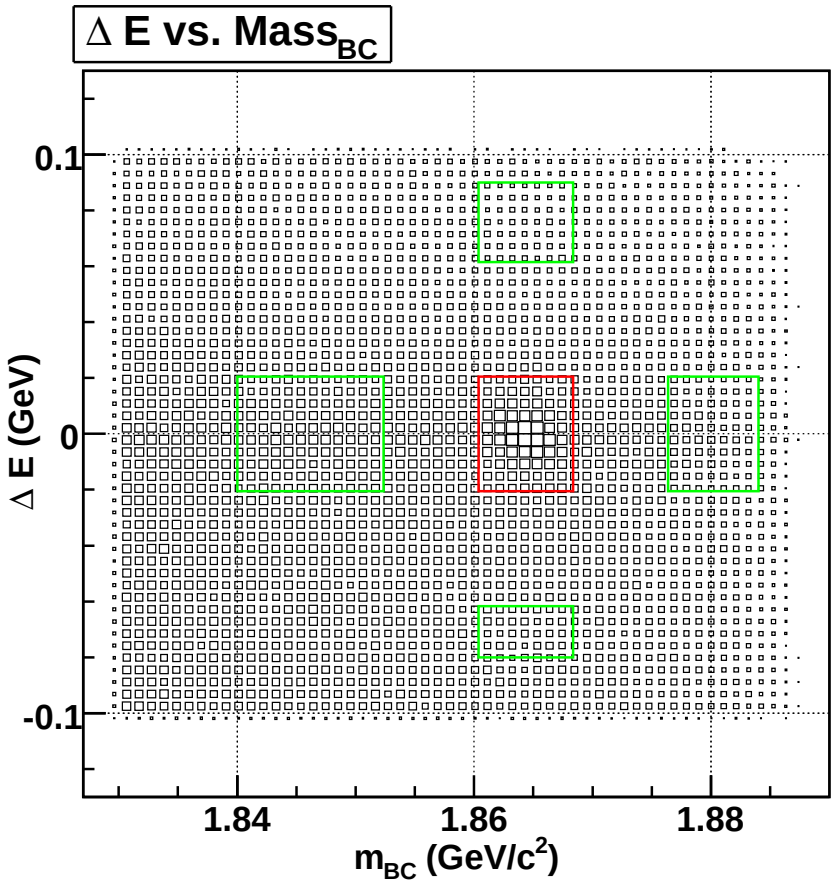

Figure 3.6: $D^0 \to K^0_s\pi^0\eta$: ΔE Versus M_{bc}. Red indicates the Signal selection; Green, Background

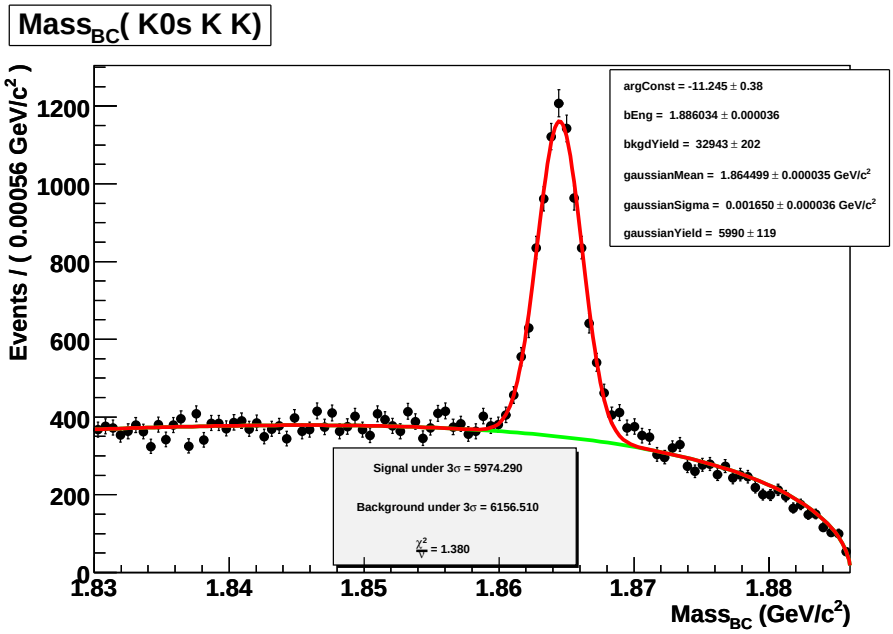

Figure 3.7: Beam–Constrained Mass Fit of $D^0 \to K^0_s K^+ K^-$ under ΔE Cut

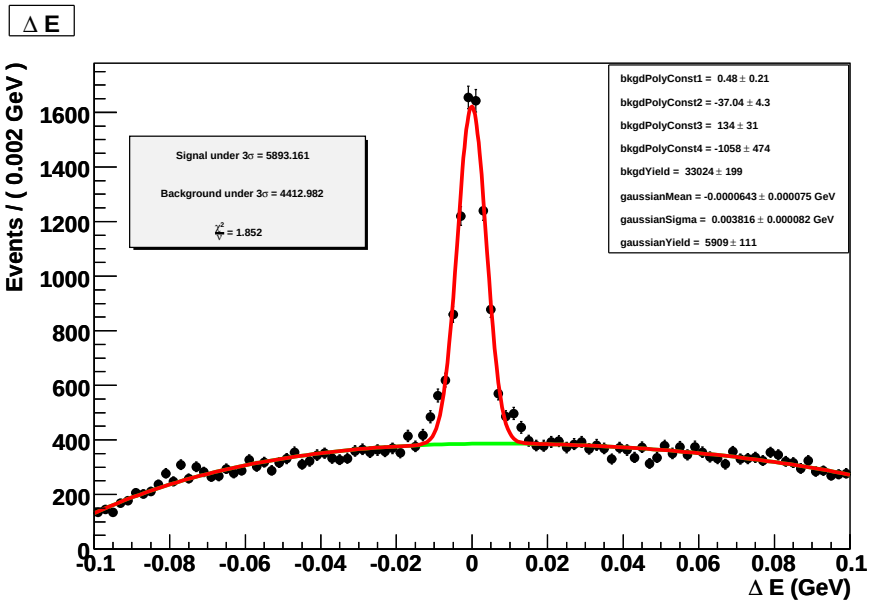

Figure 3.8: ΔE Fit of $D^0 \to K^0_s K^+ K^-$ under m_{bc} Cut

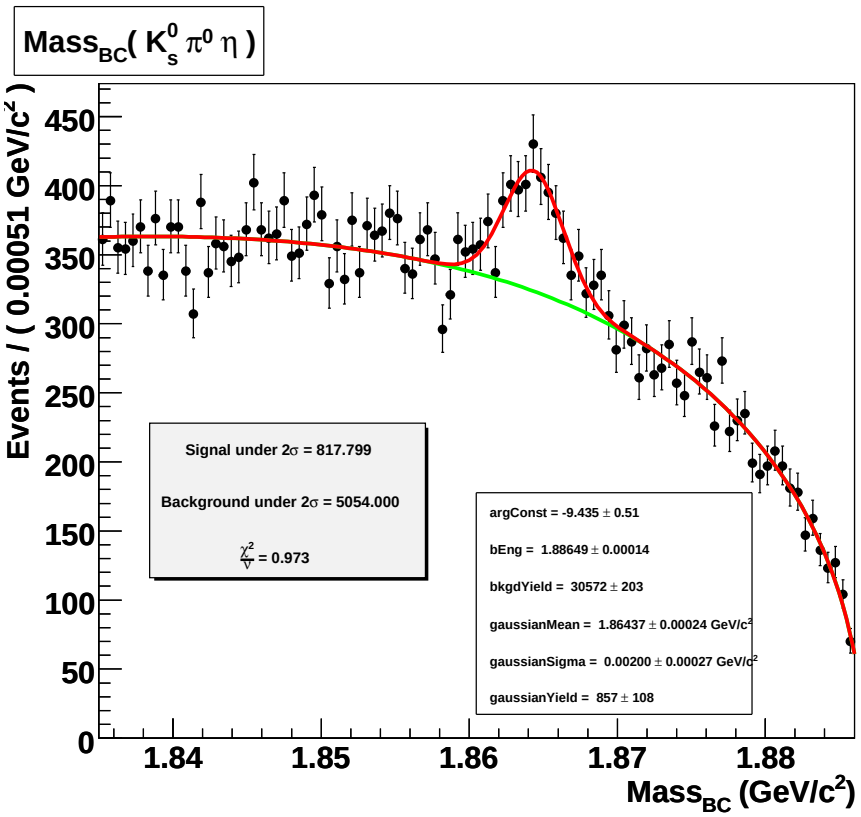

Figure 3.9: Beam–Constrained Mass Fit of $D^0 \to K^0_s\pi^0\eta$ under ΔE Cut

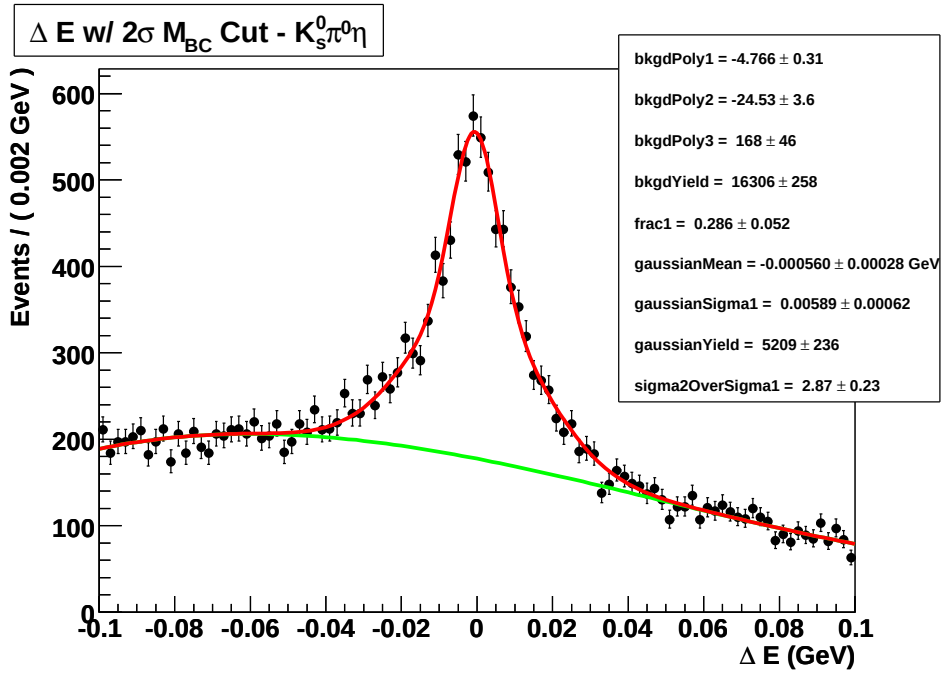

Figure 3.10: ΔE Fit of $D^0 \to K^0_s\pi^0\eta$ under m_{bc} Cut

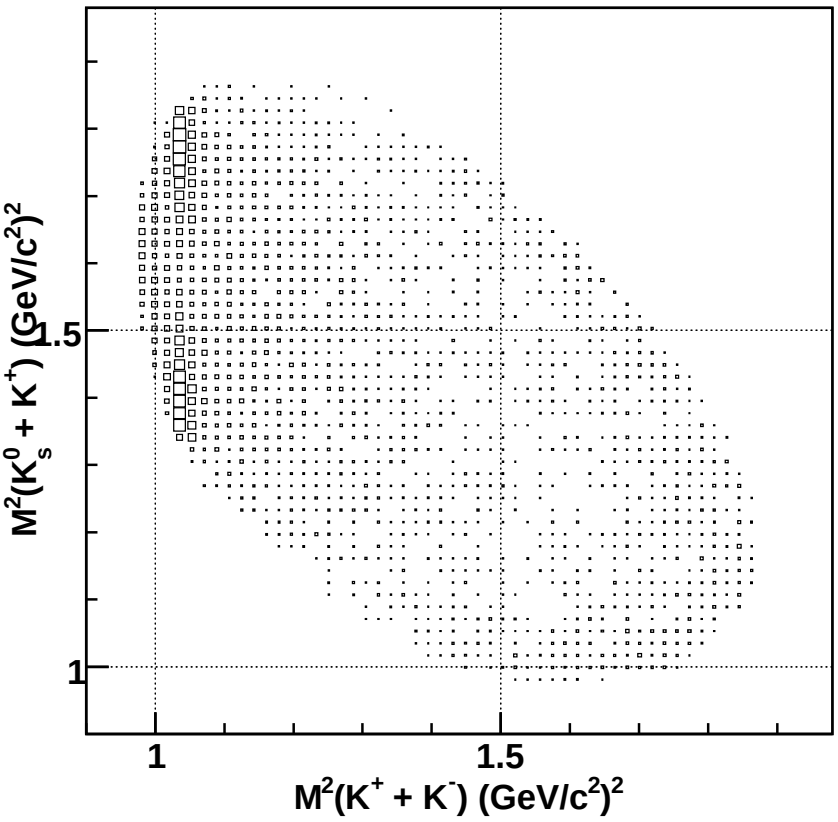

Figure 3.11: Raw (Unfitted) Dalitz plot of $D^0 \to K^0_s K^+ K^-$ in Signal region. Several events lie outside of the proper kinematic limits and will be discarded by the fitter.

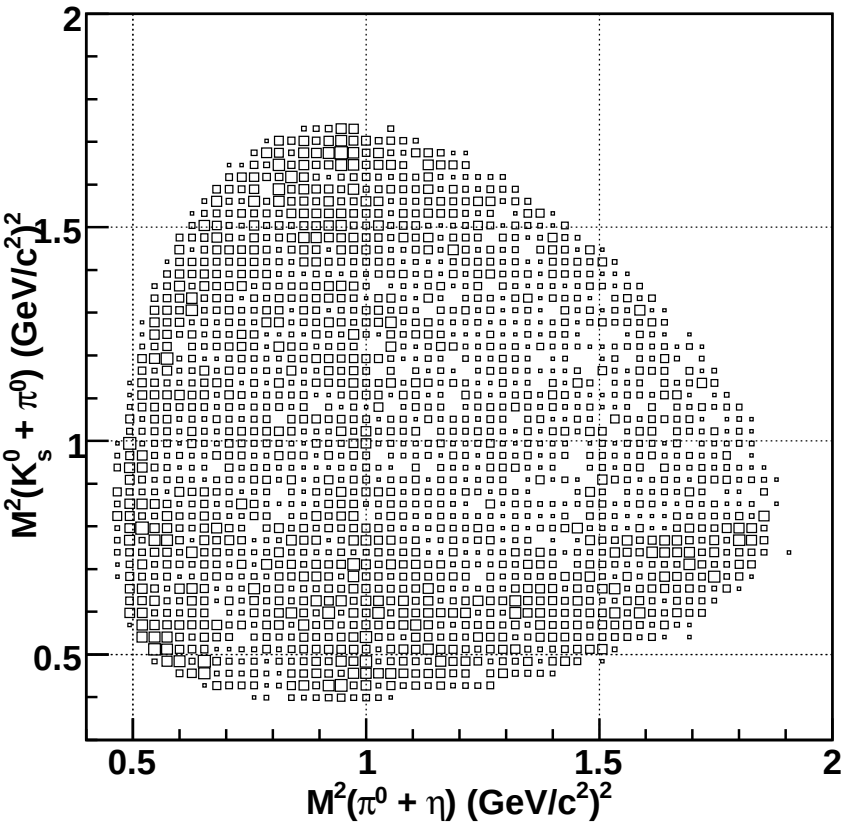

Figure 3.12: Raw (Unfitted) Dalitz plot of $D^0 \to K^0_s \pi^0 \eta$ in Signal region. Several events lie outside of the proper kinematic limits and will be discarded by the fitter.

3.4 Efficiency

Candidate particles up to and including the D can be mis–reconstructed despite our best efforts. This means our observation will not generally be uniform over the Dalitz plot. In order to characterize my ability to "see" events on the plot, I generate 50,000 signal Monte Carlo events in each channel according to the previously discussed method and fit them to the Efficiency. On the Dalitz plot, the efficiency is described as a 2D, 3$^{\text{rd}}$ degree polynomial

$$\varepsilon(x,y) = 1+E_x x+E_y y+E_{xy}xy+E_{xx}x^2+E_{yy}y^2+E_{xxy}x^2y+E_{xyy}xy^2+E_{yyy}y^3+E_{xxx}x^3 \quad (3.25)$$

where E_n are coefficients fit to a suitable Monte Carlo sample. I decay $D^0 \to K^0_s K^+ K^-$ without any intermediate resonances, and similarly $D^0 \to K^0_s \pi^0 \eta$. The resultant candidate signal MC events are filtered through the same selections as signal events, including ΔE and m_{bc} ranges set by the signal fit to variables. The efficiency Dalitz plots are shown in Fig. 3.13 and Fig. 3.14. Table 3.2 contains Efficiency coefficients for both channels.

Table 3.2: Efficiency Fit Results for $D^0 \to K^0_s K^+ K^-$ ($x = m^2(K^+ + K^-)$, $y = m^2(K^0_s + K^+)$) and $D^0 \to K^0_s \pi^0 \eta$ ($x = m^2(\pi^0 + \eta)$, $y = m^2(K^0_s + \pi^0)$).

Efficiency Coefficient	$D^0 \to K^0_s K^+ K^-$	$D^0 \to K^0_s \pi^0 \eta$
E_x	-0.1468 ± 0.1272	0.2880 ± 0.1070
E_y	-0.1530 ± 0.1182	0.5025 ± 0.1223
E_{xy}	-2.5060 ± 0.3033	-0.3697 ± 0.1819
E_{xx}	-0.7467 ± 0.2291	0.3167 ± 0.1992
E_{yy}	-2.4399 ± 0.2010	0.4350 ± 0.1560
E_{xxy}	21.5383 ± 2.3304	-1.1803 ± 0.5101
E_{xyy}	20.9594 ± 2.2701	-0.7567 ± 0.5525
E_{yyy}	2.0926 ± 1.1163	-0.4858 ± 0.4303
E_{xxx}	7.5073 ± 1.2527	-0.9533 ± 0.3618

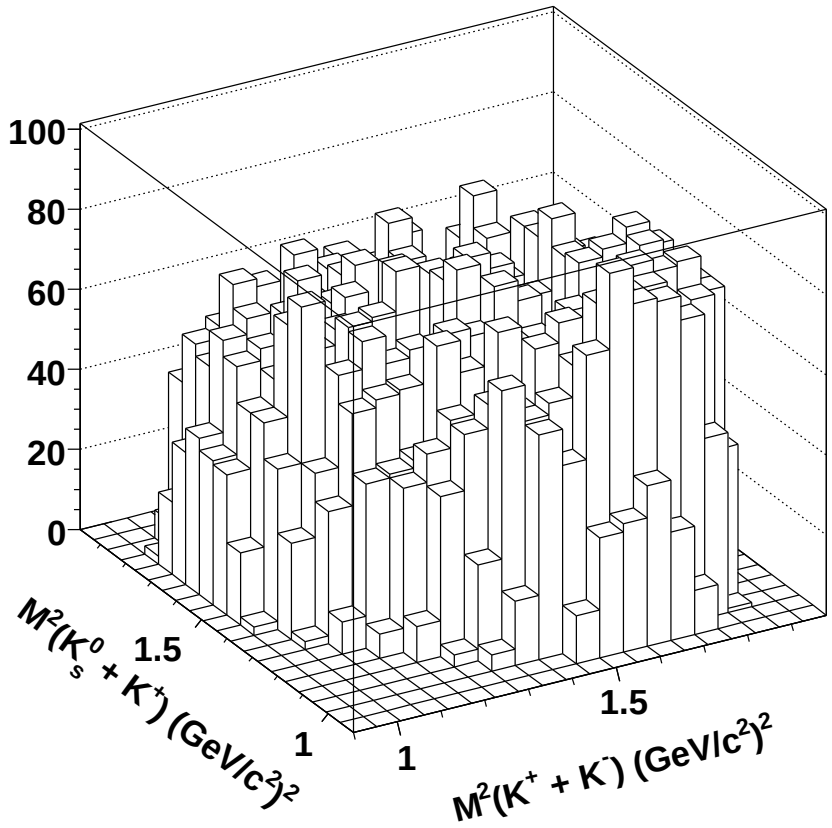

Figure 3.13: Efficiency Dalitz plot of $D^0 \to K^0_s K^+ K^-$ under Signal Selection.

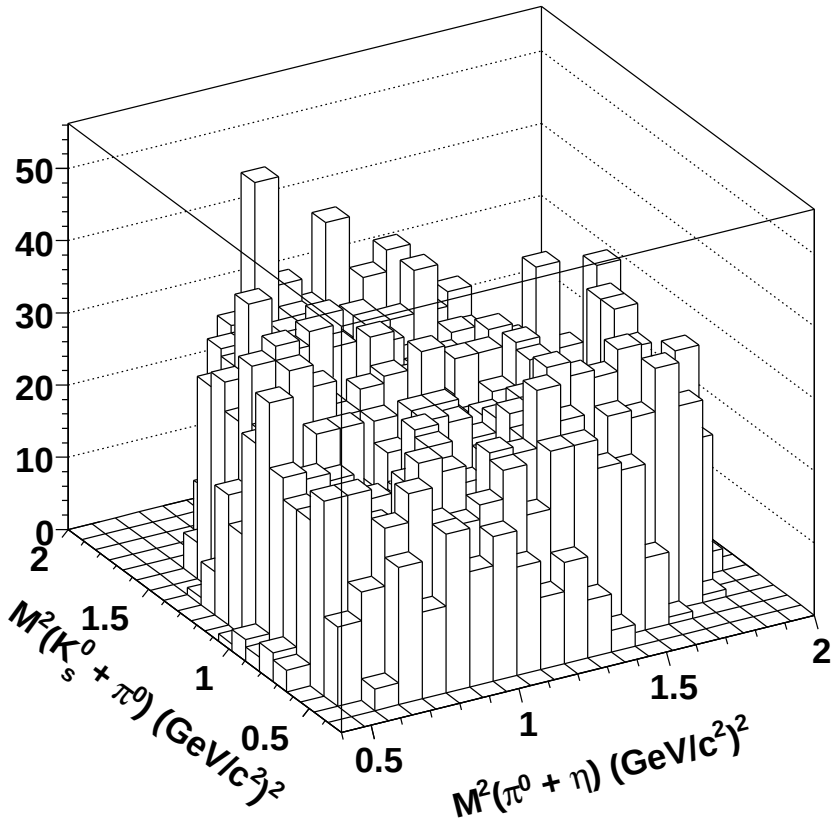

Figure 3.14: Efficiency Dalitz plot of $D^0 \to K^0_s\pi^0\eta$ under Signal Selection.

3.5 Background Selection

As with the efficiency, the basic model for the background on the Dalitz plot is also a 2D, 3$^{\rm rd}$ degree polynomial

$$B(x,y) = 1+B_x x+B_y y+B_{xy}xy+B_{xx}x^2+B_{yy}y^2+B_{xxy}x^2y+B_{xyy}xy^2+B_{yyy}y^3+B_{xxx}x^3 \quad (3.26)$$

where B_n are fit coefficients. Though the shapes of the background sideband selections seen in Figs. 3.5 and 3.6 are different, all are 7σ away from the signal mean in order to minimize signal pollution. The polynomial in Eq. 3.26 attempts to capture the shape of the background events underlying the signal region, using sideband events. Absent some structure indicative of resonances, this is all the description needed for background. If, however, we find a peak in the sidebands, we have one or more resonances present and must model them using generic Monte Carlo. Once we determine what resonances appear in background, we can add (const. $*$ |a|^2) for each to Eq. 3.26.

3.5.1 $D^0 \to K^0_S\pi^0\eta$

Examining Fig. 3.15, background events seem to be piling up in the low side of $m^2(\pi^0+\eta)$. Looking at the projections in Figs. 3.16, 3.17, and 3.18, we fail to find a clear signal. The resultant background fit coefficients are shown in Table 3.3.

3.5.2 $D^0 \to K^0_S K^+K^-$

The background Dalitz plot in Fig. 3.19 shows a much more prominent peak. A background resonance is obvious in the $K^+ + K^-$ projection as seen in Fig. 3.20. Using the generic Monte Carlo that corresponds to datasets 44 and 45, I examine the $K^+ + K^-$ projection and determine the candidate parents, Fig 3.21. Below 1.2GeV^2 in $K^+ + K^-$, $\phi(1020)$ is the largest charged K parent that will appear in the given projection. The location of the background peak in both signal and generic MC conforms to this.

Besides $\phi(1020)$, we also attempt the charged and uncharged versions of $a_0(1450)$ due to a numbering bug in Monte Carlo that labels $a_0(980)$ with the numerical label for $a_0(1450)$.

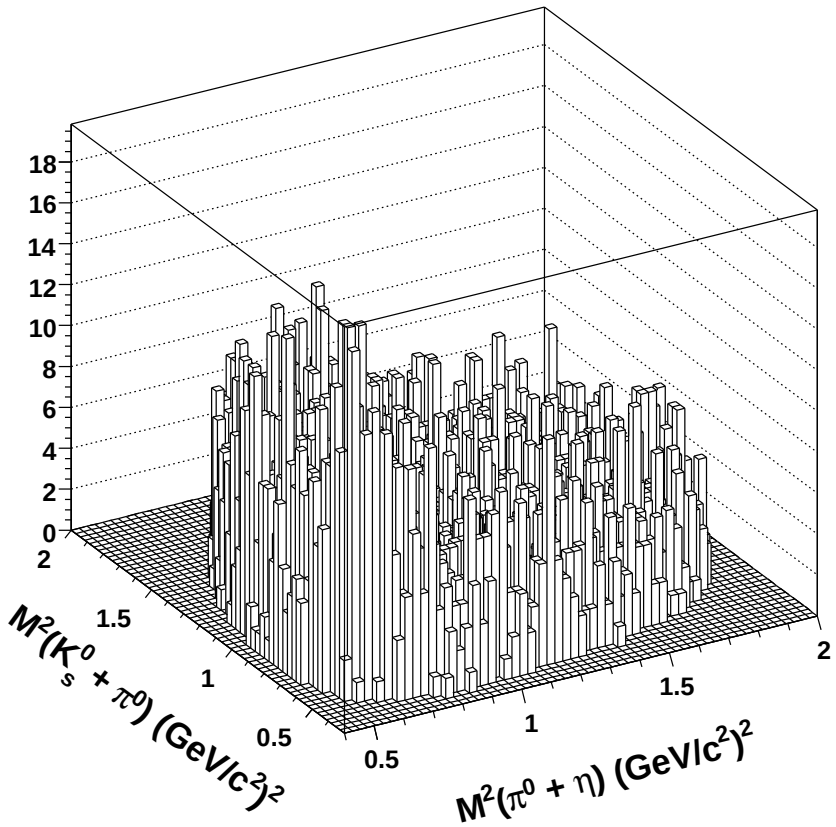

Figure 3.15: Dalitz plot of $D^0 \to K^0_s\pi^0\eta$ in Background region.

Table 3.3: Background Fit Results for $D^0 \to K^0_s\pi^0\eta$ ($x = m^2(\pi^0 + \eta)$, $y = m^2(K^0_s + \pi^0)$).

Background Coefficient	Value ± Statistical Error
B_x	-0.3362 ± 0.1045
B_y	-0.0446 ± 0.1253
B_{xy}	1.1340 ± 0.2333
B_{xx}	3.8821 ± 0.3033
B_{yy}	2.5816 ± 0.2114
B_{xxy}	-0.9074 ± 0.5779
B_{xyy}	-3.0517 ± 0.6321
B_{yyy}	0.0039 ± 0.4537
B_{xxx}	-3.5671 ± 0.4199

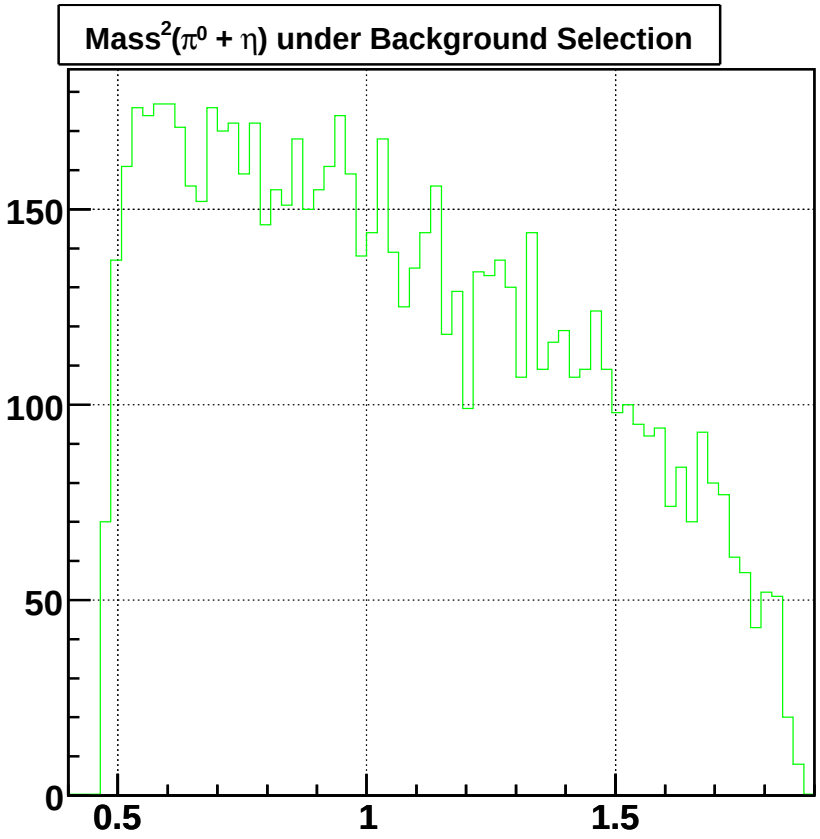

Figure 3.16: $\pi^0\eta$ Projection of $D^0 \to K^0_s\pi^0\eta$ in Background region.

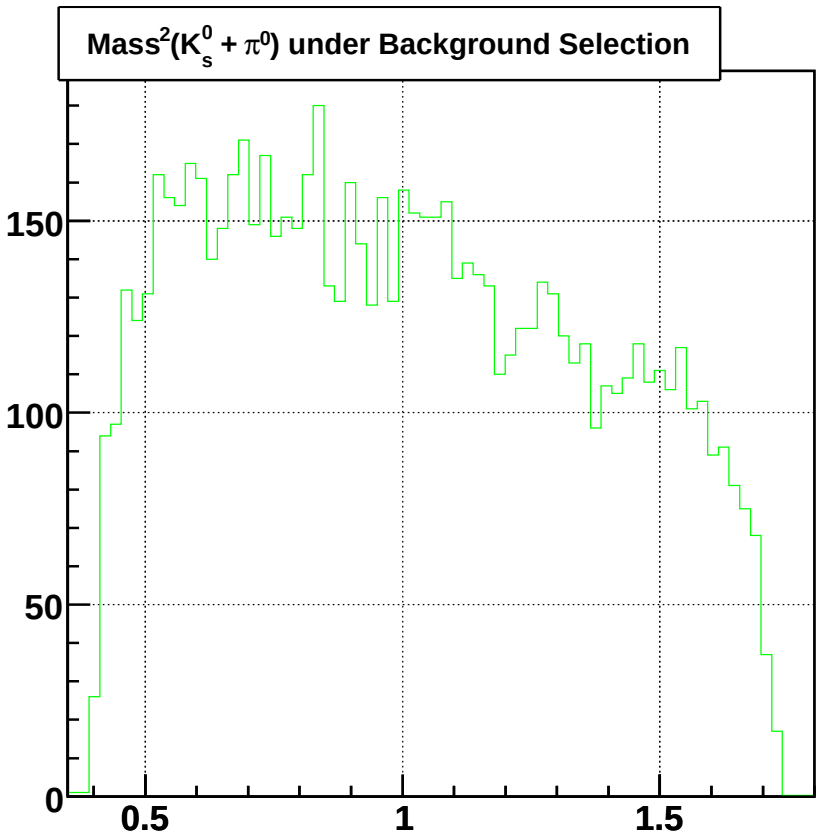

Figure 3.17: $K^0_s\pi^0$ Projection of $D^0 \to K^0_s\pi^0\eta$ in Background region.

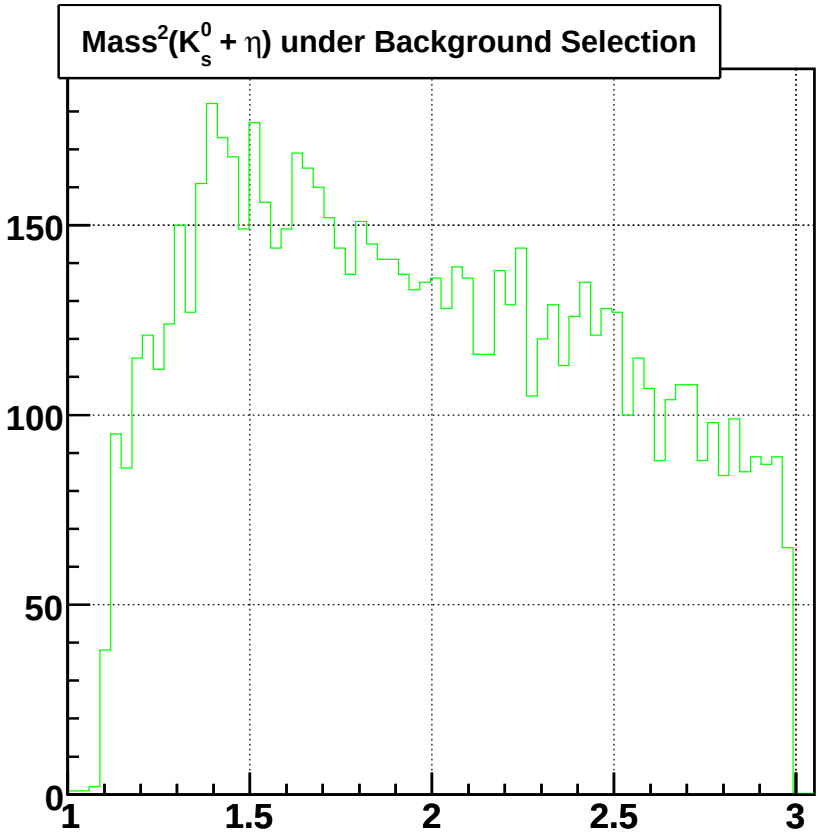

Figure 3.18: $K_s^0\eta$ Projection of $D^0 \to K_s^0\pi^0\eta$ in Background region.

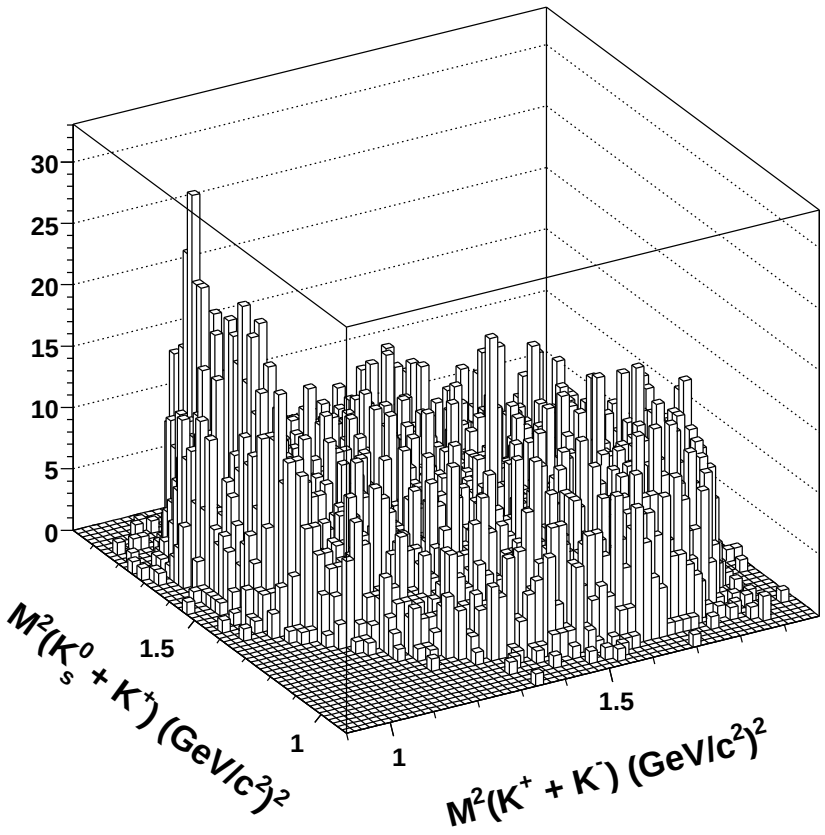

Figure 3.19: Dalitz plot of $D^0 \to K^0_s K^+ K^-$ in Background region.

Despite this, we find a significant background contribution from $a_0(1450)^0$. Fits containing $a_0(1450)^{\pm}$ failed to converge and thus these background resonances are omitted. Both $\phi(1020)$ and $a_0(1450)^0$ are modeled as Breit-Wigners. The final values are shown in Table 3.4.

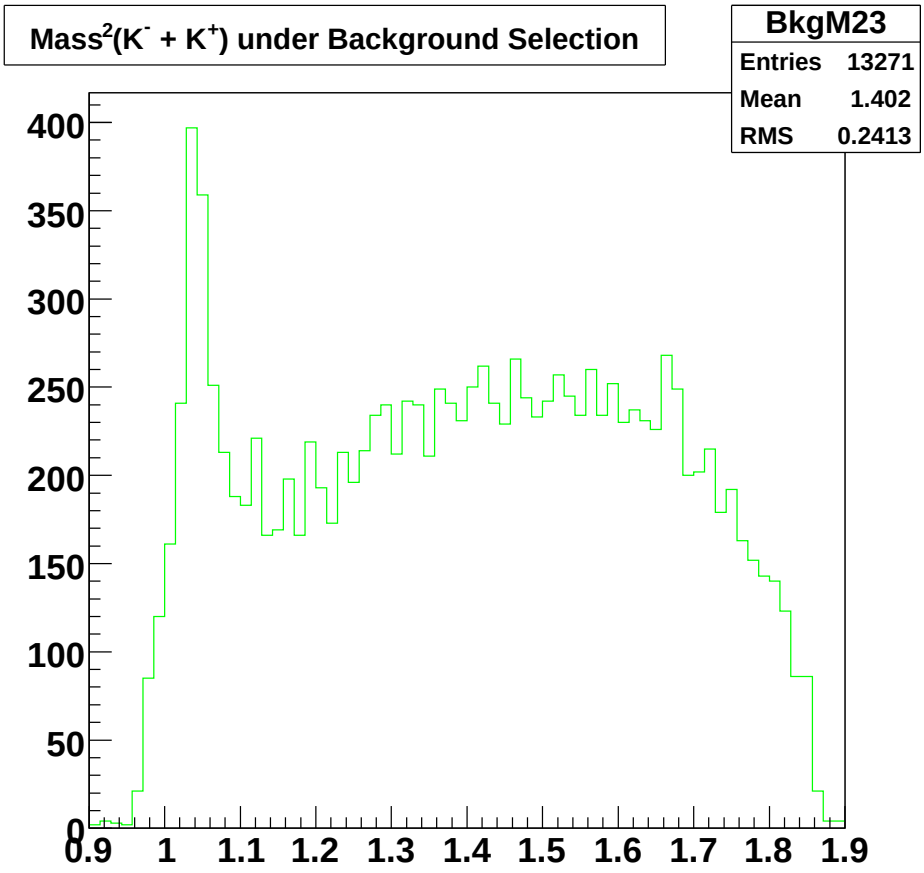

Figure 3.20: K^+K^- Projection of $D^0 \to K^0_s K^+ K^-$ in Background region.

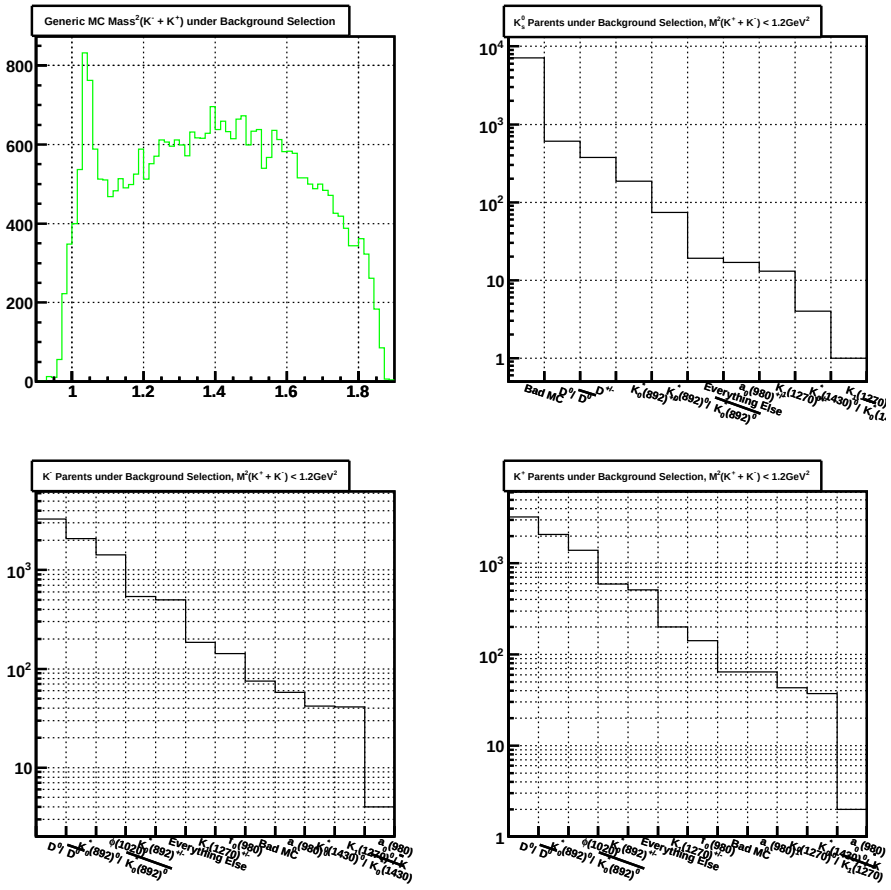

Figure 3.21: Generic Monte Carlo Figures of $D^0 \to K^0_s K^+ K^-$ in Background region. "Bad MC" are reconstructed events that do not correspond to generated MC particles.

Table 3.4: Background Fit Results for $D^0 \to K^0_s K^+ K^-$ ($x = m^2(K^+ + K^-)$, $y = m^2(K^0_s + K^+)$).

Background Coefficient	Value ± Statistical Error
$\phi(1020)$	0.0133 ± 0.0029
$a_0(1450)^0$	195.5119 ± 38.3029
B_x	-587.7579 ± 125.8467
B_y	-0.3509 ± 33.3037
B_{xy}	-803.8348 ± 168.3564
B_{xx}	-402.7109 ± 106.0521
B_{yy}	-651.6636 ± 130.6239
B_{xxy}	6409.6281 ± 1573.2437
B_{xyy}	5046.2398 ± 1311.2251
B_{yyy}	-5.8627 ± 314.1654
B_{xxx}	113.0786 ± 382.2512

CHAPTER 4: RESULTS

4.1 $D^0 \to K^0_s\pi^0\eta$ Initial Dalitz Analysis

With the efficiency and background in place, I perform the Signal fit of $K^0_s\pi^0\eta$. I rely on the previous results [14] to guide the choice of resonances that appear in the plot. We include the following resonances in our model: $K^0_s a_0(980)$, $K^*(892)\eta$, $\kappa\eta$, $K^*(1430)^0\eta$, and $K^*(1430)^0\pi^0$. All but the $a_0(980)$ resonance are modeled as standard Breit-Wigners; the $a_0(980)$ is modeled as a Flatté. We also attempt a non-resonant component, which we find to be consistent with zero.

This fit, as seen from the X ($\pi^0\eta$) projection in Fig. 4.1 appears complete. However, an unmodeled peak at 0.6GeV^2 in the Y ($K^0_s\pi^0$) projection, shown in Fig. 4.2, suggests an additional resonance is needed. After several attempts, we are unable to find a suitable resonance that is of the appropriate mass and final state. Following a suggestion from the members of the CLEO Collaboration, we instead explore the possibility of a decay involving a $\pi^0\pi+\pi-$. The $\omega(782)$ is best candidate for this peak, having a large branching fraction to $\pi^0\pi+\pi-$, the correct mass for this peak, with the $\pi^+\pi^-$ masquerading as a K^0_s. As I discuss in the Appendix, we do in fact observe the decay $D^0 \to \omega\eta$ in CLEO-c data.

4.2 Improved $D^0 \to K^0_s\pi^0\eta$ Background

The $\omega(782)$ peak doesn't appear in our background samples, thus I attempt a simultaneous signal and background fit. I model this misidentified $\omega(782)\eta$ contribution as a Guassian contribution to the background with a size determined relative to the background shape described above. That is, I fix the shape of the background contribution in $\omega(782)\eta$ to the expected background from our simulation described above plus a single Guassian, with amplitude 8.5×10^{-5} times the overall normalization of the background. I arrive at this value after various starting values, choice of floating parameters, and parameter limits fail to properly fit the $\omega(782)\eta$ peak. From the closest floating Gaussian result, I fix the peak at several values until the background peak comports with signal statistics.

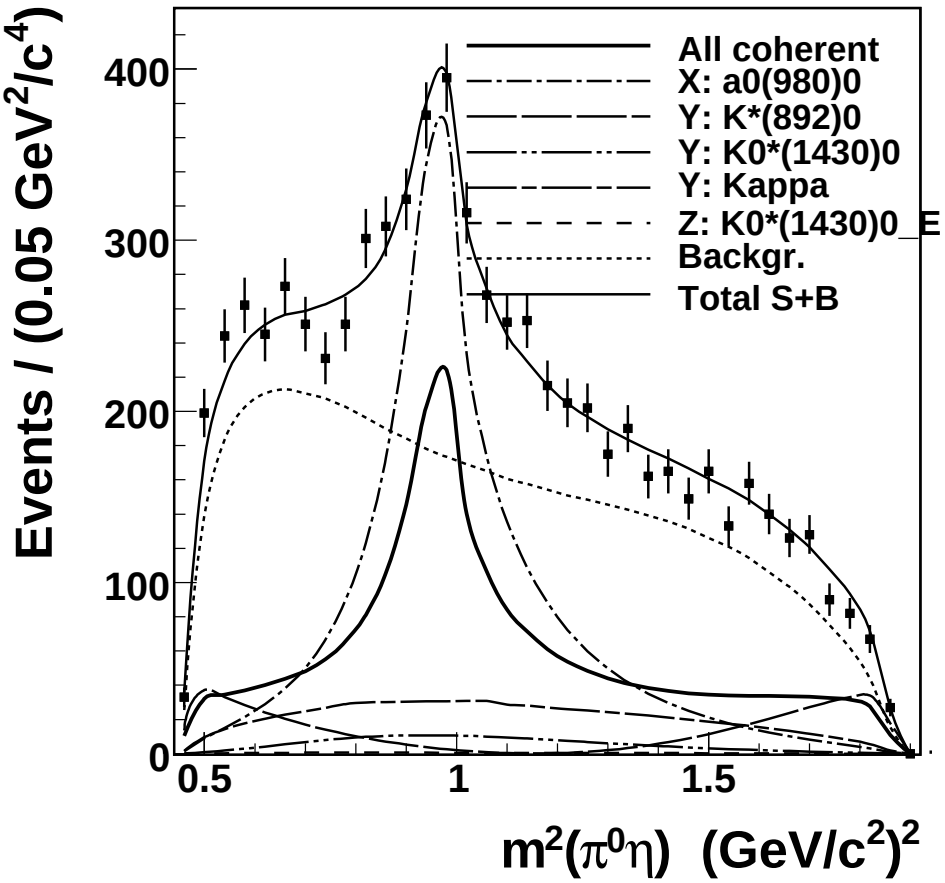

Figure 4.1: Detailed X-projection of $D^0 \to K^0_s \pi^0 \eta$ Dalitz Plot.

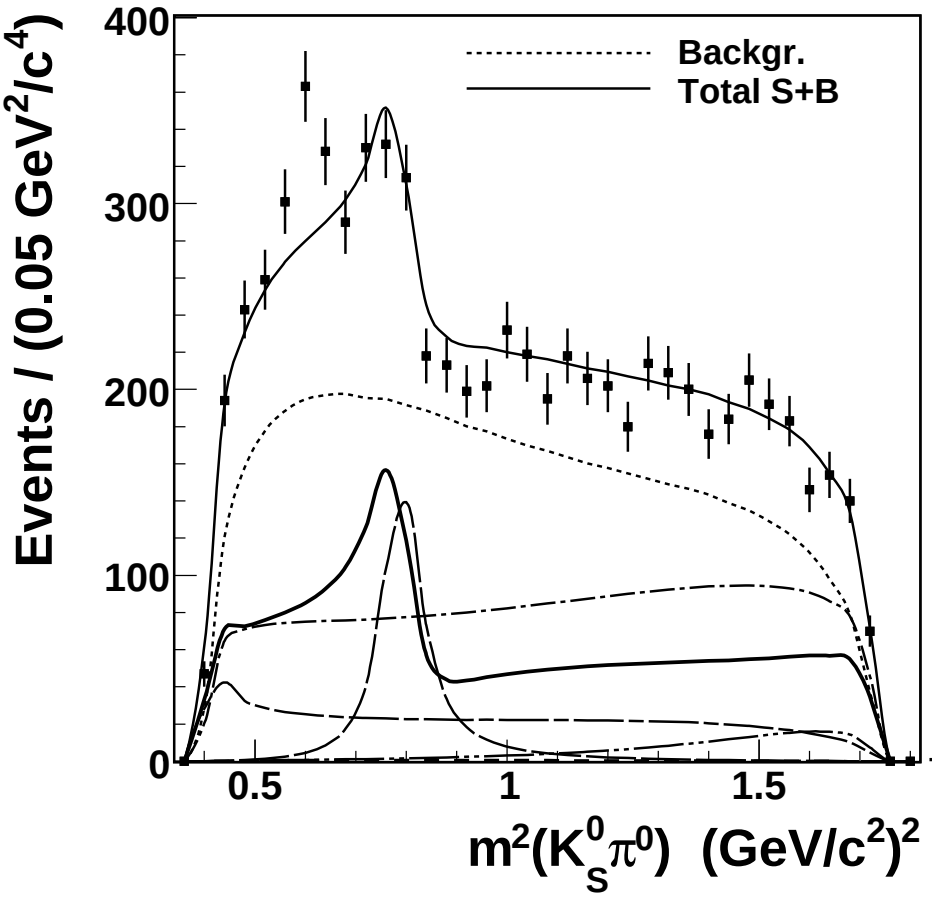

Figure 4.2: Detailed Y-projection of $D^0 \to K^0_s\pi^0\eta$ Dalitz Plot. Note the anomalous peak at 0.6GeV^2.

4.3 $D^0 \to K^0_s\pi^0\eta$ Dalitz Analysis

The complete Daltiz fit of $D^0 \to K^0_s\pi^0\eta$, including the $\omega(782)$ background, is shown in Fig. 4.3. For more detail of the fit components, see Fig. 4.4. Table 4.1 summarizes the Signal parameters. The previous CLEO result for this mode fixed the $K^0_s a_0(980)$ contribution; I instead fix $\kappa\eta$ to avoid an over–determined system when combining this $a_0(980)$ with the $a_0(980)$ found on $K^0_s K^+K^-$. As we see in Fig. 4.5, we again have a good fit in the X projection. As seen better in Fig. 4.6, we now have a reasonable grasp of the peak structure in the Y projection.

Table 4.1: Dalitz Fit Results for $D^0 \to K^0_s\pi^0\eta$. Errors are statistical.

Parameter	Amplitude	Phase	Fit Fraction
$\kappa\eta$	1	0	0.323 ± 0.044
$K^0_s a_0(980)$	1.14 ± 0.13	-103.7 ± 8.4	1.255 ± 0.023
$K^*_0(1430)\pi^0$	0.132 ± 0.070	111 ± 32	0.0066 ± 0.0050
$K^*(892)\eta$	0.231 ± 0.030	312.6 ± 9.3	0.231 ± 0.054
$K^*_0(1430)\eta$	1.12 ± 0.36	-156 ± 18	0.059 ± 0.018
Signal Fraction (f)	0.299 ± 0.020		

4.4 $D^0 \to K^0_s K^+K^-$ Dalitz Analysis

Along similar lines, I perform a Dalitz fit on the $D^0 \to K^0_s K^+K^-$ channel. We model the decay using the folowing channels: $K^0_s a_0(980)$, $K^0_s\phi(1020)$, $K^0_s f_0(1370)$, $a_0(980) \pm K\mp$, and we test a non-resonant $K^0_s K^+K^-$. The decay channel $K^0_s f_0(980)$ should appear on this plot, but including it keeps the fit from converging, thus we exclude it. The previous BABAR work[15] in this channel include all of the resonances contained herein, but does not include a non-resonant component. Additionally, we fix the $\phi(1020)$ on the Dalitz plot to avoid an over-determined system in the combined fit.

While Figs. 4.8 and 4.9 are good convergent fits containing a non-resonant contribution, we also recieive a convergent fit without the non-resonance. Looking at Table 4.2, we see that the fit wihout a non-resonant component broadly agrees with BABAR. When we compare

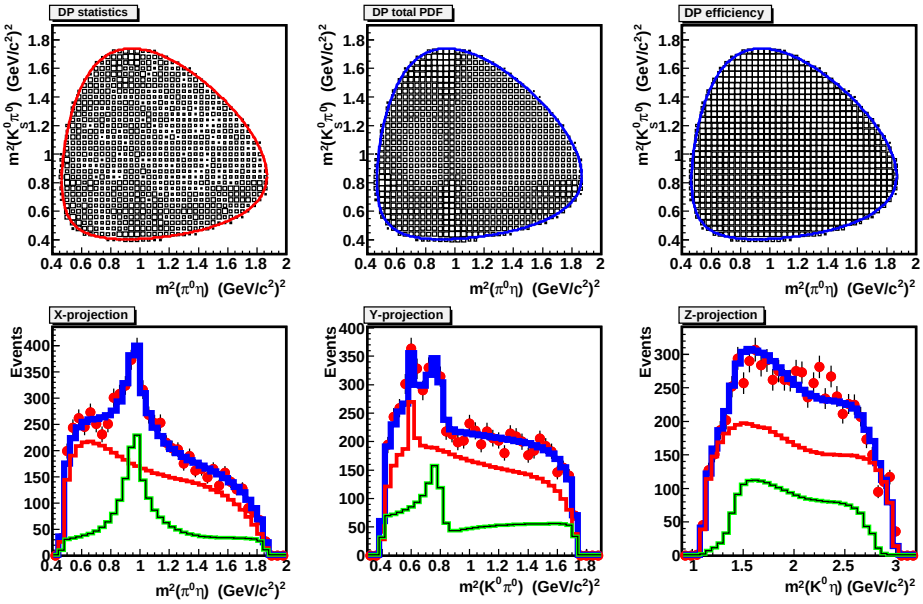

Figure 4.3: The main $D^0 \to K^0_s\pi^0\eta$ Dalitz Plots. Top row from left: Plot statistics, Total PDF, Efficiency. Bottom Row from left: X, Y, and Z Projections. Total, signal, and background are represented by blue, green, and red lines respectively.

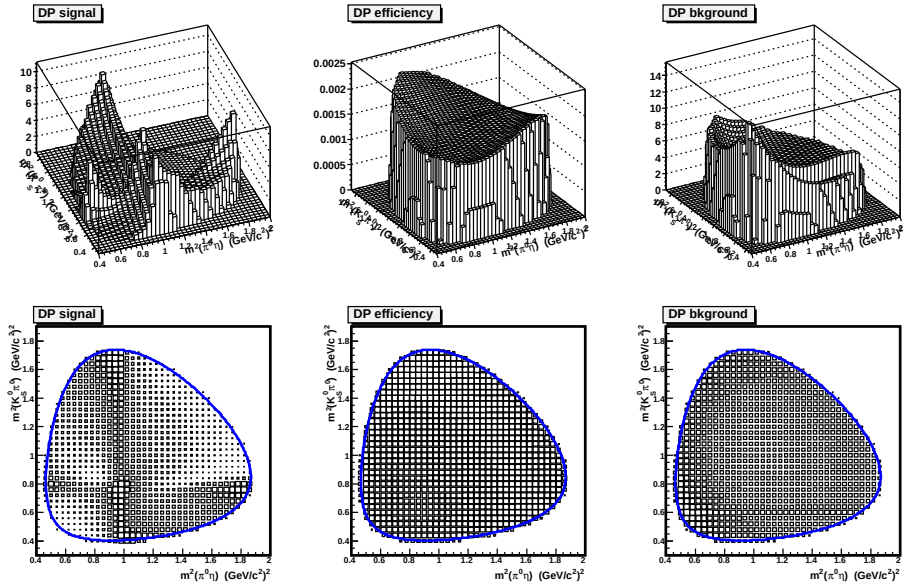

Figure 4.4: Detailed $D^0 \to K^0_s\pi^0\eta$ Dalitz Plot PDF Components. Top Row: 3D View. Bottom Row: 2D View. From left: Signal, Efficiency, Background.

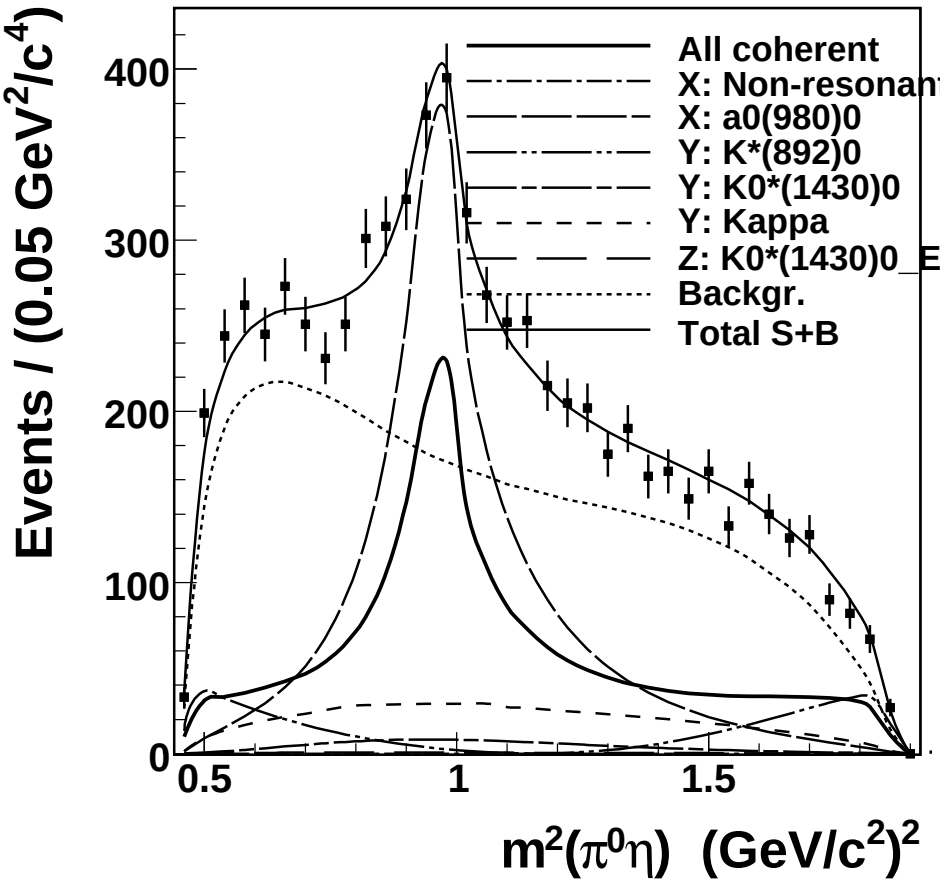

Figure 4.5: Detailed X-projection of $D^0 \to K^0_s \pi^0 \eta$ Dalitz Plot.

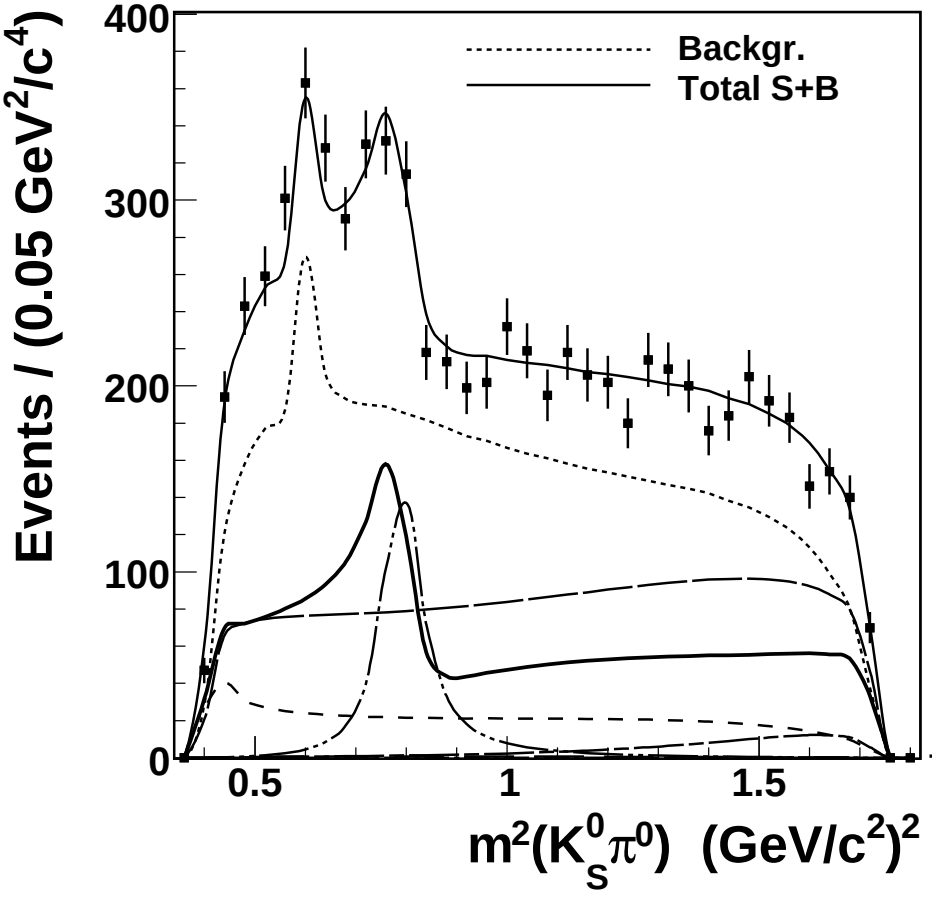

Figure 4.6: Detailed Y-projection of $D^0 \to K_s^0\pi^0\eta$ Dalitz Plot.

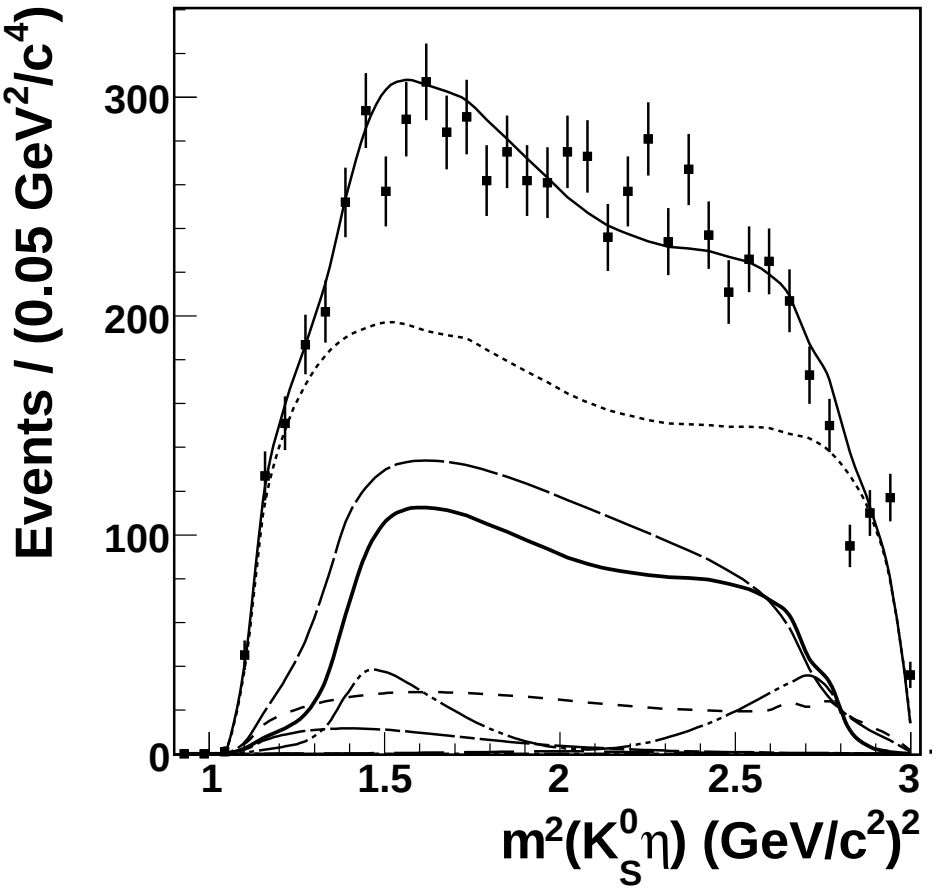

Figure 4.7: Detailed Z-projection of $D^0 \to K^0_s \pi^0 \eta$ Dalitz Plot.

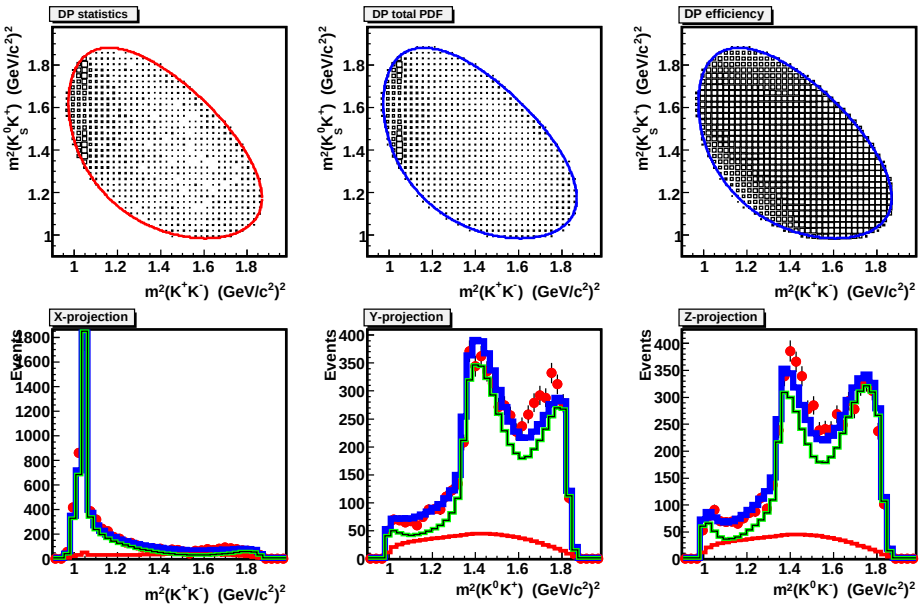

Figure 4.8: The main $D^0 \to K^0_s K^+ K^-$ Dalitz Plots. Top row from left: Plot statistics, Total PDF, Efficiency. Bottom Row from left: X, Y, and Z Projections. Total, signal, and background are represented by blue, green, and red lines respectively. *(error calculated manually)

the fit with and without the non-resonance, as seen in Figs. 4.10 through 4.12, we find the non-resonant model becomes the dominant contribution, interfering with the resonsnaces and contradicting the good result from BABAR. The resultant values are shown in Table 4.3. We do not believe the fit containing the non-resonance it real, thus we use the fit without it.

Table 4.2: Dalitz Fit Results for $D^0 \to K^0_s K^+ K^-$. Errors are statistical.

Parameter	Amplitude	Phase	Fit Fraction
$K^0_s a_0(980)^0$	4.97 ± 0.20	280	1.176 ± 0.039
$K^0_s \phi(1020)$	1	0	0.556 ± 0.024
$a_0(980)^+ K^-$	1.78 ± 0.17	72.2 ± 5.4	0.183 ± 0.019
$a_0(980)^- K^+$	1.39 ± 0.15	280.1 ± 9.8	0.112 ± 0.026
$K^0_s f_0(1370)$	4.40 ± 0.36	201.3 ± 6.2	0.442 ± 0.037

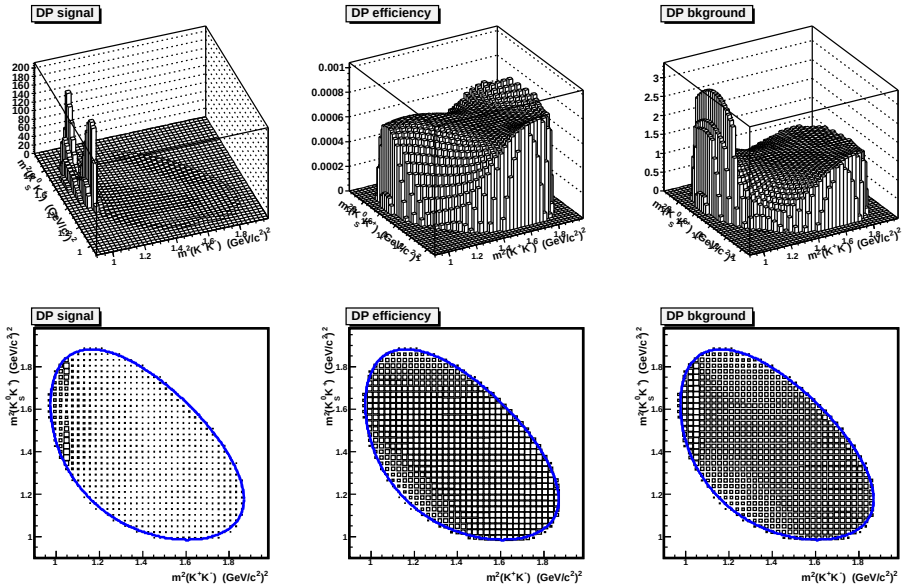

Figure 4.9: Detailed $D^0 \to K^0_s K^+ K^-$ Dalitz Plot PDF Components. Top Row: 3D View. Bottom Row: 2D View. From left: Signal, Efficiency, Background.

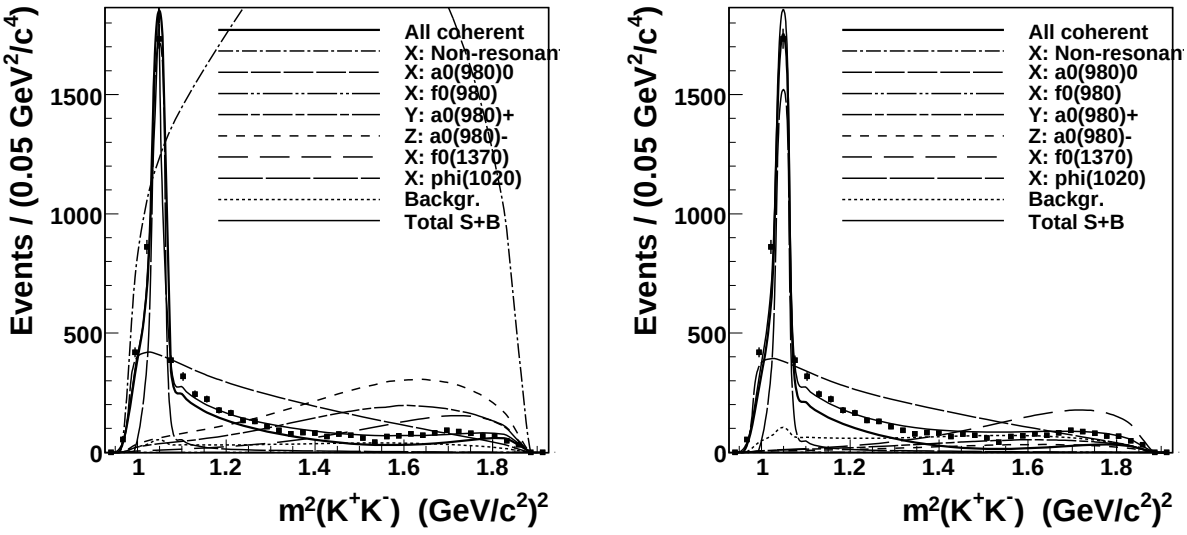

(a) (b)

Figure 4.10: Detailed X-projection of $D^0 \to K^0_s K^+ K^-$ Dalitz Plot. (a) X-projection with and (b) without the non-resonant model.

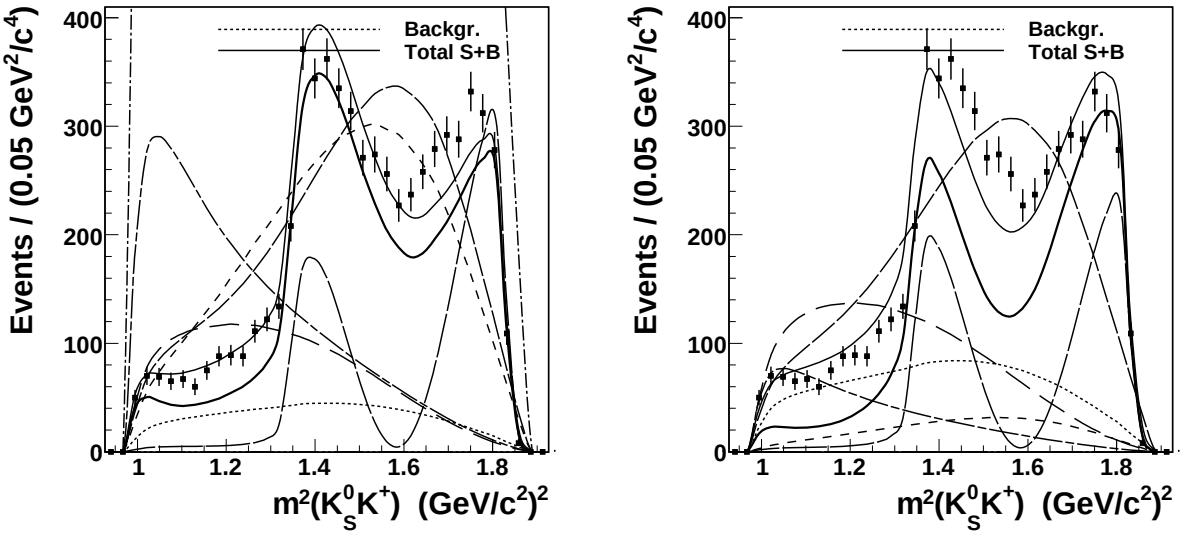

(a) (b)

Figure 4.11: Detailed Y-projection of $D^0 \to K^0_s K^+ K^-$ Dalitz Plot. (a) X-projection with and (b) without the non-resonant model.

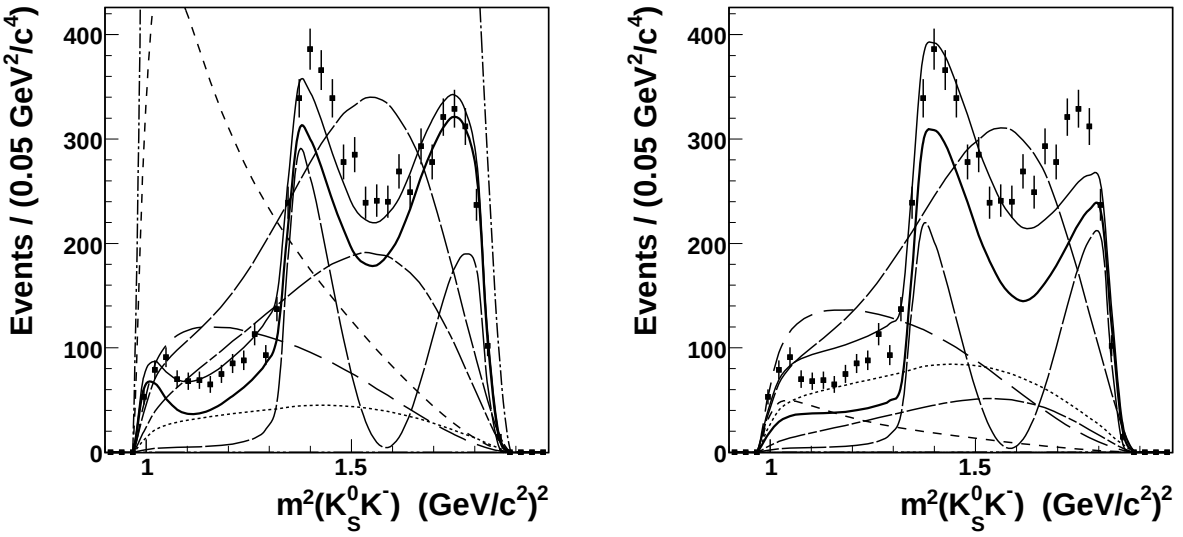

(a) (b)

Figure 4.12: Detailed Z-projection of $D^0 \to K^0_s K^+ K^-$ Dalitz Plot. (a) X-projection with and (b) without the non-resonant model.

Table 4.3: Dalitz Fit Results for $D^0 \to K^0_s K^+ K^-$ with the Non-resonant Contribution. Errors are statistical.

Parameter	Amplitude	Phase	Fit Fraction
$K^0_s a_0(980)^0$	4.78 ± 0.24	247	1.031 ± 0.020
$K^0_s K^+ K^-$	27.02 ± 0.92	230.0 ± 2.5	8.32 ± 0.11*
$K^0_s \phi(1020)$	1	0	0.526 ± 0.034
$a_0(980)^+ K^-$	3.18 ± 0.18	304.4 ± 4.0	0.555 ± 0.045
$a_0(980)^- K^+$	3.93 ± 0.19	285.0 ± 2.8	0.85 ± 0.14
$K^0_s f_0(1370)$	3.79 ± 0.30	339.6 ± 5.7	0.310 ± 0.030

4.5 Techniques of Joint Dalitz Analysis of $D^0 \to K^0_s \pi^0 \eta$ and $D^0 \to K^0_s K^+ K^-$

Equations 1.8 and 1.9 are two methods that I suggest to combine the information from one Dalitz plot analysis to constrain the results in another Dalitz analysis, specifically when there is evidence of strong interference. Equation 1.8 assumes that the amplitudes to a common resonance are the same in the two Dalitz plots and thus I call a methodology to implement Equation 1.8 the Amplitude Penalty Dalitz Analysis. Equation 1.9 assumes that the fit fraction divided by decay mode branching fraction to a common resonance is the same in the two Dalitz plots and I call this methodology the Fit Fraction Penalty Dalitz Analysis. In order to create a penalty term, we form a psuedo-χ^2

$$\chi^2 = \left(\frac{P_i - P_j}{\sqrt{\sigma_i^2 + \sigma_j^2}} \right)^2 \tag{4.1}$$

where $P_{i/j}$ are the fit fraction or amplitude ratios in Eqns. 1.8 and 1.9. Our σ values are relative uncertainties of the input branching fractions. We use the PDG average branching fraction for $\mathcal{BF}(a_0(980) \to \eta\pi)$, expressed as $\Gamma(\eta\pi) \times \Gamma(\gamma\gamma)/\Gamma(Total) = 0.21 + 0.08 - 0.04$. It should be reiterated that we equate the amplitude or fit fraction of a resonance common to both decay channels, and use this as the basis of our psuedo-χ^2 penalty. Thus the

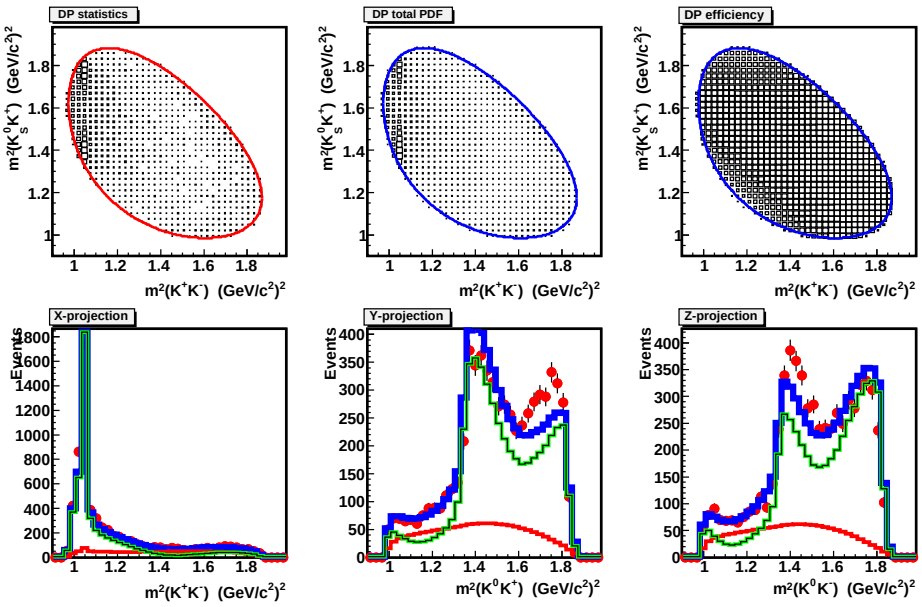

Figure 4.13: The main $D^0 \to K^0_s K^+ K^-$ Dalitz Plots. Amplitude Penalty. Top row from left: Plot statistics, Total PDF, Efficiency. Bottom Row from left: X, Y, and Z Projections. Total, signal, and background are represented by blue, green, and red lines respectively.

$K^0_s a_0(980)$ resonance on $D^0 \to K^0_s \pi^0 \eta$ is used to constrain the same resonant channel on $D^0 \to K^0_s K^+ K^-$. We fix the entire $K^0_s \pi^0 \eta$ fit, which gives us the "true" $a_0(980)$ values. The psuedo-χ^2 forces the $a_0(980) \to K^+ K^-$ in $D^0 \to K^0_s K^+ K^-$ to comport with this "true" value.

4.6 Joint Dalitz Analysis of $D^0 \to K^0_s K^+ K^-$ and $D^0 \to K^0_s \pi^0 \eta$ with Amplitude Penalty

The result of the Dalitz fit using the amplitude penalty is shown Fig. 4.13, with the details of the fit components shown in Fig. 4.14. Figs.4.15-4.17 show the x, y, and z projections along with the individual resonant components. We don't include the non-resonant component. With the penalty term in place we are able to include both $K^0_s f_0(980)$ and $K^0_s a_0(980)$. As we see in Table 4.4, both resonances have large fit fractions, but with relative phases that are nearly 180° apart.

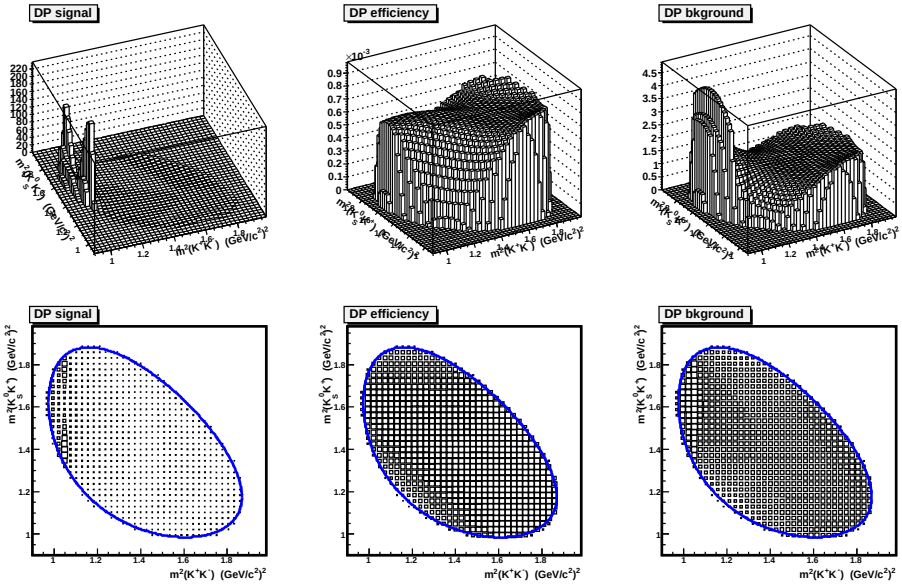

Figure 4.14: Detailed $D^0 \to K^0_s K^+ K^-$ Dalitz Plot PDF Components. Amplitude Penalty. Top Row: 3D View. Bottom Row: 2D View. From left: Signal, Efficiency, Background.

Table 4.4: Dalitz Fit Results for $D^0 \to K^0_s K^+ K^-$ with the Amplitude "Penalty" Term. Errors are statistical.

Parameter	Amplitude	Phase	Fit Fraction
$K^0_s a_0(980)^0$	16.8 ± 1.0	271.6 ± 3.5	17.9 ± 4.6
$K^0_s \phi(1020)$	1	0	0.54 ± 0.13
$K^0_s f_0(980)$	23.7 ± 1.3	108.3 ± 3.5	26.3 ± 5.1
$a_0(980)^+ K^-$	1.84 ± 0.14	335.1 ± 4.9	0.251 ± 0.076
$a_0(980)^- K^+$	2.06 ± 0.14	296.3 ± 4.3	0.317 ± 0.090
$K^0_s f_0(1370)$	1.98 ± 0.40	84 ± 13	0.087 ± 0.014

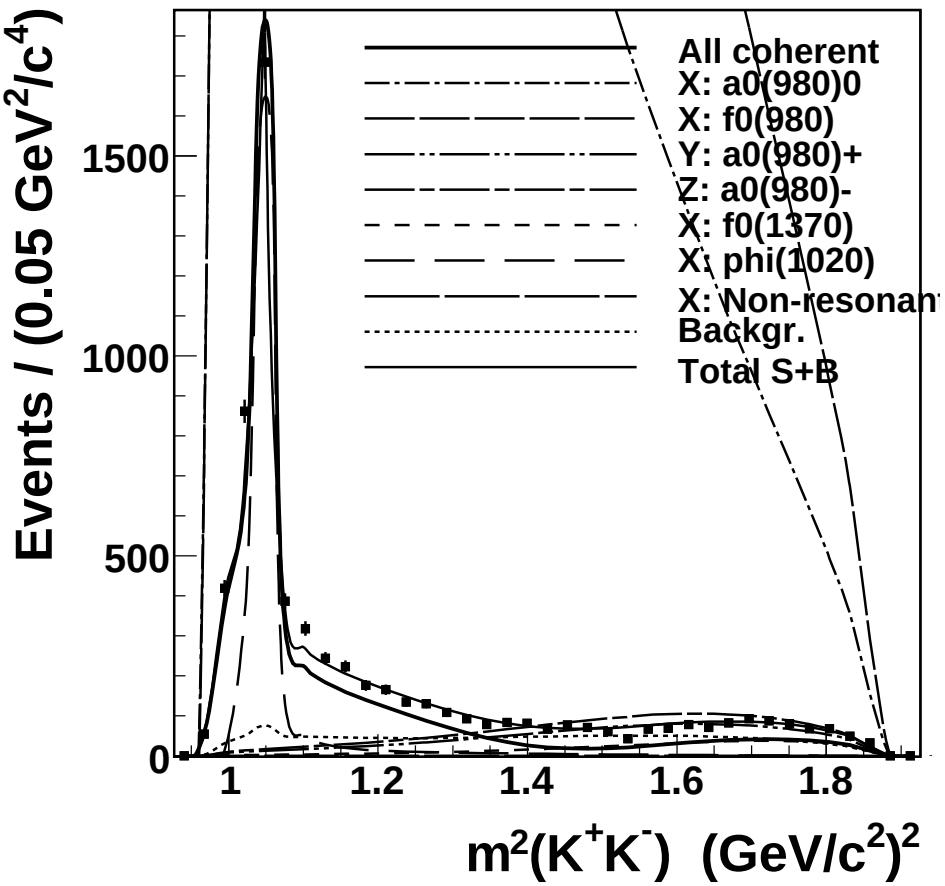

Figure 4.15: Detailed X-projection of $D^0 \to K^0_s K^+ K^-$ Dalitz Plots. Amplitude Penalty.

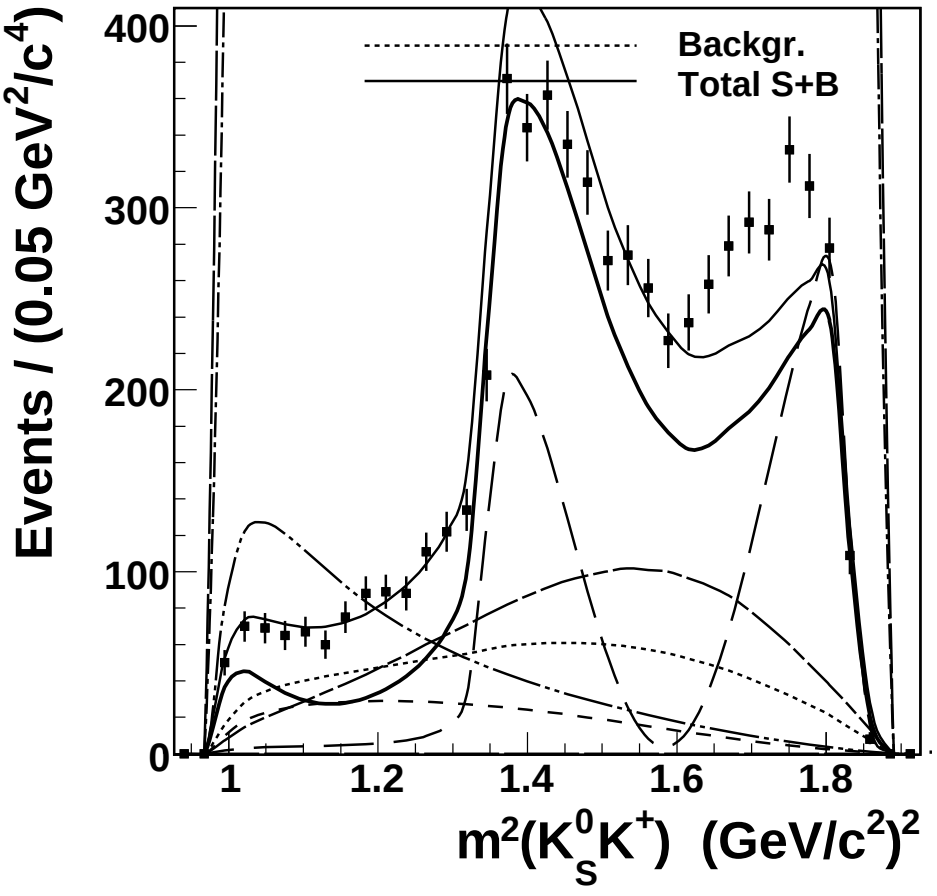

Figure 4.16: Detailed Y-projection of $D^0 \to K^0_s K^+ K^-$ Dalitz Plots. Amplitude Penalty.

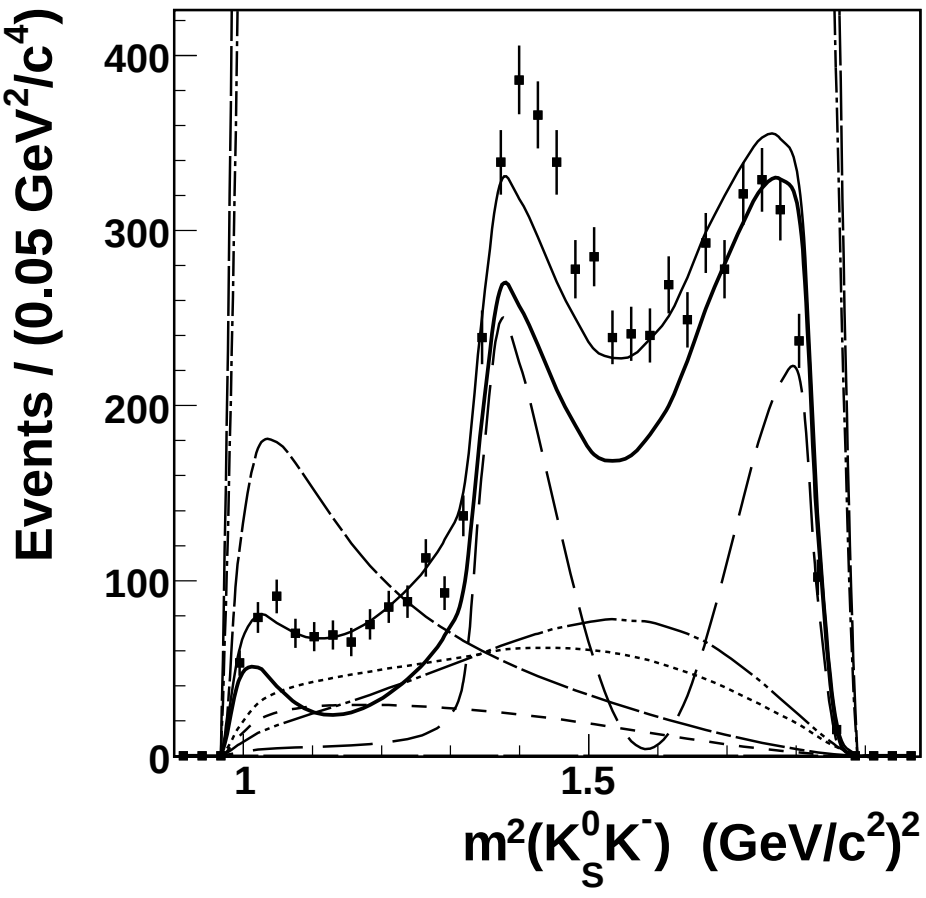

Figure 4.17: Detailed Z-projection of $D^0 \to K^0_s K^+ K^-$ Dalitz Plots. Amplitude Penalty.

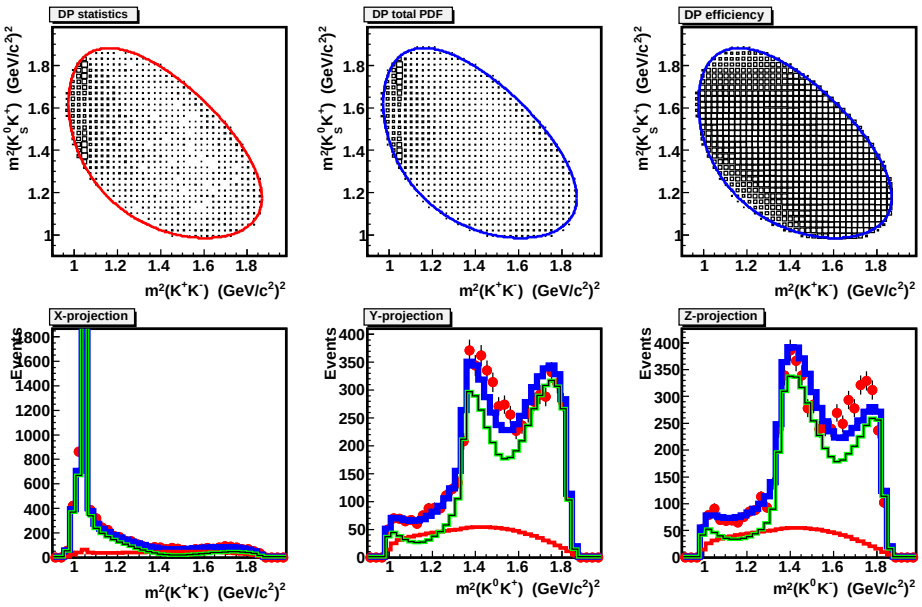

Figure 4.18: The main $D^0 \to K^0_s K^+ K^-$ Dalitz Plot. Fit Fraction Penalty. Top row from left: Plot statistics, Total PDF, Efficiency. Bottom Row from left: X, Y, and Z Projections. Total, signal, and background are represented by blue, green, and red lines respectively.

4.7 Joint Dalitz Analysis of $D^0 \to K^0_s K^+ K^-$ and $D^0 \to K^0_s \pi^0 \eta$ with Fit Fraction Penalty

We replace the Amplitude penalty term with a Fit Fraction version; the resultant main plots are shown in Fig. 4.18. The detail plots are shown in Fig. 4.19. The projection plots in Figs. 4.20–4.22 also show large $K^0_s a_0(980)^0$ and $K^0_s f_0(980)$ components, with phase angles in Table 4.5 comparable to those of the Amplitude penalty.

When we compare the Amplitude and Fit Fraction methods, we find important similarities and potentially important differences. The final fit fractions are identical within uncertainty, yet we have almost mirror image fits in the Y– and Z–projections. The Amplitude projections underrepresent the higher mass lobe of the $\phi(1020)$ in the Y–projection while simultaneously underreporting the low mass lobe in Z. The Fit Fraction method does the opposite in Y and Z.

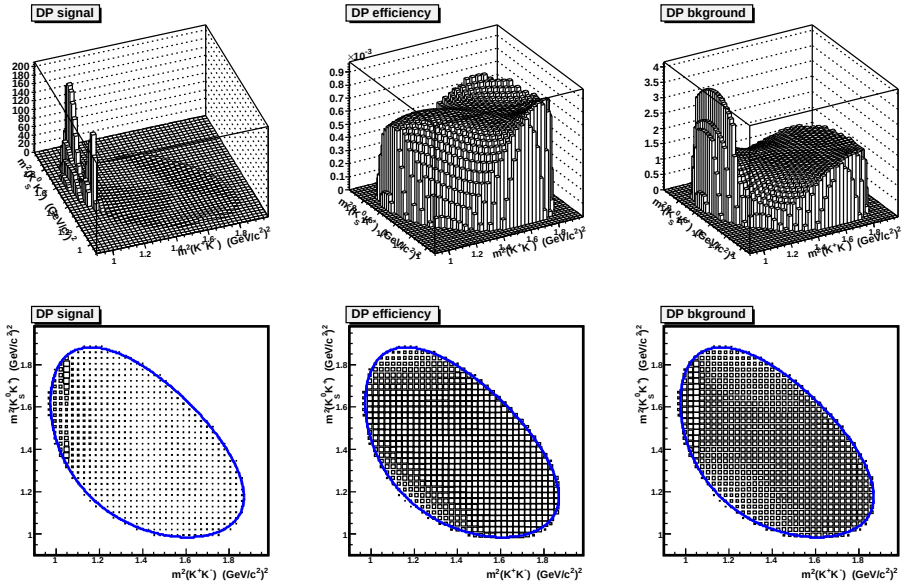

Figure 4.19: Detailed $D^0 \to K^0_s K^+ K^-$ Dalitz Plot PDF Components. Fit Fraction Penalty. Top Row: 3D View. Bottom Row: 2D View. From left: Signal, Efficiency, Background.

Table 4.5: Dalitz Fit Results for $D^0 \to K^0_s K^+ K^-$ with the Fit Fraction "Penalty" Term. Errors are statistical.

Parameter	Amplitude	Phase	Fit Fraction
$K^0_s a_0(980)^0$	13.05 ± 0.87	80.5 ± 6.6	11.1 ± 3.4
$K^0_s \phi(1020)$	1	0	0.55 ± 0.16
$K^0_s f_0(980)$	18.6 ± 1.1	280.2 ± 6.7	16.6 ± 4.5
$a_0(980)^+ K^-$	1.71 ± 0.16	112.2 ± 6.5	0.223 ± 0.071
$a_0(980)^- K^+$	1.46 ± 0.17	153.6 ± 5.1	0.163 ± 0.056
$K^0_s f_0(1370)$	1.77 ± 0.44	239 ± 17	0.071 ± 0.022

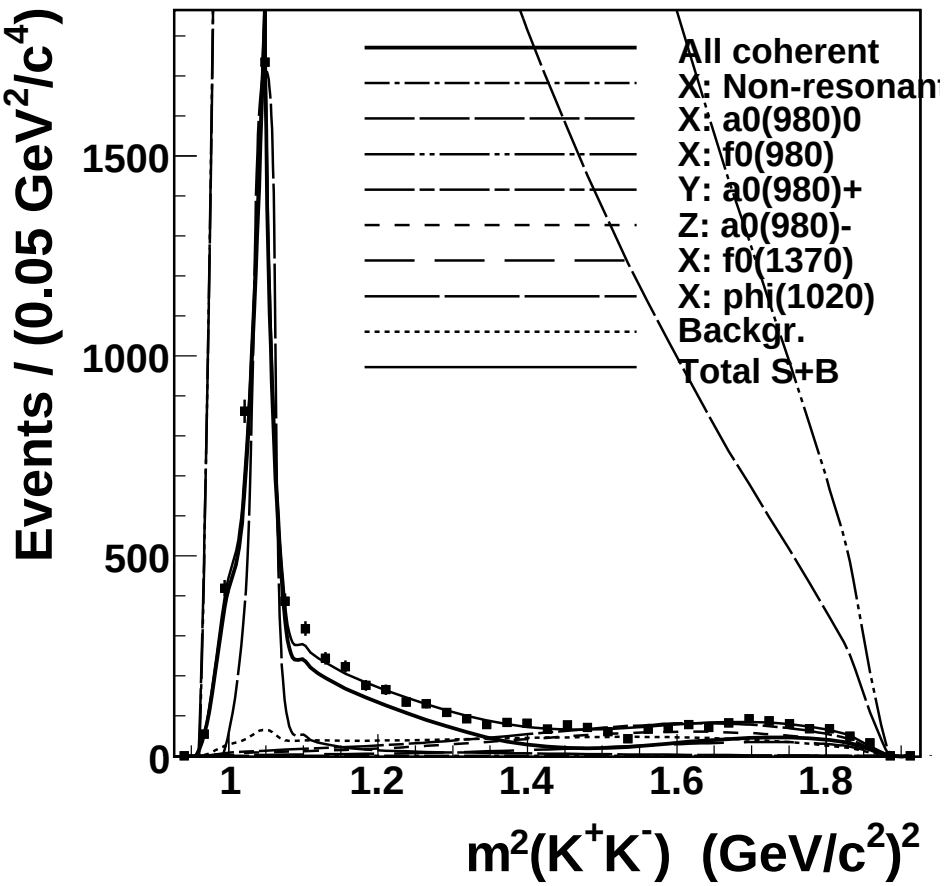

Figure 4.20: Detailed X-projection of $D^0 \to K^0_s K^+ K^-$ Dalitz Plot. Fit Fraction Penalty.

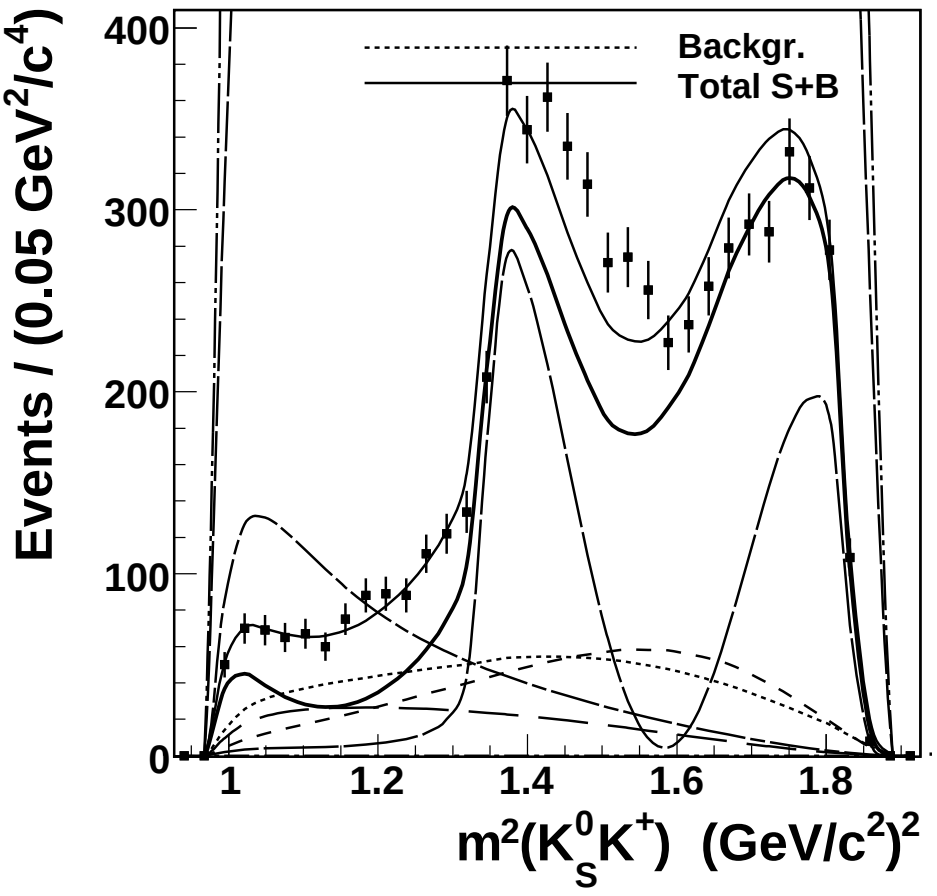

Figure 4.21: Detailed Y-projection of $D^0 \to K^0_s K^+ K^-$ Dalitz Plot. Fit Fraction Penalty.

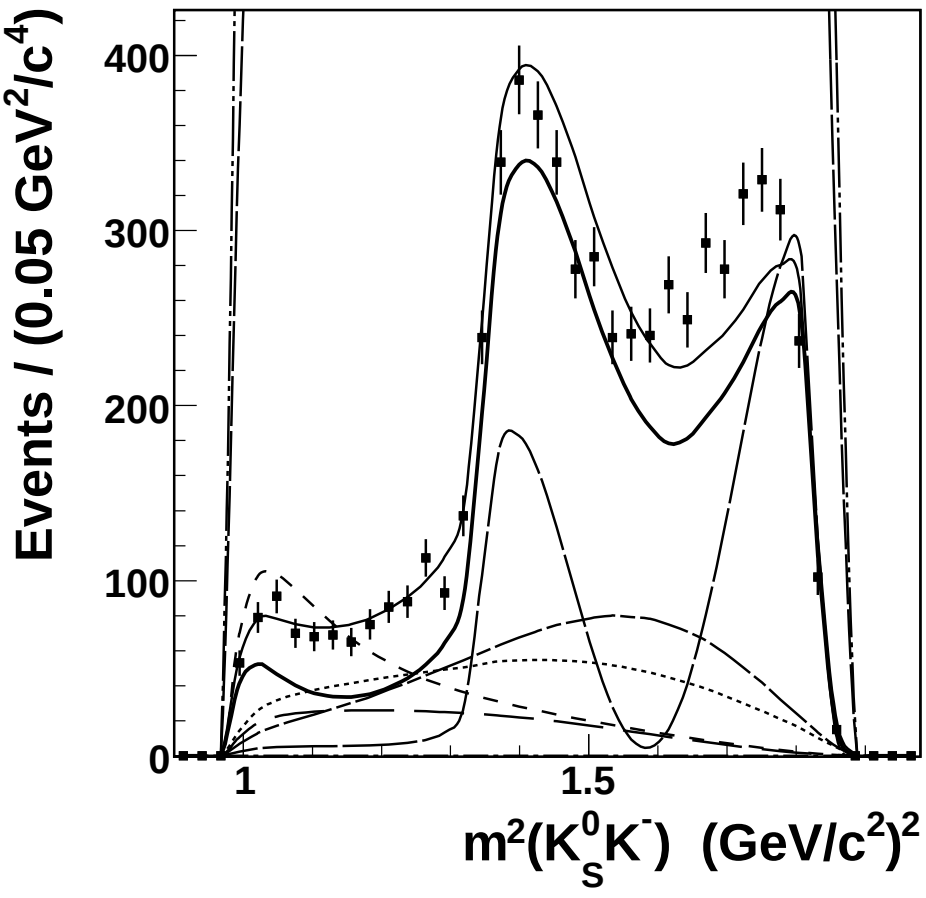

Figure 4.22: Detailed Z-projection of $D^0 \to K^0_s K^+ K^-$ Dalitz Plot. Fit Fraction Penalty.

CHAPTER 5: CONCLUSIONS

5.1 Best Fit Method and Systematic Uncertainties

From the data in the preceding chapter, we find two competing pseudo–χ^2 methods that give similar results. Using the $a_0(980)$ found in the Dalitz fit of $D^0 \to K^0_s\pi^0\eta$ to constrain that found in $D^0 \to K^0_sK^+K^-$, we find a significant $f_0(980)$ component not found in the "non-penalty" fit. Whether we construct our penalty from constraining Fit Fractions of amplitudes, we find the $f_0(980)$ and $a_0(980)$ are dominant in the $K^0_sK^+K^-$ Dalitz decay. Both show these two resonances with near complete destructive interference, and the presence of a small, wide component also generally agrees with the BABAR result.

So which is superior? Though the Amplitude penalty method requires less computing power and has smaller statistical uncertainty, we find the Fit Fraction method the best overall. Its errors better comport with the statistics of the data sample. Additionally, when we compare Figs. 4.13 and 4.18, the Fit Fraction result more closely captures the shape of the data, particularly in the Y projection. If we compare fit fractions, we also see that the FF method has smaller values for the interferring $f_0(980)$ and $a_0(980)$ fractions.

Accepting the Fit Fraction penalty results as central values, we relegate the Amplitude method to one of several systematic errors. All of our systematics arise from the assumptions "cooked" into the final values; the best case scenario will find systematic errors that are small and symmetric about the respective central values.

For each systematic error, we change a property of the central method and re-fit. Table 5.1 contains the central result along with the systematic fits modifying fixed widths and other properties. Each systematic value shown is the difference (Central Result - Systematic Result). For $f_0(1370)$ and $\phi(1020)$, we adjust the width $\pm$0.2GeV and $\pm$0.8MeV respectively. In lieu of a width adjustment, we adjust the ratio $r_{KK/\eta\pi}$ and the $g_{\eta\pi}$ Flatté coupling of the a_0 terms $\pm$0.14 and $\pm$0.05GeV$^{1/2}$ respectively. This assumes the coupling constants for all of the a_0 charge states are identical. Similarly, the $f_0(980)$ coupling constants are both adjusted

by $\pm 0.05 \mathrm{GeV}^{1/2}$.

Table 5.2 again contains the central value, along with "protocol" systematics followed by the total systematic errors. As discussed before, having chosen the Fit Fraction penalty as the central value, we relegate the Amplitude method result to a systematic. In the Fit Fraction penalty we simultaneously fit ε, $|\mathcal{M}|^2$, and $\mathcal{B}$ of the dynamics matrix. Thus the final two systematics test the efficacy of fixing the Efficiency or Background.

Table 5.1: Dalitz Fit Results for $D^0 \to K^0_s K^+ K^-$ with Statistical and Systematic Contributions: $f_0(1370)$ γ $\pm$0.2GeV, ϕ γ $\pm$0.8MeV, a_0 $r_{KK/\eta\pi}(a_0) \pm 0.14$, $g_{\eta\pi}(a_0) \pm 0.05\text{GeV}^{1/2}$, $g_{\pi\pi}(f_0) \pm 0.05\text{GeV}^{1/2}$, $g_{KK}(f_0) \pm 0.05\text{GeV}^{1/2}$. Each systematic value shown is the difference (Systematic Result - Central Result).

Parameter	Fit Frac.	Stat.	$f_0(1370)$ γ	ϕ γ	$r_{KK/\eta\pi}(a_0)$	$g_{\eta\pi}(a_0)$	$g_{\pi\pi}(f_0)$	$g_{KK}(f_0)$
$\mathrm{a}_{a_0(980)^0}$	13.05	$\pm$0.87	7.1 0	6.2 0	4.8 0	22 −3.5	27 −0.41	5.4 0
$\varphi_{a_0(980)^0}$	80.5	$\pm$6.6	8.3 −0.0052	5.8 0	18 −5.6	5.0 −6.3	8.4 0	17 −4.4
$\mathrm{a}_{f_0(980)}$	18.6	$\pm$1.1	10 0	8.7 0	6.8 0	20 −0.73	27 0	9.7 0
$\varphi_{f_0(980)}$	280.2	$\pm$6.7	3.0 −3.1	0.78 −0.32	14 −170	9.1 −18	4.7 −5.7	12 −9.0
$\mathrm{a}_{a_0(980)^+}$	1.71	$\pm$0.16	0.54 0	0.63 0	0.47 0	0.94 0	0.53 0	0.54 0
$\varphi_{a_0(980)^+}$	112.2	$\pm$6.5	5.3 −8.0	1.5 −5.9	2.2 −0.77	7.8 −8.8	0 −0.63	0 −1.7
$\mathrm{a}_{a_0(980)^-}$	1.46	$\pm$0.17	0.34 0	0.56 0	0.38 0	0.88 −0.057	0.37 0	0.40 0
$\varphi_{a_0(980)^-}$	153.6	$\pm$5.1	0 −21	0 −18	0 −15	0 −21	0 −18	0 −16
$\mathrm{a}_{f_0(1370)}$	1.77	$\pm$0.44	3.2 −1.2	0.58 0	1.1 −0.34	1.3 −0.25	0.97 −0.028	1.1 0
$\varphi_{f_0(1370)}$	239	$\pm$17	35 0	14 0	25 0	68 0	25 0	19 0
$FF_{a_0(980)^0}$	11.1	$\pm$3.4	15 0	16 0	7.2 0	51 −3.7	90 −1.0	11 0
$FF_{f_0(980)}$	16.6	$\pm$4.5	22 0	22 0	13 0	53 −1.8	100 0	18 0
$FF_{\phi(1020)}$	0.55	$\pm$0.16	0 −0.015	0.011 −0.044	0 −0.018	0 −0.017	0 −0.018	0 −0.017
$FF_{a_0(980)^+}$	0.223	$\pm$0.071	0.15 0	0.17 0	0.15 0	0.21 0	0.15 0	0.15 0
$FF_{a_0(980)^-}$	0.163	$\pm$0.056	0.080 0	0.083 0	0.097 0	0.17 0	0.085 0	0.094 0
$FF_{f_0(1370)}$	0.071	$\pm$0.022	0.19 −0.044	0.077 0	0.11 −0.025	0.13 −0.019	0.093 −0.0033	0.10 0
Signal Frac. (f)	0.798	$\pm$0.017	0 −0.013	0 −0.012	0 −0.025	0 −0.025	0 −0.017	0 −0.016

Table 5.2: Dalitz Fit Results for $D^0 \to K^0_s K^+ K^-$ with Statistical and Systematic Contributions: Amplitude Method, Fixed Efficiency, Fixed Background, and Total Systematic Error. The Total Systematic Error includes the values from Table 5.1.

Parameter	Fit Frac.	Stat.	Amp.	Eff.	Bkgd.	Tot. Sys.
$a_{a_0(980)^0}$	13.05	± 0.87	± 4.2	1×10^{-4}	0.0013	$^{+37}_{-5.5}$
$\varphi_{a_0(980)^0}$	80.5	± 6.6	± 190	2×10^{-4}	0.0008	$^{+190}_{-190}$
$a_{f_0(980)}$	18.6	± 1.1	± 5.9	1×10^{-4}	0.0019	$^{+39}_{-5.9}$
$\varphi_{f_0(980)}$	280.2	± 6.7	± 170	1×10^{-3}	54	$^{+180}_{-180}$
$a_{a_0(980)^+}$	1.71	± 0.16	± 0.13	0	0.0013	$^{+1.5}_{-0.13}$
$\varphi_{a_0(980)^+}$	112.2	± 6.5	± 220	1×10^{-4}	0.072	$^{+220}_{-220}$
$a_{a_0(980)^-}$	1.46	± 0.17	± 0.62	1×10^{-3}	0.0018	$^{+1.4}_{-0.62}$
$\varphi_{a_0(980)^-}$	153.6	± 5.1	± 140	3.8×10^{-3}	0.020	$^{+140}_{-150}$
$a_{f_0(1370)}$	1.77	± 0.44	± 0.30	0	0.0029	$^{+3.9}_{-1.3}$
$\varphi_{f_0(1370)}$	239	± 17	± 160	4.9×10^{-3}	0.060	$^{+180}_{-160}$
$FF_{a_0(980)^0}$	11.1	± 3.4	± 7.5	1.2×10^{-4}	0.0055	$^{+110}_{-8.4}$
$FF_{f_0(980)}$	16.6	± 4.5	± 11	1×10^{-5}	0.0083	$^{+120}_{-11}$
$FF_{\phi(1020)}$	0.55	± 0.16	± 0.025	0	0.00016	$^{+0.027}_{-0.069}$
$FF_{a_0(980)^+}$	0.223	± 0.071	± 0.023	2×10^{-5}	0.00028	$^{+0.40}_{-0.023}$
$FF_{a_0(980)^-}$	0.163	± 0.056	± 0.15	1×10^{-5}	0.00034	$^{+0.30}_{-0.15}$
$FF_{f_0(1370)}$	0.071	± 0.022	± 0.022	1×10^{-5}	0.00026	$^{+0.30}_{-0.059}$
Signal Frac. (f)	0.798	± 0.017	± 0.0041	0	0.0007	$^{+4.2\times10^{-3}}_{-0.045}$

In the process of compiling the systematics, we notice that the $a_0(980)$ amplitudes and fit fractions are always smaller than their $f_0(980)$ counterparts, regardless of the given fit. When we graph either the amplitudes (Fig. 5.1) or fit fractions (Fig. 5.2), we unsurprisingly find a strong linear correlation. This is confirmed upon examining the correlation matrix in Table 5.3. Additionally, we find a strong correlation between $\varphi_{a_0(980)^0}$ and $\varphi_{f_0(980)}$.

Examining the systematics and correlation matrix, we can make several conclusions:

- Phase angles are completely unknown. There is non-trivial correlation among the phase angles and amplitudes, which suggests that the relative angles don't change even if the absolute values are arbitrary.

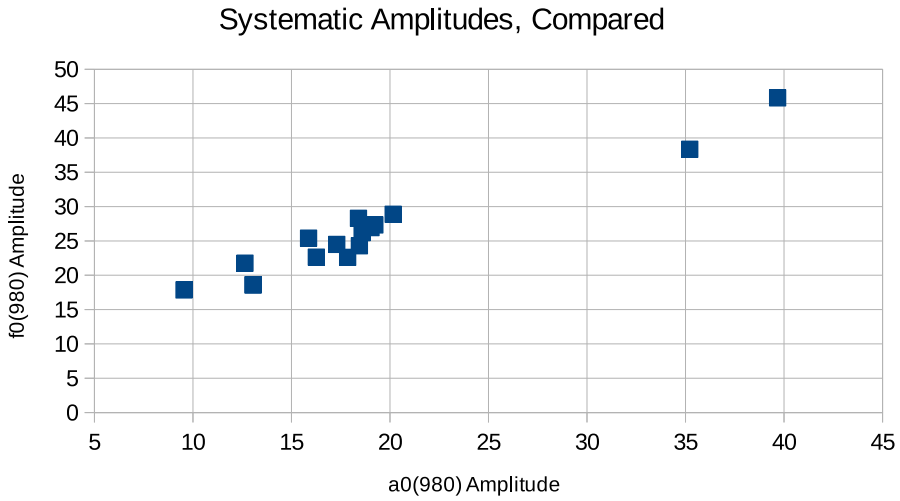

Figure 5.1: Systematic Amplitudes: $a_0(980)$ vs. $f_0(980)$.

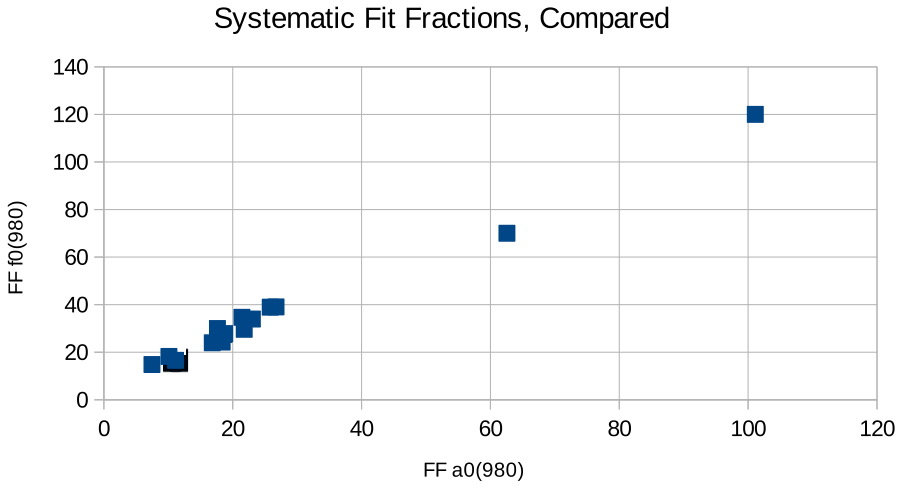

Figure 5.2: Systematic Fit Fractions: $a_0(980)$ vs. $f_0(980)$.

Table 5.3: Correlation Matrix for the Fit Fraction Method Dalitz Fit of $D^0 \to K^0_s K^+ K^-$

	$a_{f_0(980)}$	$\varphi_{f_0(980)}$	$a_{a_0(980)^0}$	$\varphi_{a_0(980)^0}$	$a_{a_0(980)^+}$	$\varphi_{a_0(980)^+}$	$a_{f_0(1370)}$	$\varphi_{f_0(1370)}$	$a_{a_0(980)^-}$	$\varphi_{a_0(980)^-}$
$a_{f_0(980)}$	1									
$\varphi_{f_0(980)}$	-0.041684	1								
$a_{a_0(980)^0}$	0.91316	-0.4126	1							
$\varphi_{a_0(980)^0}$	0.10399	0.98669	-0.27779	1						
$a_{a_0(980)^+}$	0.18636	0.62131	-0.032166	0.6125	1					
$\varphi_{a_0(980)^+}$	-0.22002	0.66984	-0.37308	0.62766	0.54786	1				
$a_{f_0(1370)}$	0.44388	-0.055087	0.31948	0.014463	-0.30697	-0.56975	1			
$\varphi_{f_0(1370)}$	-0.010979	0.77653	-0.26612	0.74334	0.87759	0.61962	-0.25617	1		
$a_{a_0(980)^-}$	-0.07061	0.68563	-0.25713	0.64819	0.768	0.69404	-0.58346	0.81658	1	
$\varphi_{a_0(980)^-}$	-0.44868	0.33382	-0.49568	0.28386	-0.050605	0.26552	-0.22164	0.0019913	0.2118	1

- The systematics are largely driven by the difference between our pseudo–χ^2 terms, particularly with regard to phase angle. The fit fractions for $a_0(980)^0$ and $f_0(980)$ are unsurprisingly sensitive to both sets of coupling constants.

- A fixed efficiency doesn't change anything. Once we have sucessfully fit the coefficients, it is unimportant whether the efficiency floats against signal or not.

- Aside from $\varphi_{f_0(980)}$, fixing the background is also unimportant.

5.2 Systematics of $D^0 \to K^0_s \pi^0 \eta$

As with the previous section, we modify properties of the central $D^0 \to K^0_s \pi^0 \eta$ fit to determine the systematic error. As shown in Table 5.4, we adjust the widths or similar values, and record the systematic value of (Central Result - Systematic Result). We adjust the following widths: $K^*_0(1370)$ by ± 0.240GeV, κ ($K_0(800)$) by ± 48MeV, and $K^*_0(892)$ by ± 2.7MeV. We assume the $K^*_0(1370)$ width applies to both ηK^0 and $\pi^0 K^0$ decay channels. As with the penalty fit, we change the Flatté ratio and coupling constant of $a_0(980)$ by ± 0.14 and $\pm 0.05\text{GeV}^{1/2}$ respectively. I also change the magnitude of the $\omega(782)$ background Gaussian by $\pm 1.87 \times 10^{-5}$. For more details on the $\omega(782)$ background, see the Appendix. Table 5.5 contains the systematics from fixing the background fit with respect to the signal fit, floating the efficiency with respect to signal, and the total systematic error.

Table 5.4: Dalitz Fit Results for $D^0 \to K^0_s\pi^0\eta$ with Statistical and Systematic Contributions: $K^*_0(1370)\ \gamma$ ± 0.240GeV, $\kappa\ \gamma$ ± 48MeV, $r_{KK/\eta\pi}(a_0) \pm 0.14$, $g_{\eta\pi}(a_0) \pm 0.05\text{GeV}^{1/2}$, $K^*_0(892) \pm 2.7$MeV, and ω Background Gaussian $\pm 1.87 \times 10^{-5}$. Each systematic value shown is the difference (Systematic Result - Central Result).

Parameter	Fit Frac.	Stat.	$K^*_0(1430)\ \gamma$	$\kappa\ \gamma$	$r_{KK/\eta\pi}(a_0)$	$g_{\eta\pi}(a_0)$	$K^*_0(892)$	Bkg. ω
$a_{K^*_0(1430)(\eta K^0)}$	0.132	± 0.070	$^{0.10}_{-0.11}$	$^{0.015}_{-0.012}$	$^{0.8}_{-4} \times 10^{-3}$	$^{0.037}_{-0.033}$	$^{4}_{-5} \times 10^{-4}$	$^{4.6}_{-3.9} \times 10^{-3}$
$\varphi_{K^*_0(1430)(\eta K^0)}$	1112	± 32	$^{0}_{-35}$	$^{2.6}_{-3.0}$	$^{1.7}_{-0.16}$	$^{6.0}_{-3.7}$	$^{0.34}_{-0.25}$	$^{0.99}_{-1.6}$
$a_{K^*_0(892)}$	0.23	± 0.03	$^{0.027}_{-0.006}$	$^{0.026}_{-0.022}$	$^{1.4}_{-1.9} \times 10^{-3}$	$^{7.4}_{-9.2} \times 10^{-3}$	$^{9.6}_{-9.7} \times 10^{-3}$	$^{2.1}_{-1.8} \times 10^{-3}$
$\varphi_{K^*_0(892)}$	312.6	± 9.3	$^{9.5}_{-12}$	$^{1.3}_{-1.1}$	$^{0.31}_{-0.24}$	$^{4.5}_{-4.4}$	$^{0.12}_{-0.12}$	$^{0.15}_{-0.145}$
$a_{a_0(980)^0}$	1.14	± 0.13	$^{0.13}_{-0.019}$	$^{0.13}_{-0.11}$	$^{0.063}_{-0.060}$	$^{0.16}_{-0.16}$	$^{0.9}_{-1.1} \times 10^{-3}$	$^{0.016}_{-0.013}$
$\varphi_{a_0(980)^0}$	256.3	± 8.4	$^{11}_{-12}$	$^{1.3}_{-1.0}$	$^{4.6}_{-3.96}$	$^{4.2}_{-3.8}$	$^{0.41}_{-0.38}$	$^{0.60}_{-0.70}$
$a_{K^*_0(1430)}$	1.12	± 0.36	$^{1.1}_{-0.44}$	$^{0.084}_{-0.060}$	$^{0.13}_{-0.11}$	$^{0.22}_{-0.20}$	$^{0.013}_{-0.012}$	$^{0.027}_{-0.028}$
$\varphi_{K^*_0(1430)}$	204	± 18	$^{11}_{-14}$	$^{2.5}_{-3.1}$	$^{1.5}_{-0.24}$	$^{2.4}_{-1.7}$	$^{0.45}_{-0.41}$	$^{1.7}_{-2.2}$
$FF_{a_0(980)^0}$	1.255	± 0.023	$^{0.043}_{-5.4\times10^{-3}}$	$^{4.9}_{-7.1} \times 10^{-4}$	$^{0.012}_{-0.018}$	$^{0.090}_{-0.094}$	$^{90}_{-2.8\times10^{-3}}$	$^{8.8}_{-7.4} \times 10^{-3}$
$FF_{K^*_0(892)}$	0.231	± 0.054	$^{3.3\times10^{-3}}_{0}$	$^{5.4}_{-3.5} \times 10^{-4}$	$^{2.6}_{-2.2} \times 10^{-3}$	$^{2.9}_{-2.2} \times 10^{-3}$	$^{100}_{-6.7\times10^{-3}}$	$^{3.9}_{-5.5} \times 10^{-4}$
$FF_{K^*_0(1430)}$	0.059	± 0.018	$^{0.052}_{-0.025}$	$^{5.2}_{-3.9} \times 10^{-3}$	$^{0.015}_{-0.010}$	$^{0.020}_{-0.015}$	$^{1.2}_{-9.2} \times 10^{-3}$	$^{4.0}_{-4.1} \times 10^{-3}$
FF_{κ}	0.323	± 0.044	$^{0.022}_{-0.062}$	$^{0.021}_{-0.023}$	$^{2.4}_{-0.22} \times 10^{-3}$	$^{0.032}_{-0.023}$	$^{0.12}_{-1.3\times10^{-3}}$	$^{5.6}_{-6.6} \times 10^{-3}$
$FF_{K^*_0(1430)(\eta K^0)}(\times 10^{-3})$	6.6	± 5.0	$^{0}_{-4.5}$	$^{0.05}_{-0.04}$	$^{0.07}_{-0.35}$	$^{3.4}_{-2.5}$	$^{0.02}_{-3.3}$	$^{0.32}_{-0.28}$
Signal Frac. (f)	0.299	± 0.020	$^{1.5}_{-7.5} \times 10^{-3}$	$^{5}_{-6} \times 10^{-4}$	$^{0.012}_{-0.015}$	$^{7.6\times10^{-3}}_{-0.0104}$	$^{1}_{-2} \times 10^{-4}$	$^{5.6}_{-4.7} \times 10^{-3}$

Table 5.5: Dalitz Fit Results for $D^0 \to K^0_s\pi^0\eta$ with Statistical and Systematic Contributions: Floated Efficiency, Fixed Background, and Total Systematic Error. The Total Systematic Error includes the values from Table 5.4.

Parameter	Fit Frac.	Stat.	Eff.	Bkgd.	Tot. Sys.
$a_{K^*_0(1430)(\eta K^0)}$	0.132	± 0.070	0.003	0	$^{+0.11}_{-0.12}$
$\varphi_{K^*_0(1430)(\eta K^0)}$	111	± 32	5.2	0.0056	$^{+20}_{-36}$
$a_{K^*_0(892)}$	0.23	± 0.03	0.0021	0	$^{+0.040}_{-0.026}$
$\varphi_{K^*_0(892)}$	312.6	± 9.3	0.66	0.002	$^{+11}_{-13}$
$a_{a_0(980)^0}$	1.14	± 0.13	0.010	0	$^{+0.25}_{-0.20}$
$\varphi_{a_0(980)^0}$	256.3	± 8.4	0.98	0.0008	$^{+13}_{-13}$
$a_{K^*_0(1430)}$	1.12	± 0.36	0.0095	0	$^{+1.1}_{-0.50}$
$\varphi_{K^*_0(1430)}$	204	± 18	0.60	0.0027	$^{+12}_{-15}$
$FF_{a_0(980)^0}$	1.255	± 0.023	0.0064	0	$^{+0.10}_{-0.096}$
$FF_{K^*_0(892)}$	0.231	± 0.054	0.0012	0	$^{+0.0083}_{-0.0075}$
$FF_{K^*_0(1430)}$	0.059	± 0.018	0.0017	0	$^{+0.058}_{-0.032}$
FF_{κ}	0.323	± 0.044	0.0040	0.00001	$^{+0.045}_{-0.071}$
$FF_{K^*_0(1430)(\eta K^0)}$	0.0066	± 0.0050	0.00021	0	$^{+0.0035}_{-0.0052}$
Signal Frac. (f)	0.299	± 0.020	0.0018	0	$^{+0.016}_{-0.020}$

5.3 Summary

In this thesis, I present a technique to use one Dalitz of a 3–body D^0 decay to constrain another. To my knowledge this is the first attempt to do this. In this analysis, I model the decay of $D^0 \to K^0_s K^+ K^-$ using the folowing channels: $K^0_s a_0(980)$, $K^0_s f_0(980)$, $K^0_s \phi(1020)$, $K^0_s f_0(1370)$, and $a_0(980) \pm K\mp$. Using the techniques described in Section 4.5 to constrain $K^0_s a_0(980)$, I find that both $K^0_s a_0(980)$ and $K^0_s f_0(980)$ are large contributions to the Dalitz plot that destructively interfere. This interference leaves the $K^0_s \phi(1020)$ channel as the dominant contribution to the observed Dalitz plot. Table 5.6 gives a summary of my findings with total errors.

Persuant to the Dalitz fit of $D^0 \to K^0_s K^+ K^-$, I perform the Dalitz plot analysis of $D^0 \to K^0_s \pi^0 \eta$. I include the following resonances in my model: $K^0_s a_0(980)$, $K^*(892)\eta$, $\kappa\eta$,

Table 5.6: Summary of Dalitz Fit Results for $D^0 \to K^0_s K^+ K^-$ using the Fit Fraction "Penalty" Method. Errors are Total Statistical and Systematic Error.

Parameter	Amplitude	Phase	Fit Fraction
$a_0(980)^0$	$13.05\ ^{37}_{-5.6}$	$80.5\ ^{190}_{-190}$	$11.1\ ^{110}_{-9.1}$
$f_0(980)$	$18.6\ ^{39}_{-6.0}$	$280.2\ ^{180}_{-180}$	$16.6\ ^{120}_{-12}$
$a_0(980)^+$	$1.71\ ^{1.5}_{-0.21}$	$112.2\ ^{220}_{-220}$	$0.223\ ^{0.41}_{-0.075}$
$a_0(980)^-$	$1.46\ ^{1.4}_{-0.64}$	$153.6\ ^{140}_{-150}$	$0.163\ ^{0.31}_{-0.16}$
$f_0(1370)$	$1.77\ ^{3.9}_{-1.4}$	$239\ ^{180}_{-160}$	$0.071\ ^{0.30}_{0.063}$
$\phi(1020)$	1	0	$0.55\ ^{0.16}_{-0.17}$
Signal Frac. (f)	$0.798\ ^{0.043}_{0.034}$		

and two $K^*(1430)^0$ channels, $K^*(1430)^0\eta$ and $K^*(1430)^0\pi^0$. This analysis is an update to an earlier CLEO II.V result [14]. In the course of this analysis, I find the presence of a peaking background from $D^0 \to \omega\eta$. This background is explored in greater detail in the Appendix. A summary of my results are shown in Table 5.7.

Table 5.7: Summary of Dalitz Fit Results for $D^0 \to K^0_s \pi^0 \eta$. Errors are Total Statistical and Systematic Error.

Parameter	Amplitude	Phase	Fit Fraction
$K^*_0(1430)(\eta K^0)$	$0.132\ ^{0.13}_{-0.14}$	$111\ ^{38}_{-48}$	$\left(6.6\ ^{6.1}_{-7.2}\right) \times 10^{-3}$
$K^*_0(892)$	$0.23\ ^{0.050}_{-0.040}$	$312.6\ ^{14}_{-16}$	$0.231\ ^{0.055}_{-0.055}$
$a_0(980)^0$	$1.14\ ^{0.28}_{-0.24}$	$256.3\ ^{15}_{-15}$	$1.255\ ^{0.10}_{0.099}$
$K^*_0(1430)$	$1.12\ ^{1.1}_{-0.61}$	$204\ ^{21}_{-23}$	$0.059\ ^{0.061}_{0.037}$
κ ($K^*(800)$)	1	0	$0.323\ ^{0.063}_{-0.083}$
Signal Frac. (f)	$0.299\ ^{0.026}_{-0.029}$		

5.4 Possibilities for Future Work

We had hoped that we would be able to make a definitive statement about what is conserved in 3–body D decays, the amplitude or fit fraction, and shed light on the underlying quantum structure of D decays. Having found both methods give equally good descriptions of our data, we are unsuccessful in this effort. The methodologies presented herein can be

extended to other 3–body D decays to atempt to build a unified picture and give insight on the nature of the QCD interactions that underlies the formation of the resoances in Charm decays. Not only do we hope that a clarifying unified picture will emerge, but also that such clarity will be valuable as a tool for a simplified description of Charm decays.

APPENDIX A: INITIAL OBSERVATION OF $D^0 \to \omega\eta$

A.1 Introduction

As noted in Chapter 4, an anomalous peak appears in the Dalitz fit of $D^0 \to K^0_s\eta\pi^0$. As shown again in Fig. A.1, our fit doesn't account for the peak at 0.6 (GeV/c^2)^2 in the Y ($K^0_s\pi^0$) projection. On the advice of the collaboration member Paras Naik[1], we explore the possibility that this peak is due to an $\omega(782) \to \pi^+\pi^-\pi^0$ candidate whose charged pions are mis-reconstructed as a K^0_s. The $D^0 \to \omega\eta$ decay channel has previously been predicted[41] to have a $\mathcal{BF} = (3.3 \pm 0.2) \times 10^{-3}$. This paper also quotes the experimental value as $\mathcal{BF} = (2.21 \pm 0.23) \times 10^{-3}$ from BaBar. BaBar has not yet published or made a conference proceeding available for this result.

As in the main analysis, we assume charge conjugation throughout. Since the decay can proceed from both a D^0 and a $\bar{D}^0$ and we do no tagging of the D flavor we are actually measuring the average of the branching fractions of $D^0 \to \omega\eta$ and $\bar{D}^0 \to \omega\eta$.

A.2 Event Selection

This analysis is performed on the full $818pb^{-1}$ of $\psi(3770)$ CLEO-c (Section 2.4) data. All $D^0/\bar{D}^0$ candidates are reconstructed from $\pi^\pm$, π^0, and η that pass the standard CLEO-c selection criteria for inclusion in D candidates[25, 36], the "D Tags" described in Chapter 2 (2.4.4). Among the selections shown in Table A.1, we require a track momentum p between 50 MeV/c $\leq$ p $\leq$ 2 GeV/c and consistency with coming from the interaction region. We use the dE/dx and RICH data described earlier (Section 2.4.2), to identify our selected tracks as $\pi^\pm$. If dE/dx is valid we require a 3σ consistency with the $\pi^\pm$ hypothesis. For p $\geq$ 0.70 GeV and $|\cos\theta| < 0.8$ we can use RICH as well. If both RICH and dE/dx are valid, we require the combined log-likelihood $\mathcal{L}_{\pi\ K} \leq 0$ where

[1] Paras.Naik@bristol.ac.uk

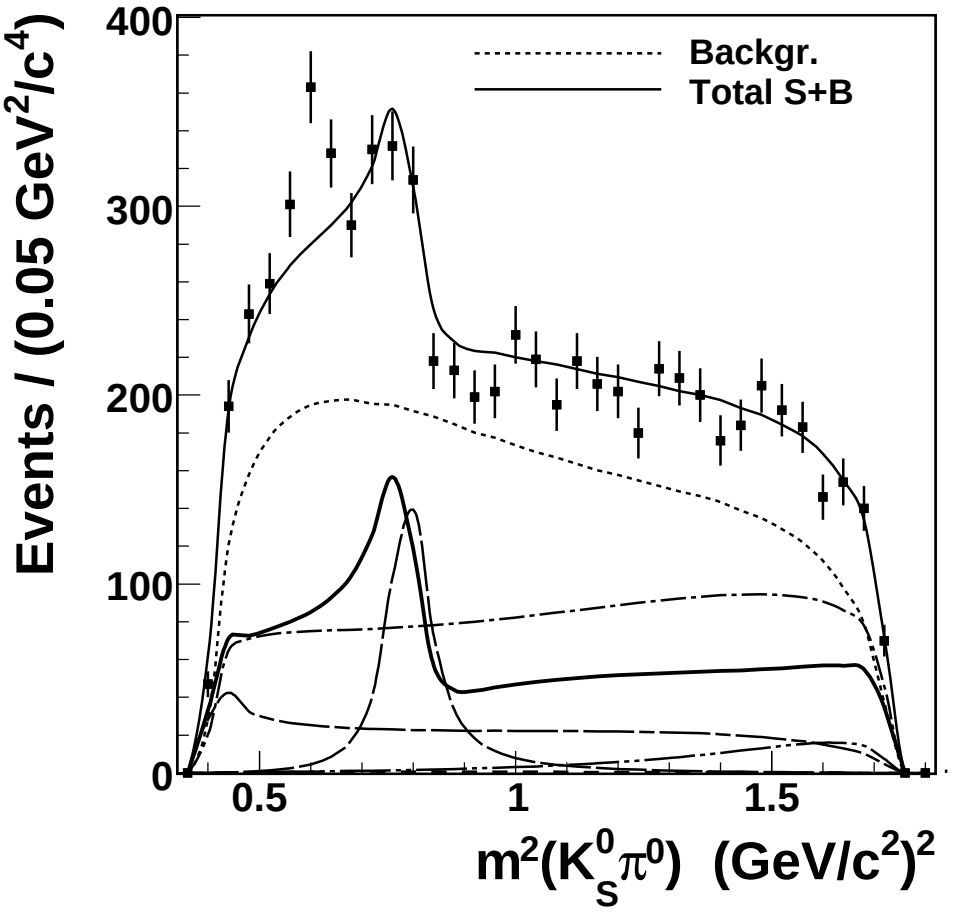

Figure A.1: $D^0 \to K^0_s\eta\pi^0$ - $K^0_s\pi^0$ (y) Projection

$$\mathcal{L}_{\pi\ K} = \sigma_\pi^2 - \sigma_K^2 + L_\pi - L_K, \quad L_h = \text{log-likelihood from RICH Data} \tag{A.1}$$

We reconstruct π^0 and η as neutral $\to \gamma\gamma$, which respectively have $\mathcal{BF} = (98.823 \pm 0.034)\%$ and $\mathcal{BF} = (39.31 \pm 0.20)\%$ PDG average branching fractions. The unconstrained mass is calculated under the assumption that the photons originate from the interaction point. We require this mass to be within 3σ of the nominal π^0/η mass. The subsequent kinematic fit must not be obviously bad ($\chi^2 < 10000$). In addition to these standard D Tag selectors we also reject neutral candidates wherein both photons are detected in the endcap and explicitly reject any photon showers with a matched track. All of the neutral selection

Table A.1: Charged Track $\pi^{\pm}$ Selection Requirements

Variable	Value
p Min	50 MeV/c
p Max	2.0 GeV/c
x-y Closet Approach	$\|db\| \leq 0.005$m
z Closest Approach	$\|z0\| \leq 0.050$m
Fit Quality	$\chi^2 \leq 100000$
Min Hit Fraction	$hitfrac \geq 0.5$
Angle	$\|\cos\theta\| \leq 0.93$

requirements are in Table A.2. Aside from the mass value and Number Sigmas Max selector, which is not implemented for η, the selections are identical.

Table A.2: π^0 and η Selection Requirements

Variable	Value
Pull Mass	3
Number Sigmas Max	1000
Min Unconstrained Mass	0
Max Unconstrained Mass	1000
Max χ^2	100000
End Cap Neutral	False
Use E9o25	False

Our D^0 candidates are reconstructed from $\pi^+\pi^-\pi^0\eta$ combinations. We make an initial skim requirement that the invariant mass $m(\pi^+\pi^-\pi^0\eta)$ be within 100 MeV/c^2 of the PDG average D^0 mass. In the next section we will describe the $\omega(782)$ reconstruction from $\pi^+\pi^-\pi^0$ combinations. For the skim these must have an invariant mass within 50 MeV/c^2 of the PDG average ω mass. We do not make any best candidate selection allowing multiple per event.

A.3 Analysis

We select ω candidates and choose cuts on the beam-constrained mass of $\omega\eta$ ($\mathrm{M_{bc}}$) and their ΔE in an iterative procedure making cuts on two of the three, fitting in the third,

choosing a cut based on the fit results, and repeating until the cut values do not change. In all cases the signal is fit to a Gaussian. In M_{bc} we fit the background to an Argus function, and use a 4^{th} order polynomial in ΔE and $m(\pi^+\pi^-\pi^0)$. Unlike M_{bc} there is no physics-inspired background shape for these, and we chose the polynomial order to give a reasonable model of background without adding meaningless nuisance parameters. We use the signal mean and sigma from one fit to make 3-standard deviation cuts on the other plots. We generate 50000 signal Monte Carlo (Section 2.5) $D^0/\bar{D}^0$ events to measure the efficiency of our reconstruction and to determine the optimal widths to use in data fitting. We take the yield from M_{bc}, shown in Figure A.2, and ΔE, Figure A.3 as our measurements of the D^0 yield in the MC. From the value of M_{bc} yield, we find an efficiency of $(17.49 \pm 0.216)\%$.

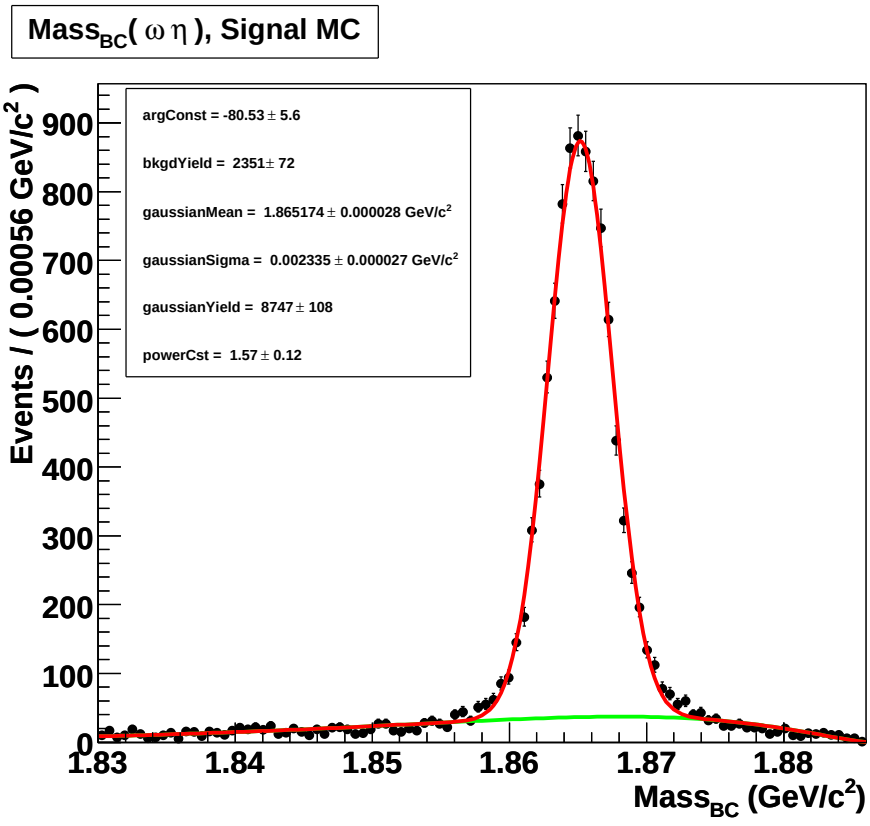

Figure A.2: Signal Monte Carlo: Beam-Constrained Mass Fit.

The same process is performed in data, but with the widths obtained in Signal Monte Carlo fixed. From the mean found in Figure A.4 and the signal Monte Carlo widths, we

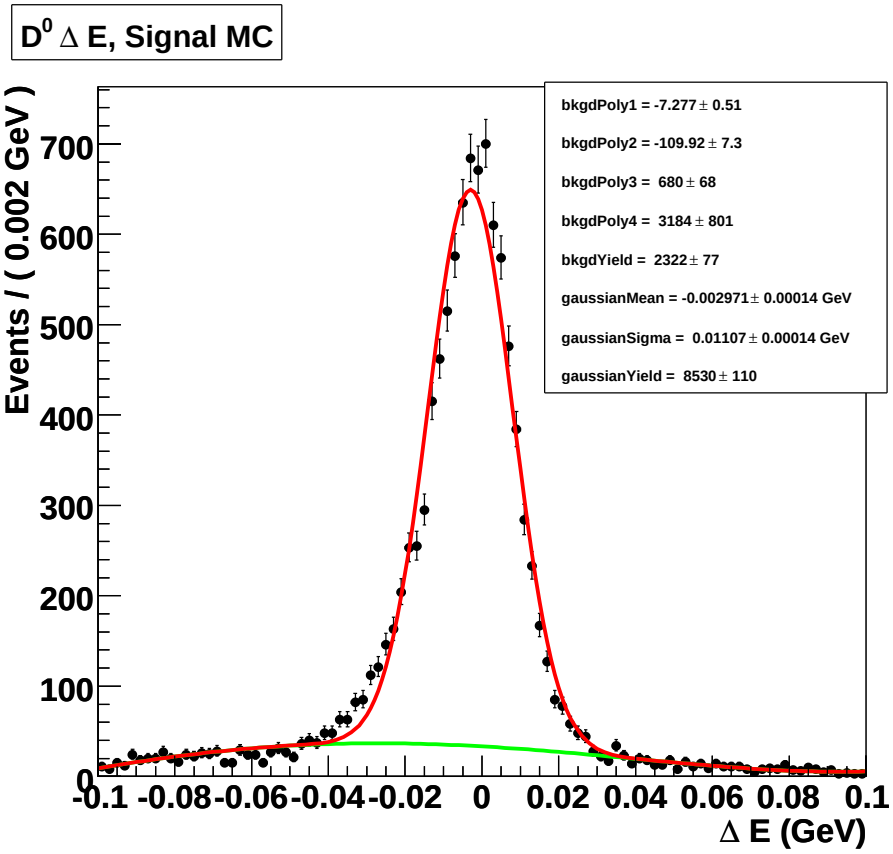

Figure A.3: Signal Monte Carlo: ΔE Fit.

choose $\omega(782)$ candidates which have 0.76016 GeV/c^2 $\leq$ m($\pi^+\pi^-\pi^0$) $\leq$ 0.80432 GeV/c^2. We note the $m(\pi^+\pi^-\pi^0)$ mass fit is simply used to select $\omega(782)$ candidates, and not as measurement of the D^0 yield.

ΔE is defined as $E_{\pi^+\pi^-\pi^0\eta} - E_{Beam}$; the distribution is shown in Figure A.5. From the fit to this we select -0.03525 GeV $\leq \Delta$E ≤ 0.03117 GeV.

The beam-constrained mass, $\mathrm{M_{bc}}^2 \equiv E_{Beam}^2 - p^2$, distribution and fit is shown in Figure A.6. Table A.3 contains a summary of the cuts we use to define the signal. Table A.4 summarizes the results of the signal yield fits. The $\mathrm{M_{bc}}$ and ΔE fit yields can both used as measurements of the $D^0 \to \omega\eta$ yield.

In the proceeding, we assume $\omega(782)$ is strongly related to the reconstruction of the D^0 and its $\mathrm{M_{bc}}$. To better visualize this relation, we look at the contour plot of $\omega(782)$ mass

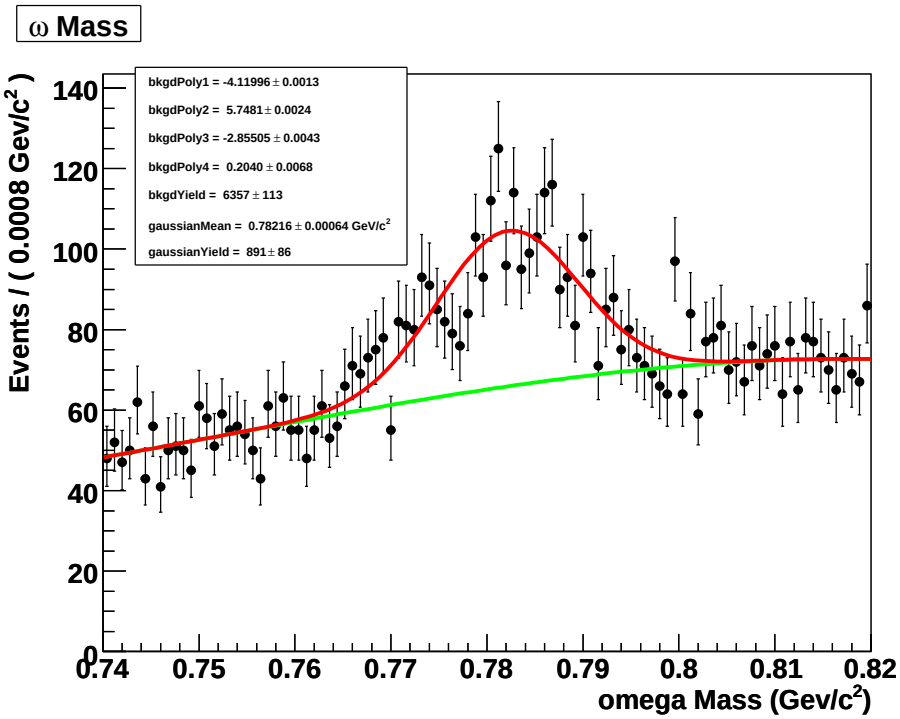

Figure A.4: Data: $m(\pi^+\pi^-\pi^0)$ invariant mass fit after signal cuts in ΔE and M_{bc}.

Table A.3: Summary of Signal Cuts

Signal Cuts
$0.76016\ \text{GeV/c}^2 \leq m(\pi^+\pi^-\pi^0) \leq 0.80432\ \text{GeV/c}^2$
$-0.03525\ \text{GeV} \leq \Delta E \leq 0.03117\ \text{GeV}$
$1.857675\ \text{GeV/c}^2 \leq M_{bc} \leq 1.871685\ \text{GeV/c}^2$

versus M_{bc} subject to a 3σ ΔE cut, as seen in Figure A.7. We can clearly see a well-populated region near the intersection of the D^0 M_{bc} and $\omega(782)$ mass. We also fit the M_{bc} below and above the ω cuts in Figure A.8 and Figure A.9 respectively. We find no meaningful D^0 presence in these sidebands.

We expect that there should be some K_s^0 contamination in our $\omega(782)$ signal; after all we began with the opposite in $K_s^0\pi^0\eta$. For our signal candidates we observe $M(\pi^+\pi^-)$ in Figure A.10. There is a clear K_s^0 peak. This histogram is fit using a Gaussian "signal" and 4^{th} order polynomial "background" using the signal region cuts found in Table A.3. We can use

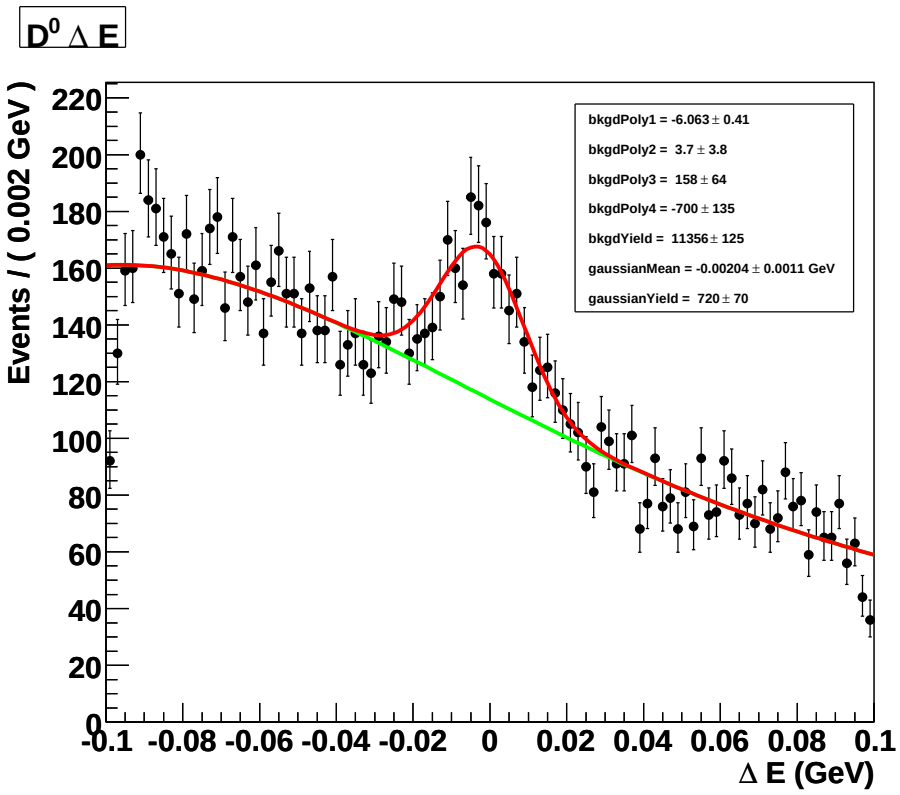

Figure A.5: Data: ΔE distribution and fit after 3σ signal cuts for the $\omega(782)$ and on M_{bc}.

this in two alternate ways. The first and simplest method is to subtract the "signal" yield in Figure A.10 from our previous results. We determine how many of the 158 ± 20 K_s^0 events should be subtracted by examining M_{bc} in three regions: $\pm 3\sigma$ about the K_s^0 mean and the two sidebands. We fit M_{bc} using the previously outlined method, and find the signal and background yields under the peak. Using the signal fraction in the K_s^0 region from Table A.5, we subtract 43 ± 17 from the Table A.4 values. The K_s^0 subtraction value includes a 10% uncertainty due to our inability to precisely know how many K_s^0 lie in signal versus background.

In a second method we veto the $K_s^0\pi^0$ contribution to $\omega(782)$ by cutting out the K_s^0 region in $M(\pi^+\pi^-)$. Aside from the veto, the analysis is identical to the original description. The new efficiency fits of M_{bc} and ΔE are shown in Figures A.11 and A.12. From this value of M_{bc} yield, we find an efficiency of $(16.13 \pm 0.208)\%$ which represents an 7.8% reduction

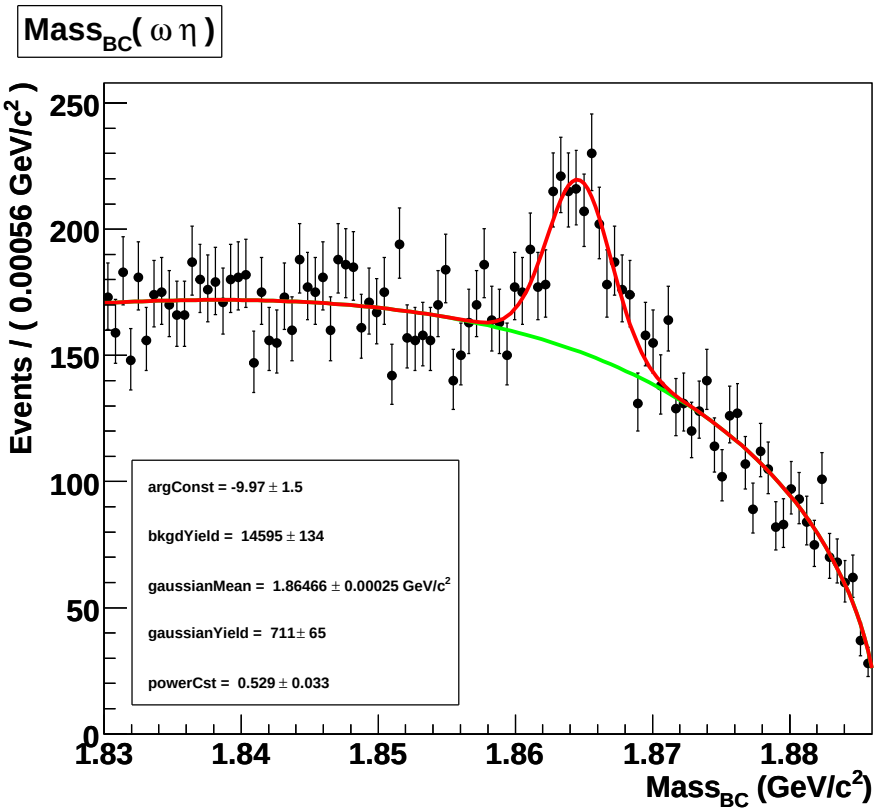

Figure A.6: Data: M_{bc} fit after the 3σ signal cuts on $\omega(782)$ and ΔE.

with respect to the uncut/K_s^0-subtracted efficiency.

Repeating the Data analysis with the K_s^0 veto, we use the width found in signal Monte Carlo and the mean shown in Figure A.13 we make our new $\omega(782)$ candidate selection. From the fits of ΔE in Figure A.14 and M_{bc} in Figure A.15 we determine the signal cuts. Table A.6 contains the K_s^0 veto cuts along with all of the new candidate selections. Table A.7 contains the yields from ΔE and M_{bc} corrected by both K_s^0 subtraction and veto, as well as their associated efficiencies and Yield/Efficiency values.

We also attempted a 2D fit in M_{bc} and ΔE. In Figure A.16 we see the projection of this 2D fit on the ΔE variable with the signal overwhelmed by the background. We are not confident that we understand the ΔE background shape well enough to use this 2D fit to extract a yield.

The proceeding analysis used the widths from Signal Monte Carlo, fixed in the data fits.

Table A.4: Signal Yields From Fitting without K_s^0 Contamination Corrections

Plot	Signal	Signal Monte Carlo
M_{bc}	711 ± 65	8747 ± 108
ΔE	720 ± 70	8530 ± 110

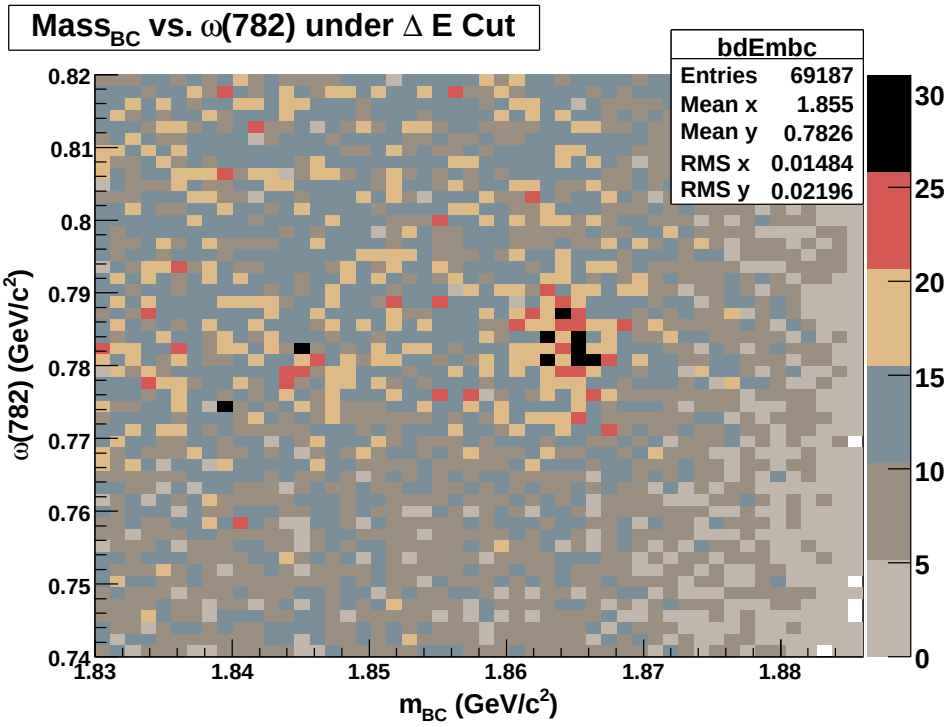

Figure A.7: Data: M_{bc} Versus $\omega(782)$ Mass under 3σ ΔE Cut

When we float the data widths, we find 637 ± 89 and 521 ± 85 for the M_{bc} and ΔE signal yields, respectively. These values greatly differ from those with fixed widths, and indeed greatly from each other. We will use the difference between fixed and floating M_{bc} yields as a systematic uncertainty.

We calculate the Branching Fraction using

$$\mathcal{BF} = \frac{N_{D^0 \to \omega\eta}}{2\epsilon_{D^0 \to \omega\eta} N_{D^0\bar{D}^0} \mathcal{BF}_{\omega \to \pi^+\pi^-\pi^0} \mathcal{BF}_{\eta \to \gamma\gamma} \mathcal{BF}_{\pi^0 \to \gamma\gamma}} \tag{A.2}$$

where $N_{D^0 \to \omega\eta}$ is the observed yield and $N_{D^0\bar{D}^0}$ is the total number of $D^0/\bar{D}^0$ events. We

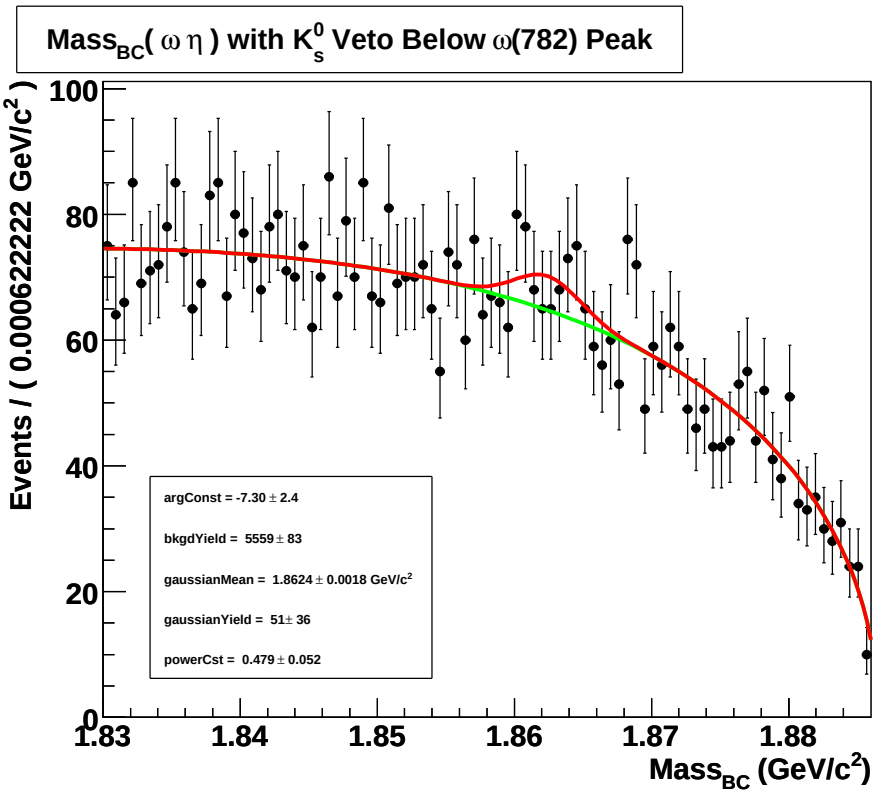

Figure A.8: Data: M_{bc} Fit under 3σ ΔE Cut, $\omega(782)$ $0.74 - 0.765$ GeV/c^2

calculate $N_{D^0\bar{D}^0}$ by multiplying $\sigma(e^+e^- \to D^0\bar{D}^0)$ previously reported by CLEO[36] and our integrated luminosity. Table A.8 contains the Branching Fraction inputs.

Comparing the Yield/Efficiency results in Table A.7 we see the K^0_s Subtraction and Veto are both acceptable methods to deal with the K^0_s signal contamination. Using the Y/ϵ values we compute a difference of 115, which is 3.0% of the average Y/ϵ, 3816. Though the Y/ϵ values are larger in the subtraction method, this method also has a conceptual problem. Our subtraction choice is a best guess; there is no clear way to determine how many K^0_s actually contribute to the signal rather then the background.

Comparing using M_{bc} and ΔE to extract the yield, we have a ± 1 systematic uncertainty from the difference in signal yield and $\pm 0.34\%$ from the difference in Efficiency. These amount to a 2.13% relative uncertainty. We also have ± 41 systematic due to the difference in yield between the fixed and floating yields in M_{bc}. In order to account for possible peaking

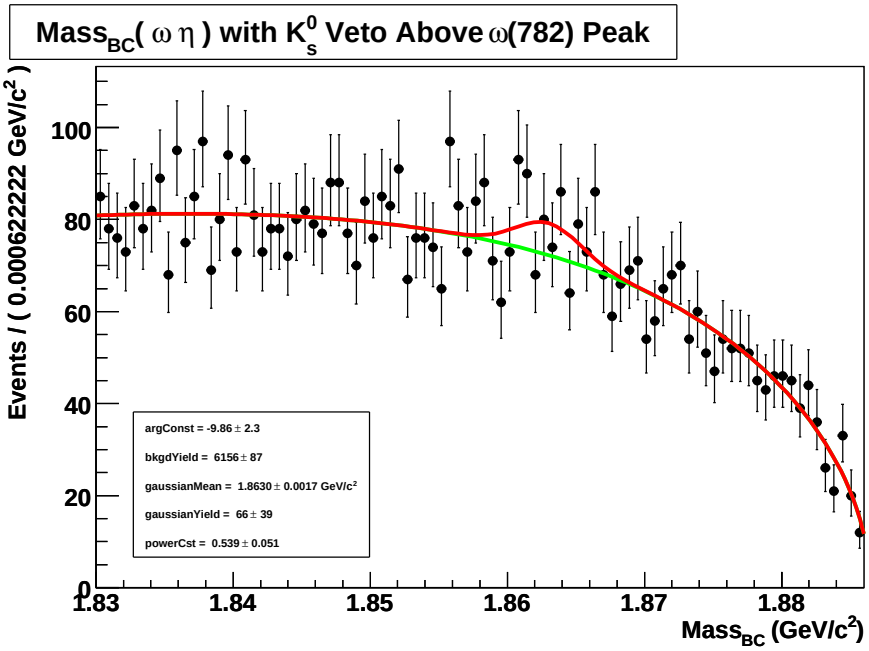

Figure A.9: Data: M_{bc} Fit under 3σ ΔE Cut, $\omega(782)$ $0.8 - 0.82$ GeV/c^2

Table A.5: Signal and Background Yields From M_{bc}, Comparing Three M($\pi^+\pi^-$) Regions

	In Relation to K^0_s Peak		
3σ M_{bc}	Below	In	Above
Signal	347	122	229
Background	1749	327	1649
Sig/Total	16.56%	27.17%	12.19%

backgrounds, we also include ± 72 systematic uncertainty from the difference between the subtraction and veto K^0_s methods. The two yield systematics give us the total systematic on yield. The statistical uncertainty comes exclusively from the statistical uncertainty in the signal yield. All of the uncertainties are summarized in Table A.9. The contribution from $\mathcal{BF}(\pi^0 \to \gamma\gamma)$ is neglible.

Thus we measure the average of $D^0 \to \omega\eta$ and $\bar{D}^0 \to \omega(782)\eta$ as

$$\mathcal{BF}_{D^0 \to \omega\eta} = (1.78 \pm 0.19 \pm 0.35) \times 10^{-3} \tag{A.3}$$

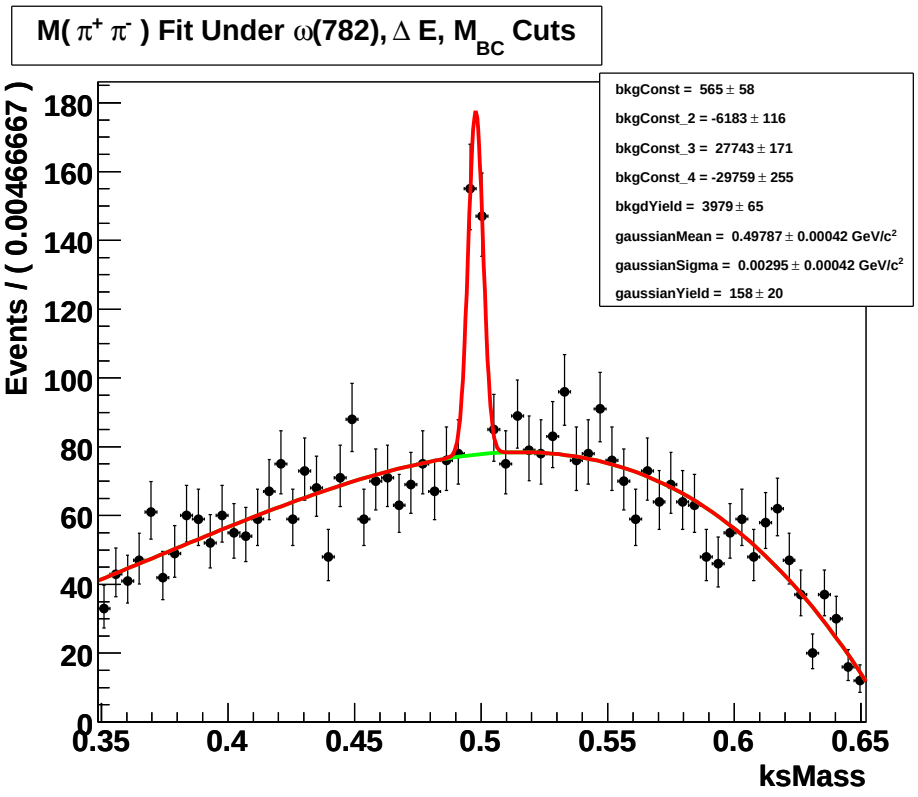

Figure A.10: Data M($\pi^+\pi^-$) Fit.

This agrees well with a result reported by BABAR and is roughly a factor of two smaller than a theoretical prediciton. This decay mode is a CP–eigenstate, making it a valuable tool in heavy flavor analysis.

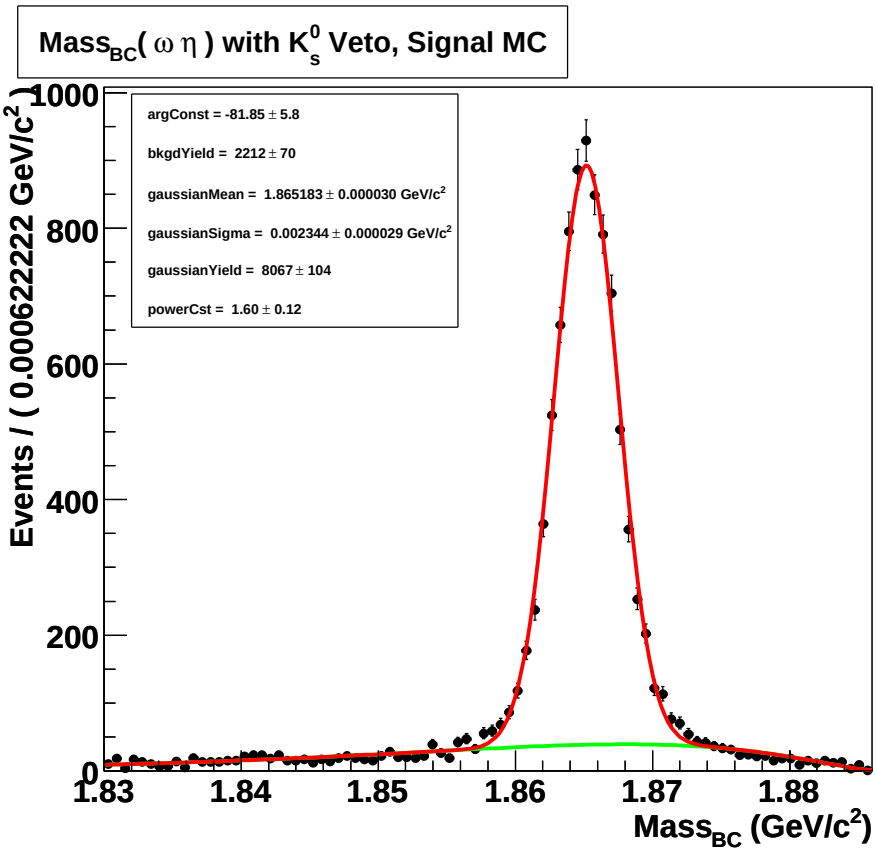

Figure A.11: Beam-Constrained Mass Fit of Signal Monte Carlo $D^0 \to \omega\eta$ with K^0_s Veto.

Table A.6: Summary of Signal Cuts with K^0_s Veto

Signal Cuts
$M(\pi^+\pi^-) \leq 0.48902$ GeV/c^2 or $M(\pi^+\pi^-) \geq 0.50672$ GeV/c^2
0.76010 GeV/c$^2 \leq m(\pi^+\pi^-\pi^0) \leq 0.80474$ GeV/c^2
-0.03551 GeV $\leq \Delta E \leq 0.03145$ GeV
1.857738 GeV/c$^2 \leq M_{bc} \leq 1.871802$ GeV/c^2

Table A.7: Signal Yields from Fittings With K^0_s Effects

	Type	Signal Yield	Signal ϵ	Yield/ϵ
K^0_s Events Subtracted	M_{bc}	667 ± 67	$(17.49 \pm 0.216)\%$	3819
	ΔE	677 ± 72	$(17.06 \pm 0.220)\%$	3969
K^0_s Veto	M_{bc}	596 ± 62	$(16.13 \pm 0.208)\%$	3694
	ΔE	597 ± 67	$(15.79 \pm 0.212)\%$	3780

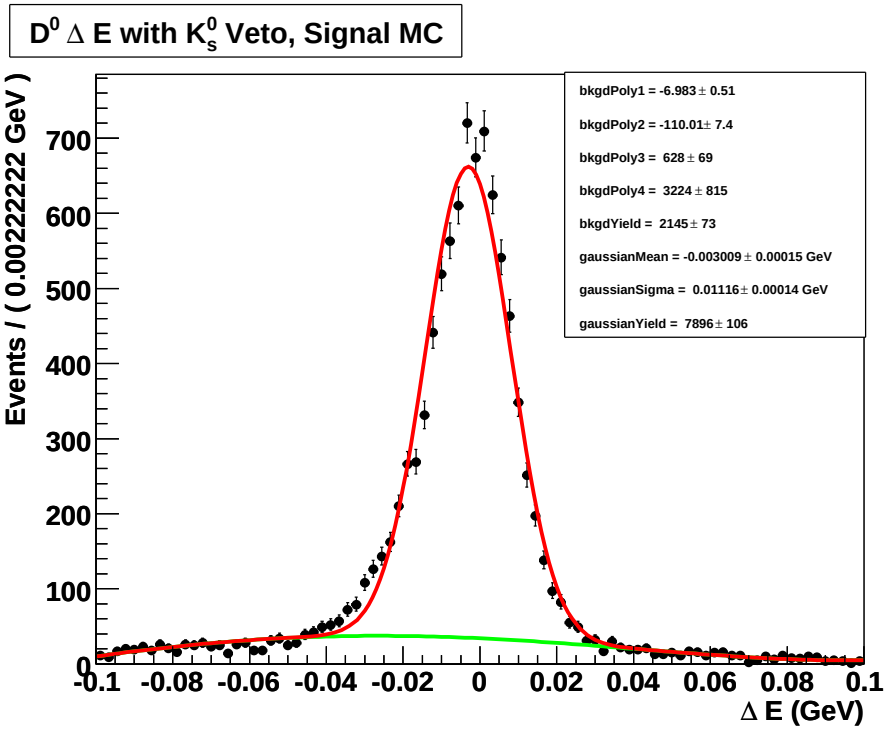

Figure A.12: ΔE Fit of Signal Monte Carlo $D^0 \to \omega\eta$ with K^0_s Veto.

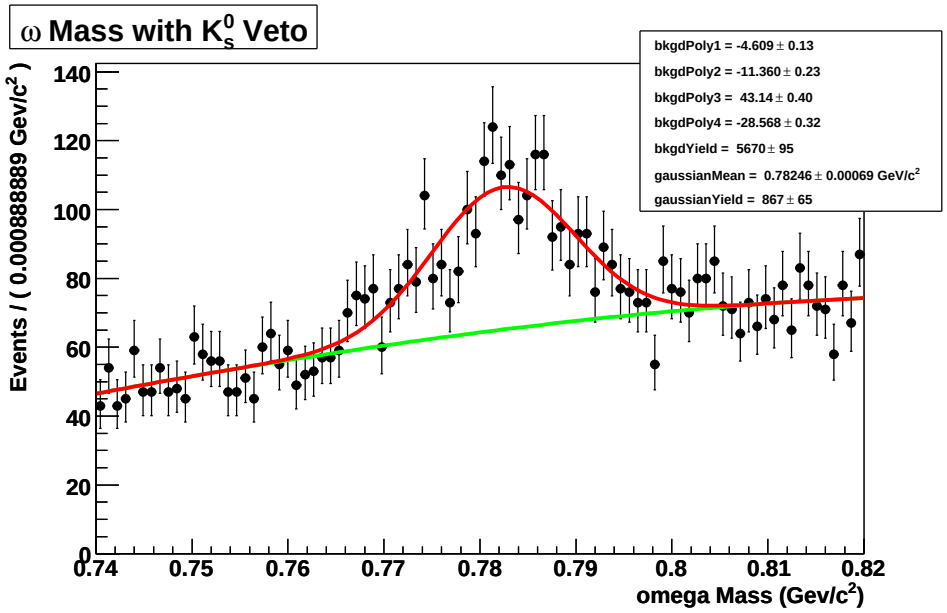

Figure A.13: Data $M(\omega(782) \to \pi^+\pi^-\pi^0)$ Fit with K^0_s Veto

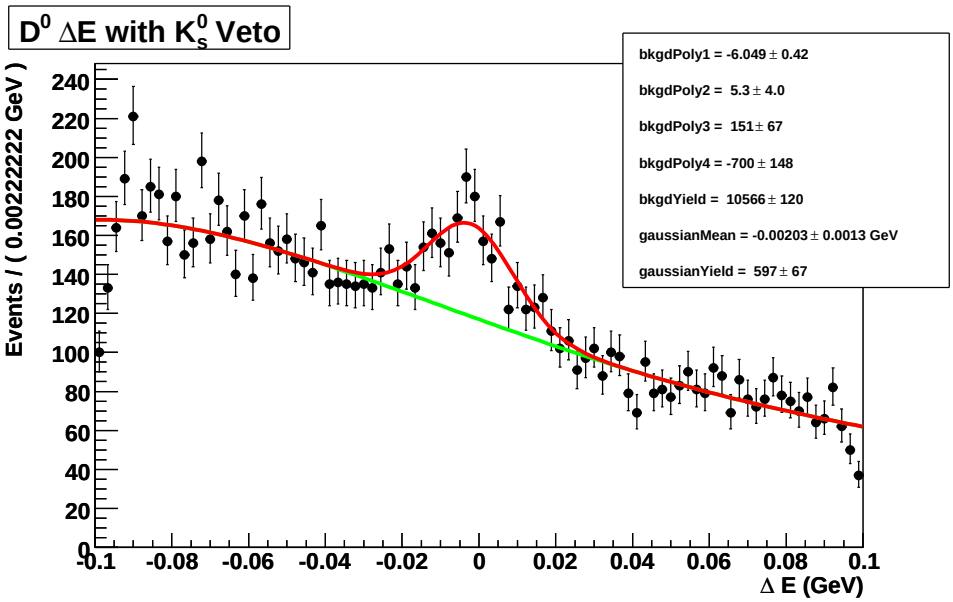

Figure A.14: Data ΔE Fit with K_s^0 Veto

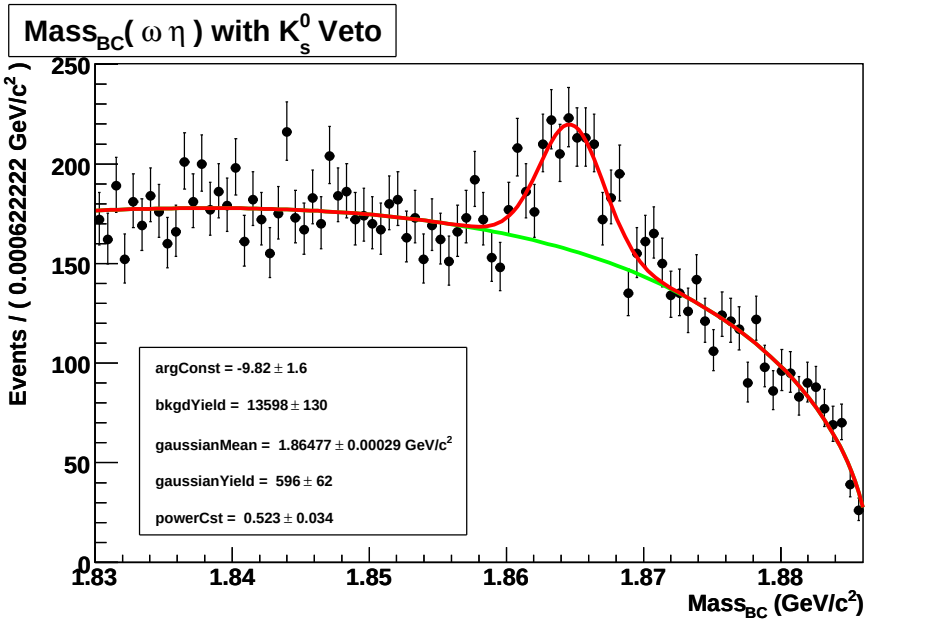

Figure A.15: Data M_{bc} Fit K_s^0 Veto

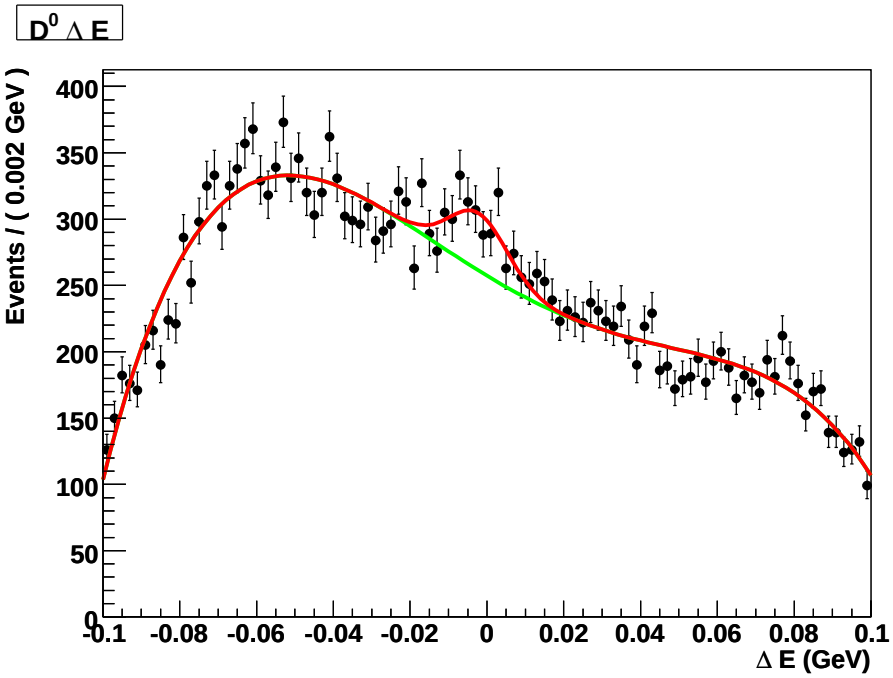

Figure A.16: $D^0 \to \omega\eta$: ΔE Projection of 2D ΔE vs. M_{bc} fit.

Table A.8: Summary of Branching Fraction Inputs. Branching Fractions are PDG[8] values. Uncertainties are statistical and systematic, respectively.

Quantity	Value
Signal Yield	$596 \pm 62 \pm 1$
Efficiency	$(16.13 \pm 0.208 \pm 0.34)\%$
$\mathcal{BF}(\omega(782) \to \pi^+\pi^-\pi^0)$	$(89.2 \pm 0.7)\%$
$\mathcal{BF}(\eta \to \gamma\gamma)$	$(39.31 \pm 0.2)\%$
$\mathcal{BF}(\pi^0 \to \gamma\gamma)$	$(98.823 \pm 0.034)\%$
$\sigma(e^+e^- \to D^0\bar{D}^0)$	$(3.66 \pm 0.03 \pm 0.06)nb$
Luminosity	$818 \pm 8\text{pb}^{-1}$
$N_{D^0\bar{D}^0}$	2993880

Table A.9: Summary of the uncertainties on $\mathcal{BF}_{D^0\to\omega\eta}$.

Source	Value ($\times 10^{-3}$)
Statistical on Yield	± 0.19
Signal Yield	± 0.125
Difference Between K^0_s Methods	± 0.215
MC Efficiency	± 0.038
Luminosity	± 0.0178
Cross Section	± 0.0326
$\mathcal{BF}(\omega(782) \to \pi^+\pi^-\pi^0)$	± 0.0140
$\mathcal{BF}(\eta \to \gamma\gamma)$	± 0.00906
Total Systematic	± 0.345
Total Uncertainty	± 0.39

BIBLIOGRAPHY

[1] F. Halzen and A. D. Martin, *Quarks and Leptons: An Introductory Course in Modern Particle Physics*. John Wiley and Sons, Inc. (1984).

[2] M. Srednicki, *Quantum Field Theory*. Cambridge University Press. (2007).

[3] M. Peskin and D. Schroeder, *An Introduction to Quantum Field Theory*. Addison-Wesley Pub. Co. (1995).

[4] M. K. Sundaresan, *Handbook of Particle Physics*. CRC Press LLC. (2001).

[5] L. Pauling, *General Chemistry*. W.H. Freeman & Co Ltd. (1970).

[6] Retrieved from `http://upload.wikimedia.org/wikipedia/commons/3/3a/Meson_Octet.png`, July 1, 2008. Redistributable under the GNU Free Documentation License. Author: Wikipedia user Laurascudder.

[7] Tevatron Electroweak Working Group, arXiv:0803.1683v1 [hep-ph].

[8] J. Beringer *et al.* (Particle Data Group), Phys. Rev. **D86**, 010001 (2012) and 2013 partial update for the 2014 edition.

[9] Retrieved from `http://upload.wikimedia.org/wikipedia/commons/8/89/Beta_Negative_Decay.s` July 1, 2008. Public Domain.

[10] K. Berkelman, *A Personal History of CESR and CLEO: The Cornell Electron Storage Ring and Its Main Particle Detector Facility*, World Scientific (2004).

[11] D. M. Asner *et al.* (CLEO Collaboration), Phys. Rev. D **78**, 012001 (2008).

[12] S. Kopp *et al.* (CLEO Collaboration), Phys. Rev. D **63**, 092001 (2001).

[13] R. H. Dalitz, *Phil. Mag.* **44**, 1068 (1953).

[14] P. Rubin *et al.* (CLEO Collaboration), Phys. Rev. Lett. **93**, 111801 (2004).

[15] B. Aubert *et al.* (BaBar Collaboration), Phys. Rev. D **72**, 052008 (2005).

[16] J. M. Link *et al.* (FOCUS Collaboration), Phys. Lett. B **610**, 225 (2005).

[17] CLEO-c and CESR-c Yellow book, CLNS 01/1742, Laboratory for Elementary-Particle Physics Publication (2001) .

[18] G. Bonvicini *et al.* (CLEO Collaboration), Phys. Rev. D **89**, 072002.

[19] Retrieved from `http://www.lns.cornell.edu/Research/EPP/CLEO/ WebHome.html`, July 1, 2008.

[20] Retrieved from `http://www.interactions.org/imagebank/images/COO028M.jpg`, March 19, 2014.

[21] Retrieved from `http://www.lns.cornell.edu/public/lab-info/dr.gif`, July 1, 2008.

[22] Heltsley, B. K., Annals of the New York Academy of Sciences **535** 558 (1988).

[23] Retrieved from `http://www.lns.cornell.edu/public/lab-info/mu.html`, August 21, 2014.

[24] Retrieved from `https://wiki.lepp.cornell.edu/lepp/bin/view/CLEO/Private/AC/FrequentFigures`, July 1, 2008.

[25] R. A. Briere and G-P. Chen, CBX 07-30, CLEO Internal Document (2007).

[26] P. Onyisi and W. Sun, CBX 06-11, CLEO Internal Document (2006).

[27] C. S. Park and E. H. Thorndike, CBX 05-73, CLEO Internal Document (2005).

[28] C. S. Park, `http://www.lns.cornell.edu/restricted/CLEO/CLEO3/soft/hints/EID.html`, CLEO Internal Webpage.

[29] B. Heltsley, CBX 06-28, CLEO Internal Document (2006).

[30] `https://wiki.classe.cornell.edu/CLEO/Private/SW/CLEOcMC`, CLEO Internal Webpage.

[31] D. Andrews *et al.* (CLEO Collaboration), Phys. Rev. Lett. **44** 1108 (1980).

[32] D. Andrews *et al.* (CLEO Collaboration), Phys. Rev. Lett. **45** 219 (1980).

[33] D. M. Asner *et al.* (CLEO Collaboration), Phys. Rev. Lett. **92** 142001 (2004).

[34] T. E. Coan *et al.* (CLEO Collaboration), Phys. Rev. Lett. **96** 162003 (2006).

[35] J. P. Alexander *et al.* (CLEO Collaboration), Phys. Rev. Lett. **77** 5000 (1996).

[36] S. Dobbs *et al.* (CLEO Collaboration), Phys. Rev. D **76** 112001 (2007).

[37] G. Bonvicini *et al.* (CLEO Collaboration), Phys. Rev. D **89** 072002 (2014).

[38] S. U. Chung *et al.*, Annalen der Physik **507.5** 404-430 (1995).

[39] E687 Collaboration, P. Frabetti *et al.*, Phys. Lett. **B 331**, 217 (1994).

[40] M. Dubrovin and D. Cinabro, CBX 06-18, CLEO Internal Document (2006).

[41] B. Bhattacharya and J. L. Rosner, Phys. Rev. D, **82** 037502 (2010).

ABSTRACT

MULTIPLE DALITZ PLOT ANALYSIS AT CLEO-c

by

MACKENZIE J. SMITH

December 2015

Advisor: Dr. David Cinabro

Major: Physics

Degree: Doctor of Philosophy

Dalitz Plot analysis is a standard technique for the study of weak hadronic 3-body decays. This technique allows us to extract the relative amplitudes, phases, and fit fractions of the resonances that are the primary product of such decays. A Dalitz analysis is complicated by the presence of two or more interfering resonances that appear at the same place on the plot. In this analysis I attempt to resolve the $K^0_s a_0(980)^0$ and $K^0_s f_0(980)$ in the decay of $D^0 \to K^0_s K^+ K^-$. Using the $K^0_s a_0(980)^0$ resonance found in $D^0 \to K^0_s \pi^0 \eta$, I compare equating a resonance in an interfering decay channel with a non–interfering channel by fit fraction or amplitude. I use the 818 pb^{-1} of CLEO-c data collected a $\psi(3770)$ energies to perform the Dalitz plot analysis of $D^0 \to K^0_s \pi^0 \eta$ and $D^0 \to K^0_s K^+ K^-$. I find large fractions from both $K^0_s a_0(980)^0$ and $K^0_s f_0(980)$ that destructively interfere to leave the $K^0_s \phi(1020)$ as the dominant resonance on the plot.

AUTOBIOGRAPHICAL STATEMENT

Name: Mackenzie J. Smith

Education:
B.S. Physics, University of Michigan–Dearborn, Dearborn, Michigan, 2005
A.S. General Science, Wayne County Community College District, Detroit, Michigan, 2000
Professional Experience:
Graduate Research Assistant, Dept. of Physics and Astronomy, WSU, 2007-2015
Graduate Teaching Assistant, Dept. of Physics and Astronomy, WSU, 2006-2007
Publications: "Multiple Daltiz Plot Analysis," (to be published).
"Initial Observation of $D^0 \to \omega\eta$," Physics Review D Rapid (to be published).

My interest in science began with healthy portions of science fiction, in particular Star Trek. I focused physics in my college years following my enjoyment of the subject in high school.

During my undergraduate studies at the University of Michigan-Dearborn, I had the opportunity to spend two summers performing thin film research here at Wayne State under the tutelage of Drs. Vaman and Ratna Naik. Here I experienced the workings of a real experiment, presented our work at Argonne National Lab and the State Capital, and got a glimpse of several potential research paths.

With the assistance of A. Nadasen and the Naiks, I returned to Wayne State to pursue my doctorate under the advisement of D. Cinabro. Starting with a study of $\gamma \to e^+e^-$ production rates in the CLEO-c detector, I went on to work on the Dalitz plot analysis of $D_s \to KK\pi$ and finally the Multiple Dalitz Plot Analysis that is the subject of this thesis.

Besides physics, I am an admirer of the arts, an occasional photographer, news junky and armchair diplomat, competent cook, and petty dabbler in strength training.